X-ray studies on adsorption processes at solid-liquid interfaces and ultrafast dynamics in water

vorgelegt von

Yury Forov

Lehrstuhl für Experimentelle Physik Ia
Fakultät Physik
Technische Universität Dortmund
2018

Table of Contents

Chapter 1

Introduction

The investigation of water and aqueous solutions has been a fascinating topic of research for scientists and philosophers through the entire existence of humans on earth [1]. Many biological and chemical processes that are of great importance for human life take place within a liquid environment [2, 3]. Usually, in this processes materials with different structural properties come in contact, where interfaces between this materials are formed. The understanding of the behavior of water and chemical processes at interfaces have always been of great importance for human life [4, 5].

However, it took up to the late 18th century to discover the composition of water, consisting of two hydrogen atoms and one oxygen atom [6]. With the knowledge of the composition of water, further research on its properties and structure started [7, 8]. Especially in the case of liquid water, several anomalous properties were detected such as the density maximum in liquid water at 4°C [9], the increase of the isobaric heat capacity or the increase in isothermal compressibility with decreasing temperatures [10, 11]. These and further thermodynamic, dynamic and structural anomalous properties of water are directly linked to its microscopic structure, which is still widely discussed [12, 13, 14, 15, 16]. The highly complex and anomalous character of water is a consequence of the existence of hydrogen bonds that connect two water molecules to each other [17, 18, 19]. This type of bonding makes the water structure very flexible. Each water molecule is able to form four hydrogen bonds, which may optimally arrange themselves tetrahedrally around a water molecule. However, with a perfectly tetrahedrally ordered structured water neither all the anomalies of water may be described [20, 21, 22] nor is this structure supported by experimental data [23, 15, 24, 25]. In current literature, several different structures of liquid water are proposed and discussed controversially [26, 27, 28, 29, 30]. One of the most popular theories describes water as a mixture of two different states, high density water and low density water. In low density water, water is tetrahedrally ordered, while in high density water the hydrogen network is distorted, resulting in a denser packing of water molecules [31, 32, 26]. This theory describes many anomalies of water very well even though an experimental confirmation is very difficult and still pending [31, 17, 12].

With a better understanding of the structure of water, also solvation science became

an important research field during last decades [33, 34, 35]. Due to the high flexibility of hydrogen bonds, water is a good solvent for hydrophilic solutes [36, 3]. Since the majority of chemical reactions and biological processes take place within a liquid environment, the understanding of solvation processes is of great interest [2, 3]. Especially in the recent years, the traditional point of view of seeing solvents as inert media for different molecular processes changed into recognizing solvents to have an active role in such processes [36, 37]. However, understanding thoroughly such processes is difficult since it requires a great knowledge of the influence of all components and the thermodynamic properties of the system [38, 39].

In the presence of a solid, changes in the structure of water next to the solid-liquid interface are induced [40, 36, 41, 42]. This type of water is therefore called interfacial water. Additionally, also differences in the properties of the solid lead to differences in the structure of interfacial water. One of the main aspects here is the distinction between a hydrophilic and a hydrophobic surface. In the case of a hydrophilic surface, water can perform an electrostatic interaction with the surface of the solid, which may lead to a long range order in the interfacial water induced by the solid [43, 44, 45, 46]. In opposite, water is not able to perform an electrostatic interaction with a hydrophobic (nonpolar) surface and thus only Van der Waals interactions between water and the hydrophobic surface are possible [36, 40, 45]. Therefore, an area of low electron density forms between hydrophobic surfaces and water ranging over a few angstrom [47, 48, 49, 50].

The presence of a solid also affects the solutes in aqueous solutions. Aqueous solutions containing proteins have often been subject of research to study their structure as well as their interaction with other molecules due to their key role in biological and technical processes [51, 52, 53, 54, 55]. In the presences of a solid-liquid interface, proteins in aqueous solutions tend to adsorb on this interface [56, 57, 58]. Proteins at such interfaces have a broad application field ranging from food industry over drug delivery, application in biosensors or formation of biofilms on implants [59, 60, 61, 62, 63, 64]. Especially in the last case, an uncontrollable formation of biofilms on implants is undesired since it supports growth of bacteria, so that the risk of an inflammatory reaction rises [65]. In opposite, the lubricating properties of a biofilm can be used by a controlled formation of biofilms on implants to support the ingrown of the implant [66]. One of the main materials used for implants is titanium oxide [67]. Therefore, the investigation of the adsorption behavior of proteins on titanium oxide is highly interesting. Nevertheless, the specific mechanism of protein adsorption is not completely understood yet [68]. One of the main problems is the fact that the adsorption behavior is driven by many parameters, such as the structure of the surface [69], concentration of the proteins [70], ionic strength [71], cosolvents [72], electrostatic interactions [73] and thermodynamic properties of the system like temperature [74, 75], pressure [76] or pH value [77]. Furthermore, since the solvent also plays an important role in the adsorption behavior of proteins, it is necessary to investigate the adsorption behavior *in-situ* with atomic resolution [78, 69]. There are several studies on the adsorption behavior on proteins at solid-liquid interfaces using different experimental methods, e.g. ellipsometry [79], surface plasmon resonance spectroscopy [80], atomic force microscopy [81] or neutron

and X-ray scattering methods [82, 83]. The method of choice for this thesis is X-ray reflectivity (XRR), since it fulfills all necessary requirements to study the protein adsorption mechanism under varying thermodynamic conditions. Up to now, XRR was used to investigate the adsorption behavior of proteins on silicon substrates, since only these substrates are flat enough without curvature and have a surface roughness of only a few angstrom, which is necessary to perform XRR experiments [69, 84, 74]. Nevertheless, new preparation methods allow to deposit other substances on the silicon substrate that still fulfill these conditions [85, 86]. Therefore, a silicon wafer with a titanium oxide layer was chosen as substrate material to be investigated in this thesis, since titanium oxide surfaces are widely used in technical and medical applications [87, 88, 89, 90]. Since no studies on the adsorption behavior of proteins on with titanium oxide covered silicon substrates are known yet, the protein of choice is lysozyme. The adsorption behavior of lysozyme on silicon oxide as a function of temperature was recently studied [74]. Therefore, a part of this thesis deals with the adsorption behavior of lysozyme on titanium oxide as a function of temperature as well as other thermodynamic properties like pH value and pressure. Furthermore, the thickness of the titanium oxide layer was varied to investigate its influence on the adsorption behavior. The results of this study were already published in the journal Langmuir [91].

Another solid-liquid interface that plays an important role in several technical applications is the interface between a hydrophobic surface and aqueous solutions [92, 93, 94]. Here, especially the presence of ions at such interfaces is of great interest, since such systems play a crucial role in several processes in industry [95, 96, 97]. Much pioneer work has been done to describe the interactions between ions and hydrophobic surfaces, but a complete description of the physical mechanism for the hydrophobic interaction is still pending [98]. From MD simulations, different parameters like polarizability, size and charge have been identified, effecting the accumulation of ions at interfaces [99, 100, 101, 102]. In general, these parameters codetermine the hydration enthalpy of ions and their ability to break or to stabilize the water network [36]. Thus, a variation of hydration enthalpy has an impact on the hydrophobic interaction between ions and interfaces.

In the past, the ion distribution at liquid-gas interfaces was in the focus of interest, using several experimental techniques, yielding different conclusions. For example, Ghosal et al. [103] report on the accumulation of halides at the liquid-gas interface while an XRR study of Sloutskin et al. [104] did not confirm the proposed strong ion accumulation. However, liquid-gas interfaces are modulated by capillary waves, which are not considered in MD simulations and cause a convolution of the simulated density profiles. The proposed ion density excess at the liquid-gas interface might be significantly reduced by this effect. The use of hydrophobic solid-liquid interfaces avoids this problem. Especially the use of octadecyltrichlorosilane (OTS) coated surfaces seems to be very promising because of the existence of the so-called hydrophobic gap [48] (low electron density area between OTS and the liquid phase), which shows a strong signature in the reflectivity signal. This signature is very sensitive on the adsorption of material at the interface and can be used to analyze the formation of extreme thin layers [49]. OTS is a self-assembled monolayer, consisting of a polar silanol head group that adsorbs on

silicon oxide surfaces and a nonpolar alkyl chain group pointing towards the liquid. Hydrophobic solid liquid-interfaces between OTS coated wafers and aqueous solutions were intensively studied recently [48, 49, 105, 106]. High pressure effects on the structure of the hydrophobic gap or protein adsorption at such interfaces were investigated as well as the effect of the change of the solvent from water to nonpolar solvents by means of XRR, demonstrating the great capability of this technique [78]. Therefore, a part of this thesis will deal with ion adsorption on OTS varying concentration and ion size.

After the investigation of adsorption processes at solid-liquid interfaces, a second field of study in this thesis is the solvent itself, liquid water. One of many approaches to reveal new insight on the properties of liquid water is the investigation of the behavior of water on very short time scales (femtoseconds and shorter) [107, 108, 109, 110]. Usually, pump-probe experiments are used to investigate such short time scales, where a first laser or X-ray pulse initiates a process while a second pulse probes the system after a desired time delay [111, 112, 113]. However, several difficulties limit the use of ultrashort pulses to study the structure of water, such as a high repetition rate of the laser or the necessity of changing the sample on very short time scales since the pump and probe pulses produce damages in the sample. An alternative approach to study the structure of water on even shorter time scales (attoseconds) was presented by Abbamonte et al. in the year 2004 [114]. Here, Inelastic X-ray Scattering (IXS) is used as experimental technique to investigate the evolution of an electronic density disturbance in water on attosecond time scales with atomic resolution. X-ray based methods, such as IXS, are widely used to determine information about the local atomic and electronic structure of matter [115, 27, 116]. For example, IXS provides information about the electron density of states, since the measured intensity in IXS experiments is proportional to the dynamic structure factor [117, 27]. Moreover, the dynamic structure factor is linked to the electron density propagator [118]. Thus, changes in the electron density of the investigated system may be derived as described by Abbamonte et al. [118]. However, the resolution of the propagator in space and time is limited by the maximal investigated momentum and energy transfer ranges. Measuring IXS spectra over large momentum and energy transfer ranges with a reasonable step size in momentum and energy transfer is desirable but difficult. Due to the small cross-section of an inelastic scattering event, such experiments have to be carried out at third generation synchrotron radiation facilities [117]. In the year 2004, Abbamonte et al. were able to investigate IXS spectra of water at ambient conditions within a momentum transfer range between $0.476\,\text{\AA}^{-1}$ and $4.95\,\text{\AA}^{-1}$ and an energy transfer range between $0\,\text{eV}$ and $100\,\text{eV}$, resulting in a spatial resolution of $1.27\,\text{\AA}$ and a time resolution of $41.3\,\text{as}$ in order to study the evolution of the electron density disturbance [114]. Due to technological progress, currently the investigation of significantly larger momentum and energy transfer regions is possible. In the framework of this thesis, electron density disturbances in water were studied with a significantly higher resolution. Moreover, limitations as well as requirements for such experiments are discussed. Besides measurements of water at ambient conditions, the temperature was also varied to $4\,^\circ\text{C}$ and $90\,^\circ\text{C}$ to investigate differences in the evolution of the electron density disturbance for different

densities of water.

This thesis is therefore structured as follows: in chapter 2 the used sample systems are introduced with special focus on the structure of liquid water and the solution of ions and proteins in water. Furthermore hydrophilic and hydrophobic solid-liquid interfaces will be discussed and a brief overview on adsorption processes in general is given. Chapter 3 presents results of the study of adsorption processes at solid-liquid interfaces. After an introduction in XRR theory and the presentation of experimental setups for performing XRR experiments at solid-liquid interfaces, results on the adsorption behavior of lysozyme on titanium oxide as a function of temperature, pH value, TiO_x layer thickness as well as pressure will be shown. Thereafter, the results of the study on the adsorption behavior of ions on OTS will be presented. The local microscopic structure of water is the object of chapter 4. In this chapter, a short overview on the theory of IXS is provided together with a detailed description on how to derive the electron density propagator, which will be thereafter investigated on ultrashort time and space scales in liquid water at 4 °C, 20 °C and 90 °C. Finally, all results are summarized in chapter 5 and an outlook on possible follow-up projects is given.

Chapter 2

Samples

In the framework of this thesis, the local structure of water as well as adsorption processes at interfaces between solids and aqueous solutions are investigated. Even though water is a frequently studied system and became one of the main fields of research over the last decades [119, 120, 121, 122, 36, 123], many open questions concerning the properties of water, caused by its structure, exist [18, 12, 124]. Moreover, the structure of water at interfaces differs from the structure of bulk water, which becomes even more intricate by replacing water by an aqueous solution [125, 126, 40, 127, 36]. Section 2.1 gives an overview on the structure of water and aqueous solutions. As solutes, several ions as well as the protein Lysozyme were chosen [128, 129, 130, 131, 132]. A detailed description on these materials is presented in sections 2.1.2 and 2.1.1.

When an aqueous solution is in contact with solids, a solid-liquid interface develops (see for further details [133, 134]). In this case, molecules, which are solved in water, tend to adsorb at the solid-liquid interface [135, 56]. However, many factors affect the adsorption process such as Van der Waals forces [136, 69], electrostatic interactions [73], addition of cosolvents [71, 137] or hydrophobic and entropic effects [138, 72]. This will be explained in detail in section 2.2, in which also titanium oxide and octadecyltrichlorosilane (OTS) as surface material of the solids will be introduced.

2.1 Water and Aqueous Solutions

A more complete overview of scientific efforts regarding the structure of water and aqueous solutions is given in literature [139]. Therefore, this section only summarizes the necessary information.

Water is a small molecule consisting of two hydrogen atoms and one oxygen atom, resulting in the molecular formula H_2O. In liquid water, a single water molecule is V-shaped with a mean O-H length of 0.97 Å and the mean H-O-H angle of 106°. However, these values differ for each individual molecule, being dependent on its energy and surroundings. Each molecule is electrically neutral but polar, with the positive charge distributed around the hydrogen atoms and the negative charge on the opposite side around the oxygen atom. Due to the polarity of the molecules, two molecules can

attract each other. This attraction is the strongest in the case of an O-H bond of one molecule pointing directly towards the oxygen atom of another molecule, which is called hydrogen bonding. Two bonded molecules of water form a water dimer. Here, the distance between the oxygen atoms is slightly below 3 Å, depending on the temperature of the water.

By increasing the number of water molecules, further hydrogen bonds are formed, resulting in a more complex structure of the water. There are several theories about the structure of water. One of the most popular theories describes water as a mixture of high density water (HDW) and low density water (LDW). In LDW, each water molecule has four approximately tetrahedrally arranged electron pairs. Two of these electron pairs are associated with covalent bonds to the hydrogen atoms, while the two other electron pairs are remaining as lone pairs. In the case of HDW, the hydrogen network is distorted, leading to a more packed structure.

It is widely accepted that the structure of liquid water, which is dynamic and can be modified by thermodynamic properties like temperature and pressure, is connected with the anomalies of water. For example, due to the tetrahedral hydrogen-bonded geometry, the density of the solid state of water is lower than the density of liquid water. In the solid state, the molecules form an essentially perfect tetrahedrally coordinated network with much empty space between the molecules. This network is distorted upon melting, leading to a more fluxional and denser packed network. At ambient pressure, a maximal density of $1\,g/cm^3$ at a temperature of 4°C can be reached, which decreases both with rising and decreasing temperatures.

2.1.1 Ions

The flexibility of the structure as well as the polarity of the molecules of water make it a good solvent. During the interaction with ions, water molecules can solve cations by orienting their oxygen atoms toward the ion and adopt the opposite configuration during interaction with anions. Even though these interactions affect the local water structure, no geometric distortion of water structure over long ranges occur [36]. However, due to the fact that ions differ significantly in size (see for example table 2.1 for the ions used in this thesis), the local structure of the solution varies for each ion. Therefore, solutes may be classified in terms of their ability to enhance or degrade the short-range order in the liquid. Large ions with a small charge per size ratio support the breaking of hydrogen bonds in water, leading to a denser solution, which is more liquid-like. These ions are called chaotropes. On the other hand, small ions, having a high charge per size ratio, increase the local order in water and contribute to a more ice-like structure of the solution. These ions are called antichaotropes or kosmotropes [36].

The ability to impose order on the hydrogen-bonding network or to break hydrogen bonds becomes especially relevant for a coexistence of ions and proteins in an aqueous solution. In this case, interactions between ions and proteins as well as ions and the water molecules directly contacting the proteins (first hydration shell) occur, resulting in a strengthened or weakened hydrophobic interaction. Here, chaotropes are able to weaken the hydrophobic interaction, leading to a better solubility of the protein, which

Table 2.1: Properties of ions used in this thesis.

Ion	Atomic radius [Å][140]	Covalent radius [Å][141]	Van der Waals radius [Å][142, 143]	Ionic radius [Å][144]
H^+	0.25	0.31 ± 0.05	1.10	0.10
Li^+	1.45	1.28 ± 0.07	1.82	0.76
Na^+	1.80	1.66 ± 0.09	2.27	1.02
K^+	2.20	2.03 ± 0.12	2.75	1.38
Rb^+	2.35	2.20 ± 0.09	3.03	1.52
Cs^+	2.60	2.44 ± 0.11	3.43	1.67
Cl^-	1.00	1.02 ± 0.04	1.75	1.81
Br^-	1.15	1.20 ± 0.03	1.85	1.96
I^-	1.40	1.39 ± 0.03	1.98	2.20

is called salting-in. On the other hand, kosmotropes are able to strengthen the hydrophobic interaction and thus to decrease the solubility of the protein in solution, which is called salting-out. Ions can also directly interact with proteins. Ions with a strong salting-in effect are strong denaturants. A classification of ions in order of their ability to salt-in or salt-out proteins is given by the Hofmeister series [145, 146]. However, the mechanism of the Hofmeister series is not entirely clear yet [147]. The classification of the ions used in this thesis is as follows: [148]

kosmotropes   **chaotropes**

$$Cl^- \quad > \quad Br^- \quad > \quad I^-$$

$$Cs^+ > Rb^+ > K^+ > Na^+ > Li^+.$$

2.1.2 Proteins

Proteins are large molecules consisting of long chains of amino acid residues. Due to their functions in biological processes in organisms, proteins play a crucial role in human life [149, 38]. Each function of a protein originates from its three dimensional structure. There are four distinct characteristics in the structure of a protein [150, 151]:

Primary structure The primary structure is an amino acid sequence, also called polypeptide chain, starting from an amino-terminal and ending with a carboxyl-terminal.

Secondary structure: The secondary structure is the pattern of hydrogen bonds between backbone amine and carboxyl groups. The most common pattern are

α-helices (right hand-spiral conformation), β-sheets (two or three backbone hydrogen bonds are forming a generally twisted, pleated sheet) and turns (the polypeptide chain reverses its overall direction). In a protein, many regions of different secondary structures may occur.

Tertiary structure: The tertiary structure is the three-dimensional structure of a protein and describes the spatial relationship between the secondary structures. In a functional protein, the tertiary structure is usually complex due to non-local interactions that force the protein to fold and stabilize it. By unfolding, the protein loses its tertiary structure and thus the functionality.

Quaternary structure: The quaternary structure depicts the arrangement of several protein molecules, which form a protein complex.

The solution of large molecules like proteins in water differs from small molecules (as presented in section 2.1.1) [36]. Since proteins consist of polar and non-polar regions, an integration of the protein into the water structure is not favorable. Instead, water is able to form bonds with the hydrophilic sites, while it does not form bonds with the hydrophobic sites. Therefore, between two hydrophobic molecules in water or a hydrophobic molecule in water and a hydrophobic surface bordering on the aqueous solution, an attractive interaction occurs, which is called the hydrophobic effect [92]. This effect causes the hydrophobic areas of the protein to be folded inside, while the outer, hydrophilic, parts of the protein interact with water, which develops hydration shells around the protein. The hydrophobic effect also promotes aggregation of particles or the adsorption of particles at interfaces, due to the forced minimization of open H-bonds [36]. A detailed description of the adsorption process at interfaces is given in section 2.2.3.

To investigate the adsorption behavior of proteins at interfaces, lysozyme, which is an antimicrobial enzyme, was the protein of choice.

Lysozyme consists of 129 amino acids with a mass of 14.307 kDa that are folded in an almost ellipsoid shape with dimensions of $30 \times 30 \times 45$ Å^3 [152]. The tertiary structure of lysozyme is shown in figure 2.1. Lysozyme is thermally stable up to a denaturation temperature of 71 °C. At ambient conditions, the isoelectric point (IEP) is at pH 11 [153], which means that lysozyme is positively charged at pH 7.
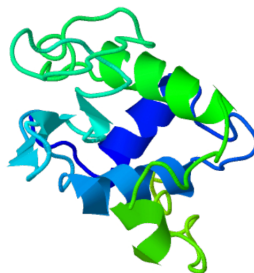

Figure 2.1: Tertiary structure of lysozyme. [154]

Since lysozyme is a functional protein, its interaction with other molecules and interfaces is of great relevance. The next section gives a description on the interaction of lysozyme at solid-liquid interfaces.

2.2 Interfaces

An interface arises between two materials with different structural properties. In the case of the contact of a liquid with a solid material, a solid-liquid interface is formed at the transition region between the solid and the liquid. Next to the solid-liquid interface, the liquid phase changes its structure due to surface forces applied by the solid surface [40, 36, 41, 42]. Therefore, the liquid reorients, leading to changes in the electron density, viscosity, polarity and refractive index of the liquid next to the solid surface (see figure 2.2). In the case of water, this type of liquid is called interfacial water. The properties of the interfacial water strongly depend on the surface with which it comes in contact [43, 44, 45, 46]. Here, a major differentiation is given by the polarity of the surface, which will be discussed in the following subsections.
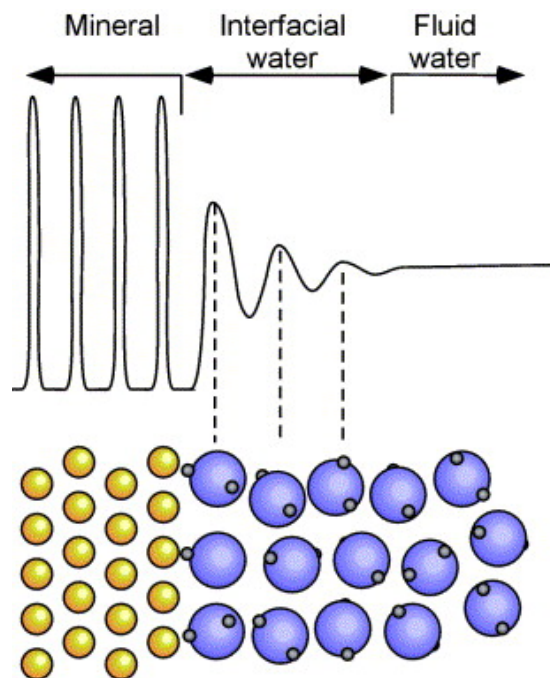

Figure 2.2: Scheme of the electron density (top) and molecular structure (bottom) of a liquid at the solid-liquid interface. [40]

2.2.1 Hydrophilic Surfaces

Hydrophilic surfaces are able to form H-bonds with water and thus induce a long range order in interfacial water. The interfacial energy between the surface and water can be determined by a measurement of the contact angle Θ_C between a water drop and the surface [155]. A scheme of a liquid drop on a surface and the corresponding interfacial energies is shown in figure 2.3. The contact angle and the interfacial energies

11

are connected via the Young equation [156]

$$\gamma_{LV}\cos(\Theta_C) = \gamma_{SV} - \gamma_{SL}, \tag{2.1}$$

where γ_{LV} is the liquid-vapor interfacial energy, while γ_{SV} describes the solid-vapor interfacial energy and γ_{SL} the solid-liquid interfacial energy. Surfaces in contact with water, which have a contact angle below 90° are called hydrophilic, while surfaces with a contact angle above 90° are called hydrophobic [157].
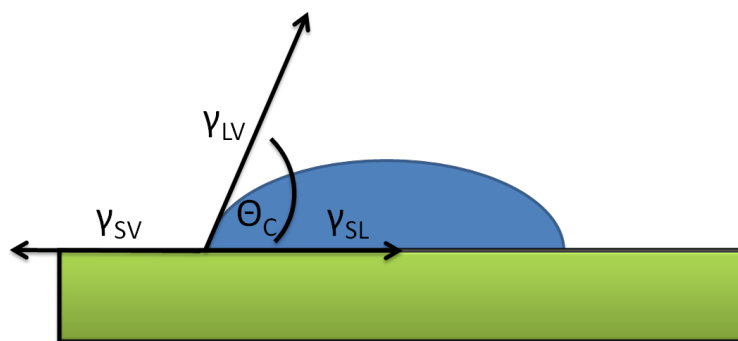

Figure 2.3: Scheme of a liquid drop on a surface and the corresponding interfacial energies, based on [156].

Titanium oxide with amorphous structure [85, 86] was the material of choice as a hydrophilic solid. The contact angle of titanium oxide is in the region between 50°-70° [158]. Titanium oxides are widely used in industry and medicine and thus the investigation of adsorption processes of particles on titanium oxide is of large interest [87, 88, 89, 90]. Especially in the case of dental medicine, titanium with a TiO_2 layer on top is used as a preferred implant material [67]. Studying the adsorption of proteins on titanium oxide is in so far important as adsorbed proteins can initiate the formation of biofilms, which usually results in unwanted consequences [63]. A biofilm on an implant surface may support growth of bacteria, so that the risk of an inflammatory reaction rises [65].

2.2.2 Hydrophobic Surface

On hydrophobic surfaces, water is not able to form H-bonds with the surface. Much effort has been put in to investigate the interface between the hydrophobic surface of octadecyltrichlorosilane (OTS) and aqueous solutions [48, 49, 105, 106, 78]. OTS forms a self-assembled monolayer on silicon oxide substrates due to its amphiphilic structure (see figure 2.4): the head group of OTS, consisting of an silicon atom and three chlorine atoms, is polar, which makes it possible to adsorb on the silicon oxide surface under release of the chlorine atoms, while its long-chain alkyl tail group $((CH_2)_{17}CH_3)$ is non polar providing the hydrophobic surface. At the interface between the OTS tail

group and water, a low electron density area arises, the so-called hydrophobic gap. The existence of the hydrophobic gap is shown in various experiments. However, there is no consensus about the shape of the hydrophobic gap [48, 49]. Nevertheless, recent studies limit the size of the hydrophobic gap to 1 Å - 6 Å [49, 106]. Further investigation on the adsorption process of molecules on OTS regarding changes in the hydrophobic gap will provide a better understanding of both the adsorption process at hydrophobic interfaces as well as the role of the hydrophobic gap and its behavior in presence of additional molecules. Therefore, the adsorption process of ions was investigated in this thesis as a function of ion concentration and ion size.
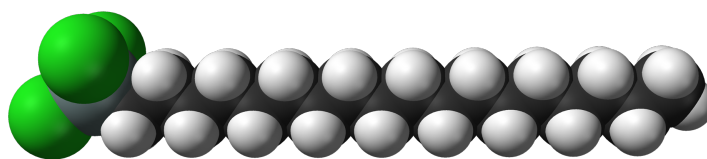
Figure 2.4: Scheme of an OTS molecule with chlorine atoms colored in green, silicon in grey, carbon in black and hydrogen in white. [159]

2.2.3 Adsorption Processes

Interfaces do not only affect the structure of interfacial water, but also have an influence on molecules solved in water. For example, in the presence of a solid-liquid interface, molecules tend to adsorb on this interfaces due to minimization of the total energy of the system [56, 160, 58]. Therefore, the properties of the solid surface play an important role in the adsorption process. In the case of proteins, a differentiation between hydrophilic and hydrophobic surfaces is necessary. On hydrophilic surfaces, the hydration shell of the protein comes in contact with the surface and thus the protein is able to keep its native form [83, 74]. This is not possible in the case of hydrophobic surfaces. Here, the hydration shell can not interact with the non-polar surface. Due to the hydrophobic effect, it is energetically favorable for the protein to unfold [161]. Thereafter, the hydrophobic areas of the protein, which are kept in the inner area of the protein in the native form, can adsorb on the non-polar surface, while the hydrophilic areas of the protein are pointing towards the liquid phase. This process changes the properties of the hydrophobic surface significantly, making it lose its hydrophobicity [162, 68]. Due to the strong interaction of the hydrophobic surface with proteins, this irreversible adsorption process under denaturation of the protein is very favorable when proteins come in contact with hydrophobic surfaces [68]. This adsorption process is schematically illustrated in figure 2.5.

Another approach on the description of the adsorption process is the thermodynamic point of view with the adsorption process being driven by enthalpy and entropy of the system [164]. Spontaneous adsorption of a protein occurs in the case when more energy is released from the system than gained, which can be described by the change of Gibbs
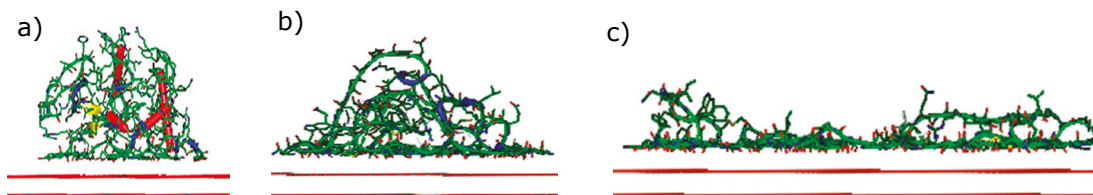
Figure 2.5: Different adsorption states of lysozyme on graphite. a) Most favorable adsorption geometry of lysozyme on graphite in the initial stage. b) Final metastable state of lysozyme on graphite under loss of secondary structure. c) Final, unfolded state of lysozyme on graphite. [163]

law of free energy via [92, 165]

$$\Delta G = \Delta H - T\Delta S \qquad (2.2)$$

with Gibbs free energy G, the enthalpy H, the entropy S and the temperature T of the system. When energy is released from the system, ΔG is smaller than zero and spontaneous adsorption occurs. Since these parameters are strongly affected by the thermodynamic properties of the system, those properties have a crucial impact on the adsorption process [164].

The adsorption behavior of lysozyme at solid interfaces was already subject of earlier studies. As an example, Kiesel et al. investigated the adsorption behavior of lysozyme on silicon oxide as a function of temperature [74]. In this study, with rising temperature, being still below the denaturation temperature, a higher amount of lysozyme adsorbed on silicon oxide. However, for temperatures above the denaturation temperature, the adsorbed amount of lysozyme on silicon oxide increased drastically compared to temperatures below the denaturation temperature, resulting in a large amount of adsorbed lysozyme on silicon oxide. These results will be compared to measurements on titanium oxide performed in this thesis. Furthermore, the influence of further thermodynamic properties like pressure and pH value of the aqueous solution on the adsorption of lysozyme on titanium oxide will be investigated in this thesis.

Chapter 3

Adsorption processes at solid-liquid interfaces

When an aqueous solution comes in contact with solids, the solid-liquid interface develops as a boundary between the solid and the liquid phase. Solutes like proteins as well as ions, that are dissolved in water, adsorb at solid-liquid interfaces. To investigate these adsorption processes at solid-liquid interfaces *in-situ* with atomic resolution, X-ray reflectivity (XRR) has been established as a powerful technique. XRR provides information on interfacial properties such as electron density, thickness and roughness of such (multi-) layer systems, combined in an electron density profile (EDP). Using high energy X-rays at a high photon flux allows the utilization of complex sample environments that are necessary to investigate the adsorption process under different thermodynamic conditions such as high temperature or high pressure. Thus, XRR is the method of choice in the framework of this thesis.

First, the theoretical background of the XRR method is presented in this chapter, followed by experimental details of XRR measurements to investigate the adsorption behavior of lysozyme on titanium oxide as well as ions on OTS. Afterwards, results of these measurements are presented and discussed.

3.1 Theoretical Background

In this section, the theoretical background of the X-ray reflectivity method is discussed. First, the scattering geometry will be presented. Second, a theoretical description of the reflectivity process at the simplest possible system, a smooth surface, is shown. Afterwards, the theory of XRR of more realistic and complex systems like rough systems and multilayer systems is discussed. As X-ray reflectivity is a well understood technique and part of many textbooks, this chapter only shows an overview based on the textbooks of M. Tolan [166], J. Als-Nielsen and D. McMorrow [167].

3.1.1 The Scattering Geometry

A scheme of the scattering geometry of an XRR experiment is shown in figure 3.1. An incident X-ray beam with the wave vector $\mathbf{k}_i$ impinges the sample at an angle α_i. It is then scattered with the wave vector $\mathbf{k}_f$ at the angle α_f between scattered beam and sample surface as well as the angle ϕ between the plane of the incident beam and surface normal, while another part of the beam is transmitted into the sample with the wave vector $\mathbf{k}_t$ under the angle α_t. In an XRR experiment, the angle α_f is equal to the incident angle ($\alpha_f = \alpha_i$) and the angle ϕ is equal to zero (in-plane scattering).
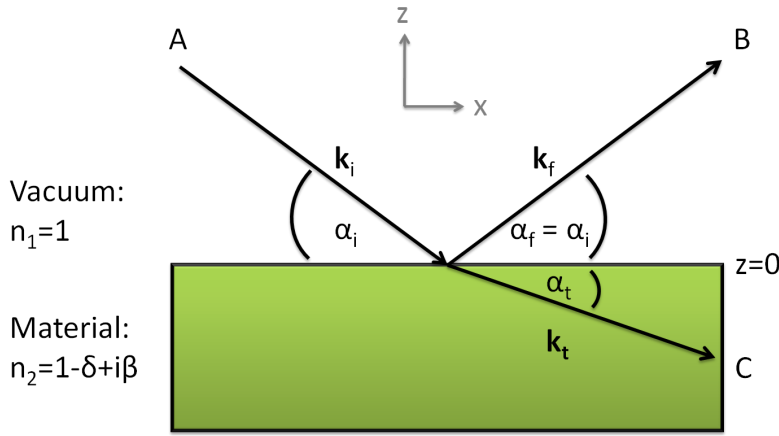
Figure 3.1: Scheme of the reflection and transmission geometry of an electromagnetic wave, based on Tolan [166].

The momentum transfer $\mathbf{q} = \mathbf{k}_f - \mathbf{k}_i$ can be calculated via

$$\mathbf{q} = \begin{pmatrix} q_x \\ q_y \\ q_z \end{pmatrix} = |\mathbf{k}_i| \begin{pmatrix} \cos(\alpha_f)\,\cos(\phi) - \cos(\alpha_i) \\ \cos(\alpha_f)\,\sin(\phi) \\ \sin(\alpha_f) + \sin(\alpha_i) \end{pmatrix} \tag{3.1}$$

with $|\mathbf{k}_i| = \frac{2\pi}{\lambda}$ and λ as the wave length of the incident beam. Due to the XRR geometry ($\alpha_f = \alpha_i$ and $\phi = 0$), only the component q_z perpendicular to the sample surface contributes to the momentum transfer, which can be thus described as $q_z = \frac{4\pi}{\lambda}\sin(\alpha_i)$. Hence, XRR data contains only information on the laterally averaged electron density profile of an interface.

3.1.2 Smooth Surfaces

The main goal of XRR experiments is to characterize the investigated sample by determination of its electron density profile in vertical direction. Here, the sample can be described as a solid state body consisting of an arrangement of atoms that act as

harmonic oscillators with resonance frequencies ω_j. Since the frequency of the incident beam ω is much higher than ω_j, the index of refraction is given by

$$n = 1 - \delta + \imath\beta = 1 - \frac{\lambda^2}{2\pi}r_0\rho + \imath\frac{\lambda}{4\pi}\mu \qquad (3.2)$$

with the so-called dispersion δ, the absorption β, the classical electron radius r_0, the electron density ρ and the linear absorption coefficient μ. The dispersion is usually in the range from 10^{-5} to 10^{-8}, while the absorption is typically one to three orders of magnitude smaller for sample systems used in XRR experiments in the framework of this thesis.

At smooth surfaces, the condition of continuous electromagnetic waves is fulfilled, leading to Fresnel's formulas for the reflectivity coefficient r and transmission coefficient t:

$$r = \frac{k_{i,z} - k_{t,z}}{k_{i,z} + k_{t,z}}, \qquad t = \frac{2k_{i,z}}{k_{i,z} + k_{t,z}}. \qquad (3.3)$$

Since the real part of the index of refraction is almost one, differences between the polarization planes can be neglected. Moreover, there is a critical angle α_c below which external total reflection occurs. Using Snell's law and a Taylor expansion for the transmission angle α_t results in the approximation $\alpha_c \approx \sqrt{2\delta}$.

The reflected intensity R is given by $R = |r|^2$, while the transmission is $T = |t^2|$. In the case of sharp and smooth surfaces, the reflected intensity is called Fresnel reflectivity R_F and the transmitted intensity Fresnel transmission T_F. Examples for Fresnel reflectivity and transmission are shown in figure 3.2. The Fresnel reflectivity can be characterized by $R_F = 1$ for $\alpha_i < \alpha_c$ and $R_F \approx \left(\frac{\alpha_c}{2\alpha_i}\right)^4$ for $\alpha_i > 3\alpha_c$.

Since real sample systems are not perfectly smooth and may consist of more than one layer, the next subsection deals with the influence of multilayers and roughness on the reflectivity data.

3.1.3 Real Surfaces and Interfaces

In the case of real surfaces and interfaces, roughness effects have to be taken into account. As shown in figure 3.3, EDPs of perfectly smooth surfaces have a discontinuity in the transition region between two different media. However, since XRR data provides only laterally averaged information, the transition region of rough interfaces can be described as an ensemble of smooth surfaces with continuously varied refractive index $n_j(z)$. This transition region is schematically shown in figure 3.4. The electron density profile becomes continuous and the transition region can be described by a Gaussian error function, where the full width at half maximum of the transition region is the root-mean-square (rms) roughness σ.

Hence, the reflectivity of rough surfaces is described by

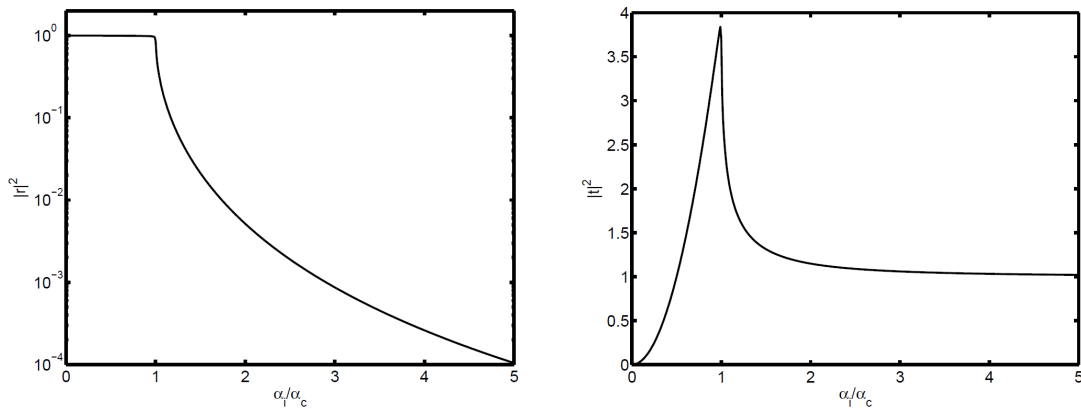$$R(q_z) = R_F e^{-q_z^2\sigma^2}, \qquad (3.4)$$

Figure 3.2: Fresnel reflection and Fresnel transmission as a function of normalized incident angle [168].
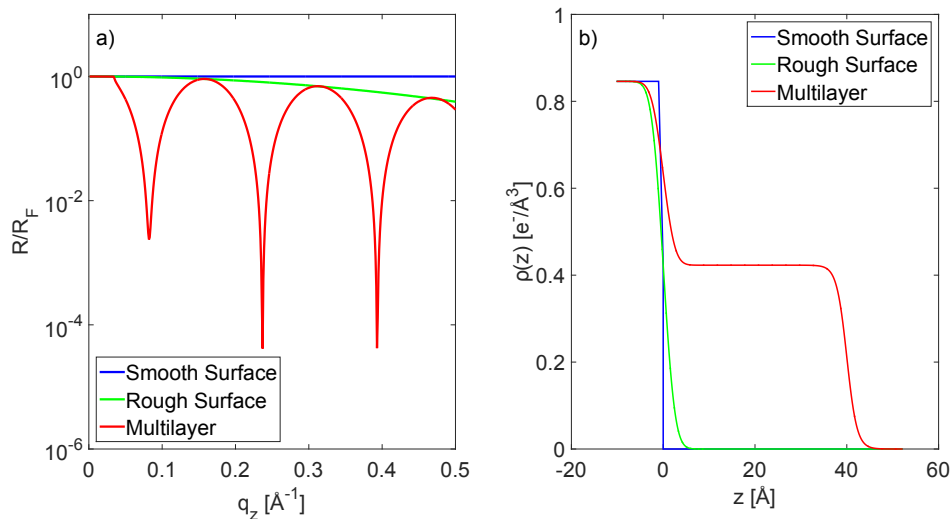

Figure 3.3: a) Reflected intensity of a smooth (blue), rough (green) and multilayer (red) system divided by the Fresnel reflectivity. The data was calculated from electron density profiles shown in b). b) Electron density profiles of the corresponding reflectivities shown in a).

leading to a damping of the reflected intensity in comparison with the Fresnel reflectivity at high incident angles. Due to the fact that the Fresnel reflectivity spans over several orders of magnitude for a typical XRR experiment, a high photon flux is necessary.

Moreover, real systems mostly consist of more than one layer. An approach to calculate the reflectivity of multilayer systems was presented 1954 by L. G. Parratt [170]. Here,
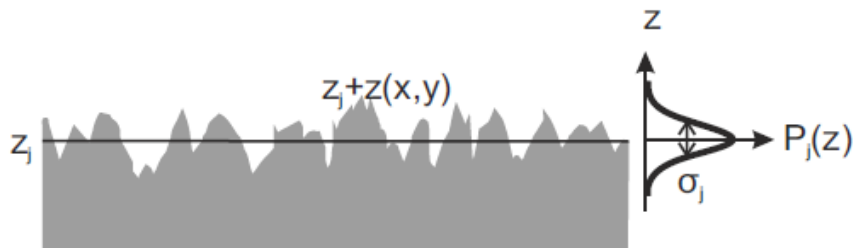
Figure 3.4: Scheme of the determination of the roughness at a rough interface. [169]

at each of the N layers of the multilayer system the incident beam is both reflected and transmitted. The part of the beam transmitted at the first layer becomes the incident beam for the second layer, which is both reflected and transmitted, too. Since the last layer is the bulk material, the transmitted beam at this layer is adsorbed and thus can be neglected. Henceforth, the reflectivity can be recursively calculated beginning with the reflected beam at the last layer. Interferences between reflected beams at different layers lead to so-called Kiessing fringes [171] in the reflectivity curve (see figure 3.3). Combining the Parratt's algorithm with modified Fresnel coefficients, one may calculate the reflectivity of rough multilayer systems. However, the roughness has to be much smaller than the layer thickness, since otherwise discontinuities in the electron density profile occur. To prevent these discontinuities, the electron density profile is divided into thin slices that can be calculated by Parratt's algorithm. This procedure is called the effective density model, which is able to characterize real systems.

An alternative approach is formulated within the kinematical or first-order Born approximation, where only single scattering events are taken into account. This allows to describe the scattering amplitude as the Fourier transform of the vertical electron density $\rho(z)$ via

$$R(q_z) = R_F(q_z) \left| \frac{1}{\rho_\infty - \rho_{solution}} \int \frac{\mathrm{d}\rho(z)}{\mathrm{d}z} e^{iq_z z} \mathrm{d}z \right|^2 \tag{3.5}$$

with $\rho_\infty - \rho_{solution}$ as the difference between the bulk electron density of the substrate and the solution. However, since the q_z range in an experiment is limited, the resulting electron density profile is not unique. Moreover, calculations using the kinematical approximation show differences towards experimental data at low q_z values and a direct inverse Fourier transform is impossible due to the square of the absolute value of the integral, since all phase information is lost.

As shown in this section, XRR is a powerful technique to obtain information on roughness, layer thicknesses and electron density differences in multilayer systems. However, the roughness of the investigated samples plays an important role, since for rough systems the reflected intensity is decreasing exponentially. Moreover, for large q_z-values the intensity is proportional to q_z^{-4}. Therefore, to access a large q_z range, high photon flux is necessary. In the case of solid-liquid interfaces, as investigated in this work, it is also necessary for the incident beam to pass through a water layer and fulfill other

requirements, as described in the following section.

3.2 Experimental Details

From the technical point of view, a parallel well focused, monochromatic x-ray beam that offers a high flux of highly energetic photons has to be provided to perform XRR experiments at solid-liquid interfaces. Therefore, the experiments shown in the framework of this thesis were performed at third generation synchrotron radiation sources, which are introduced in the following subsection. Subsequently, the used sample systems are presented. There is a set of requirements for the sample cells as well as the used samples that are illustrated in the sample systems section. Finally, the experimental procedure is described in the last part of this section.

3.2.1 Experimental Facilities

In the framework of this thesis, experiments were performed at beamlines of four different synchrotron radiation sources: BL9 at DELTA (Dortmund, Germany), P08 at PETRA III (Hamburg, Germany), MS-X04SA at SLS (Villigen, Switzerland) and ID31 at ESRF (Grenoble, France). Since the experimental setups at these beamlines are similar, only the example of beamline BL9 at DELTA will be discussed in detail.

Beamline BL9 at DELTA, Dortmund, Germany:
As presented by Paulus et al. [172] (see also [173, 174, 175]) and schematically shown in figure 3.5, beamline BL9 of DELTA (**D**ortmunder **EL**ek**T**ronenspeicherring-**A**nlage) produces X-rays by a superconducting asymmetric wiggler, which operates at a critical energy of 7.9 keV. The optical elements of the beamline are optimized to operate at a photon energy of up to 27 keV, providing a photon flux of 7×10^8 photons per second and square millimeter at a storage ring current of 100 mA (storage ring energy: 1.5 GeV). This energy is ideal to investigate biological materials like proteins because of a minimized radiation damage in the energy region around 25 keV [176], but with the energy being still high enough to pass through a water phase with a thickness of 1 cm. Afterwards, the X-rays are monochromatized by a silicon (311) double-crystal monochromator, leading to an energy resolution of $\Delta E/E = 10^{-4}$. To collimate the beam as well as define the beam size, a slit system consisting of three slits (c, e and g in figure 3.5) is installed, of which the first two slits collimate the X-ray beam vertically, while the third slit defines the vertical size of the beam to 0.2 mm, leading to a final beam size of 0.2 mm × 1 mm (V × H) at the sample position. The slits e and g enclose an auto-absorber system that limits the photon flux and thus the amount of photons incoming at the sample that is monitored by the NaI detector monitors d and h. The sample is located in the sample cell at the position i. Since during XRR experiments the intensity is recorded as a function of incident angle with the reflected angle being equal to the incident angle, the experiments are performed in Θ - 2Θ geometry. The incident angle arises from the rotation of the sample stage, while the reflected angle occurs from a rotation of the detector, which is twice as high as the rotation of the

sample. After being reflected at the sample, the X-ray beam passes through a slit system (j), which suppresses diffuse scattering. Finally, the reflected intensity is detected by a Pilatus 100K area detector (k), so that it is possible to detect both the reflected intensity and diffuse scattering simultaneously. At BL9, the adsorption of lysozyme on titanium oxide was investigated as a function of different thermodynamic conditions. With the presented setup, it took 20 minutes to conduct an XRR measurement.
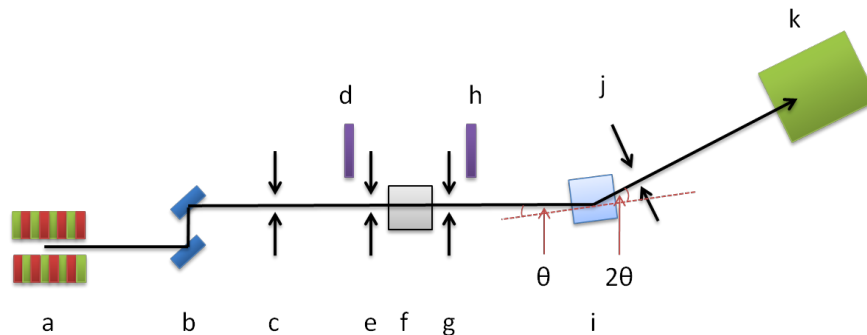
Figure 3.5: Schematic setup of the beamline BL9 at DELTA, based on Paulus [172]. Components: a: superconducting asymmetric wiggler, b: silicon (311) double-crystal monochromator, c, e, g, j: slit systems, d, h: detector monitors, f: auto-absorber system, i: sample cell, k: Pilatus 100K area detector.

The presented setup is typical for performing XRR experiments at synchrotron radiation sources. In the following, major differences between the other used experimental facilities and the already presented beamline will be shown.

Beamline ID31 at ESRF, Grenoble, France:
Lysozyme adsorption on titanium oxide interfaces was also investigated at the beamline ID31 of the ESRF (**E**uropean **S**ynchrotron **R**adiation **F**acility) (see ID31 Homepage for detailed beamline setup [177]). The ESRF operates at a storage ring energy of 6 GeV with a current of 200 mA[178]. This beamline is specialized in high energy X-ray scattering and thus a setup with an incident photon energy of 70 keV and a beam size of 0.005 mm × 0.04 mm (V × H) was used. Using the high flux of the beamline has to be done carefully because of the risk of beam damage in the sample. Especially the investigation of solid-liquid interfaces is prone to beam damage [179, 180] due to the fact that X-rays produce radicals in water, which alters the water structure and the structure of the hydration shell of the proteins. Therefore, the counting time at high incident angles was reduced along with an increase in angle step size and absorber plate thickness. At beamline ID31, the pressure-dependent adsorption behavior of lysozyme on titanium oxide was investigated with a scan duration of 3 minutes per scan.

Beamline X04SA at SLS, Villingen, Switzerland:
The setup of the beamline X04SA of the SLS (**S**wiss **L**ight **S**ource) is described in de-

tail by Willmott et al. [181] and Patterson et al. [182]. To perform experiments in the framework of this thesis, the surface diffraction end station of the beamline was used. This beamline provides a significantly higher photon flux than BL9 at DELTA due to the higher storage ring energy (2.4 GeV) and current (400 mA, top-up operation mode), as well as the use of an undulator instead of a wiggler as insertion device, resulting in a maximum flux of $> 10^{13}$ photons per second at an incident energy of 12 keV. However, since an incident energy of 25 keV (resolution: $\Delta E/E = 1.4 \cdot 10^{-4}$) was used at a beam size of 0.05 mm $\times$ 0.2 mm (V $\times$ H), the incoming photon flux at the sample was reduced. The reflectivity data was recorded by a Pilatus 100K detector. This setup is well suited for the investigation of ions at hydrophobic interfaces, resulting in a recording time of less than 10 minutes for each scan.

Beamline P08 at PETRA III, Hamburg, Germany:
The adsorption of ions at hydrophobic interfaces was also investigated at beamline P08 of PETRA III (**P**ositron-**E**lektron-**T**andem-**R**ing-**A**nlage) [183]. This synchrotron radiation source operates at a storage ring energy of 6 GeV and a beam current of 100 mA. Thus, with the present devices of beamline P08, a maximal flux of $2 \cdot 10^{13}$ photons per second at an incident energy of 8.4 keV is achievable. However, the needed incident energy of this experiment is higher due to the requirement of passing a water layer of 1 cm thickness. Therefore, an incident energy of 25 keV was chosen. The beam size was set to 0.05 mm $\times$ 0.1 mm (V $\times$ H) and a Pilatus 100K detector was chosen to record the reflectivity. With this setup, 10 minutes were necessary to perform an XRR measurement.

3.2.2 Sample Systems

This subsection introduces the sample systems that were investigated in the framework of this thesis. In a first study, the adsorption of lysozyme on titanium oxide surfaces was studied as a function of temperature, pressure, pH value and titanium oxide layer thickness. The second study deals with the investigation of the adsorption behavior of several kinds of ions on the hydrophobic surface of an OTS layer at ambient conditions.

Lysozyme on Titanium Oxide:

Very smooth silicon wafers (roughness: (2 ± 0.5) Å) with a native silicon oxide layer with a thickness of 1 nm and a roughness of (3 ± 1) Å were purchased from Wacker Siltronic (Burghausen, Germany) and used as substrate material. Titanium oxide layers were deposited on top by means of atomic layer deposition (ALD) [85, 86]. The titanium oxide was produced using $TiCl_4$ and H_2O. This technique allows to deposit titanium oxide layer by layer on top of the silicon wafer, keeping the roughness of the titanium oxide layer small. Thus, silicon wafers with titanium oxide coating layer thicknesses with the dimensions of 50 Å, 60 Å, 80 Å (each layer with a roughness of 4 Å,

respectively) and 115 Å (roughness: 6 Å)[1] were produced. In this case, the structure of the titanium oxide is amorphous [184]. To characterize the sample surface for surface defects, atomic force microscopy (AFM, see [185, 186] for further details) snapshots of the sample surface were taken (see figure A.1 in the appendix). These snapshots show a complete surface coverage of the titanium oxide. Prior to use, the wafers were cut into 10×19 mm^2 pieces, cleaned for 5 minutes in an ultrasonic bath and rinsed with ultrapure water.

Lysozyme was used as a model protein for investigating the adsorption behavior of proteins on titanium oxide. The adsorption behavior of this protein was already investigated on silica surfaces as a function of temperature [74] and is thus a well suited protein to be investigated on titanium oxide. The results of the investigation shown in this thesis will be compared to the study of Kiesel et al. [74]. Lysozyme was purchased from Sigma-Aldrich (Taufkirchen, Germany) as lyophilized powder and was used as received. This protein is obtained from hen egg white and can be described as a prolate ellipsoid with dimensions of $30 \times 30 \times 45$ Å^3 [152], having an isoelectric point (IEP) at pH 11 [153]. To obtain an aqueous protein solution, lysozyme was solved in an aqueous buffer solution yielding a protein concentration of 1 mg/mL. In case of temperature-dependent measurements, a 10 mM phosphate buffer at pH 7 was used, while for pressure-dependent measurements a pressure stable 20 mM BisTris buffer was chosen [187] at pH 7.1. At this conditions, the zeta potential of the titanium oxide layer is slightly negative. For pH-dependent measurements, lysozyme was dissolved in ultrapure water and the pH value was adjusted by the addition of HCl or NaOH.

Ions at Hydrophobic Interfaces:

To produce hydrophobic OTS-coated wafers, silicon wafers were used as substrate material and coated by the subsequently presented procedure. This preparation is described in detail by Paul Salmen [78] and is slightly different from other known methods [48, 188]. All chemicals used in this subsection were purchased from Sigma-Aldrich (Taufkirchen, Germany).

First, silicon wafers are cut into 10×19 mm^2 pieces and cleaned in isopropanol, acetone, and chloroform, 15 minutes in a supersonic bath, respectively. Afterwards, the wafers are put into a mixture of hydrogen peroxide (1/3) and sulfuric acid (2/3), in which they stay for 45 minutes. This mixture removes organic residues and etches the surface of the wafer, whereby silanol groups are generated at the surface. Afterwards, the wafers are cleaned in three water baths to remove the mixture from the surface of the wafer. With this method, the wafers are hydrophilized offering a contact angle below 10 °, which is necessary for a proper deposition of OTS molecules. In the next step, the wafers are dried by an argon flow. This method keeps the silanol groups on the surface of the wafer intact [189] and allows a smooth growth of OTS monolayers. Afterwards, the dry wafers are placed into a mixture of chloroform (1/3, water-free)

---

[1]The titanium coating was produced by Tobias Gahlmann and Dr. Andreas Behrendt, Institute of Electronic Devices, University of Wuppertal, 42119 Wuppertal, Germany

23

and hexane (2/3, water-free) with 1 mM OTS. Since this mixture is water-free, OTS head groups can only form a bond with the surface of the wafer, leading to a silicon oxide monolayer at the surface, while the non-polar OTS tail groups are pointing away from the surface. This procedure takes at least 12 hours. Afterwards, the wafers are finally cleaned several times alternatingly in toluol and hexane baths to remove OTS residues. The wafers are now hydrophobic with a homogeneous surface [78] and can be stored at room conditions. Prior to use, the wafers are cleaned in isopropanol in an ultrasonic bath.

To investigate the adsorption of ions at OTS wafers, ions were produced by dissolving salt in ultrapure water. Different compounds were chosen to study the adsorption behavior as a function of ion size and position in the Hofmeister series [190, 147, 191]. Therefore, several combinations of alkali metals and halogens were chosen as well as alkali metals and hydroxides. These compounds with a purity of at least 99.9% were purchased from Sigma-Aldrich (Taufkirchen, Germany): NaCl, NaBr, NaI, HCl, LiCl, KCl, RbCl, CsCl, LiOH, NaOH, KOH, RbOH and CsOH. Further details on these compounds are presented in section 2.1.1.

3.2.3   Sample Environment

In order to study the adsorption behavior of proteins on titanium oxide as well as ions on OTS, three different custom made sample cells were used for different thermodynamic conditions. These sample cells are presented in this subsection in detail.

Pressure Variation

Pressure-dependent measurements were performed in an already existing sample cell, which is schematically shown in figure 3.6 a). This sample cell was introduced by Wirkert et al. [192] and allows to measure a sample volume of about 375 μL in a pressure range between 50 bar and 5 kbar by XRR.

To resist the high pressure, the outer sample cell with the dimensions 98 mm $\times$ 90 mm $\times$ 80 mm (length in beam direction $\times$ width $\times$ height) consists of high-strength stainless steel (type 2.4668, $NiCr_{19}Fe_{19}Nb_5Mo_3$). Two synthetic diamond windows (marked with the letter W and D in figure 3.6 a)) with a thickness of 1 mm and a diameter of 6 mm are located concentrically along the beam path. Because of the strong absorption of the windows as well as the sample liquid, high photon energies (> 20 keV) are required [172]. This is fulfilled at all experimental stations (see 3.2.1). XRR measurements at a maximum angle of incidence of 7.7 $^\circ$ at a beam height of 0.1 mm can be performed. The sample is placed in the inner cell (see figure 3.6 b)) and is then placed in the opening O (see figure 3.6 a)) of the outer cell. The inner cell consists itself of three elements: the sample holder (B in figure 3.6 b)), a breech (A in figure 3.6 b)) and a casing (C in figure 3.6 b)) with Kapton windows (K in figure 3.6 b)). First, the wafer (maximum size 7.5 mm $\times$ 7.5 mm) is placed in the sample holder and fixed with a screw (S in figure 3.6 b)). Afterwards, the casing is filled with the sample liquid, while the sample holder is placed inside and locked with the breech. To prevent the Kapton window from
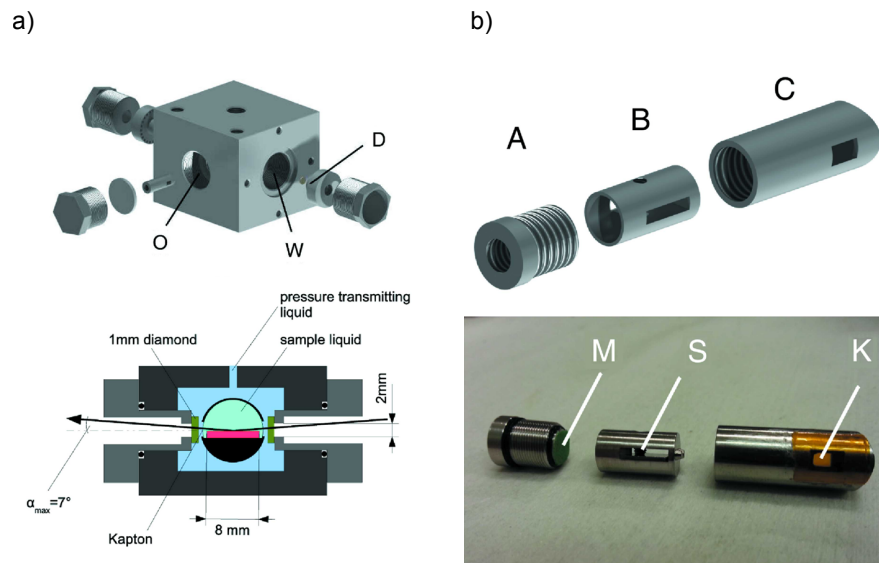
Figure 3.6: Schematic setup of the high pressure sample cell, published by Wirkert et al. [192]. a) Sketch of the sample cell and scheme of the scattering geometry: The opening of the beam path W through the diamond windows D as well as the opening for the inner sample cell O are highlighted in the upper part of the figure. The lower part of the figure shows the beam path through the sample cell. b) Scheme and photograph of the inner sample cell with the breech (A) incl. rubber membrane M, sample holder B incl. screw S to fix the sample and cover plate C incl. Kapton windows K.

rupture by applying pressure (because of the volume change of the sample liquid), a rubber membrane (M in figure 3.6 b)) is spanned over the boring of the breech. After placing the inner sample cell inside the outer sample cell, pressure may be applied by filling the outer sample cell with pressure-transmitting material (water). By changing the amount of the pressure-transmitting material with a high pressure pump, the pressure applied on the sample may be altered. Additionally, installed pressure monitors track the pressure inside the pressure circuit.

Temperature Variation
In experiments, where the temperature was varied, a sample cell presented by Salmen [78] was used. This sample cell (see figure 3.7) consists of a stainless steel cell body with Kapton windows and stainless steel sample holder.

A wafer with dimensions of $10\,\text{mm} \times 19\,\text{mm}$ (length $\times$ width) is placed in the sample holder and fixed with PTFE plates on opposing sides of the holder. Thereafter, the sample holder is positioned inside the sample cell and mounted on a small pin to fix the location of the wafer inside the sample cell. This allows a fast alignment after wafer exchange. Afterwards, the interior of the cell may be filled with up to $10\,\text{mL}$ of the sample liquid. However, $4\,\text{mL}$ sample liquid are enough to perform XRR experiments on solid-liquid interfaces. If desired, an additional heat exchanger plate may be mounted
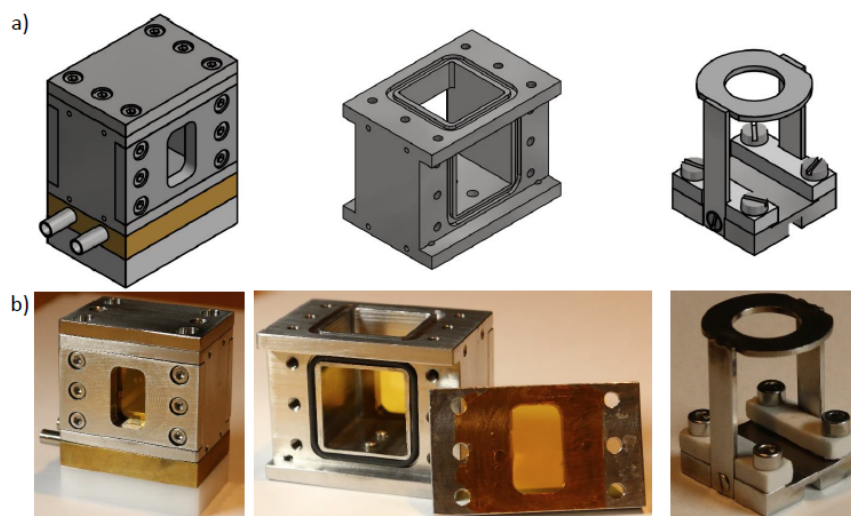
Figure 3.7: Scheme of the temperature variation sample cell [78]. a) Sketch of the whole sample cell (left), inner part of the sample cell (middle) and sample holder (right). b) Photographs of the cell components. [78]

below the sample cell to change the temperature of the sample by a continuous flow cooling/heating system.

Room Conditions Setup

A part of the experiments are performed at room conditions. In these experiments, the sample cell presented in figure 3.7 is used. However, during sample changes the cell has to be cleaned very carefully to ensure correct results. Therefore, to reduce the cleaning time a second sample cell was produced. This sample cell has the same layout as the sample cell shown in figure 3.7, but the body of the cell consists of PTFE, which may be cleaned significantly quicker. Photographs of the sample cell are shown in figure 3.8.
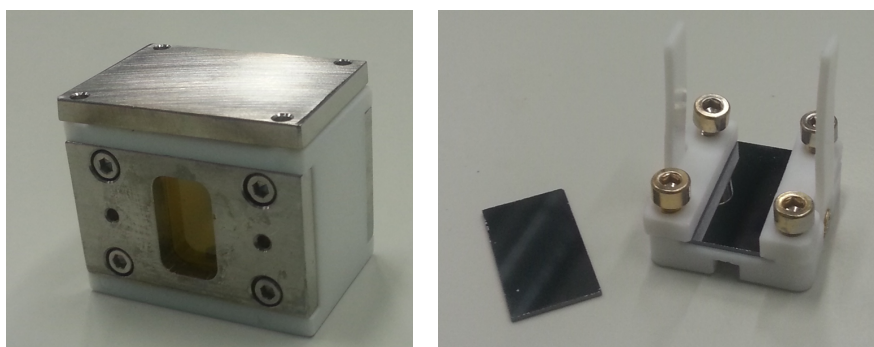
Figure 3.8: Photographs of the sample cell used for experiments at room conditions: Whole sample cell (left) and sample holder incl. wafers (right).

These sample cells are suitable to be used at all beamlines presented in section 3.2.1 to perform XRR experiments at solid-liquid interfaces. The analysis of the obtained XRR data is presented in the next section.

3.3 Data Treatment

In a first step of XRR data analysis, the raw data is corrected for its background by the subtraction of the transverse diffuse scan and normalized afterwards. Subsequently, the electron density profiles can be determined by minimizing the mean square deviation between the reflectivity data and a reflectivity curve that is calculated by Parratt's recursive algorithm [170] in combination with the effective density model [166], using a least-squares fitting routine. As presented beforehand in section 3.1, the EDP contains information on the layer thickness d, electron density ρ and interfacial roughness σ of each layer of the model system.

In the past, many studies were performed to investigate the EDP of silicon and silicon oxide interfaces (see e.g. references [193, 69, 106, 194]). It is widely accepted that for measurements at high momentum transfers the EDP of silicon and silicon oxide interfaces is best described by Steinrück et al. [194]. This model includes an area of lower density between the silicon and silicon oxide layer. However, due to the fact that most measurements presented in this chapter do not exceed a momentum transfer of $0.4\,\text{Å}^{-1}$, the resolution is not high enough to resolve this area. In this case, the EDP presented by Tidswell et al. [193] is the EDP of choice, describing the data most fittingly. Since the model systems as well as the analysis procedures differ from this point on for both studies, first the analysis of lysozyme adsorption on titanium oxide will be presented, followed by the study of the adsorption behavior of ions on OTS.

3.4 Lysozyme on Titanium Oxide

In the study of lysozyme adsorption on titanium oxide, the reference sample system (without protein) was modeled as follows: silicon was used as substrate material with a silicon oxide layer on top, followed by a titanium oxide layer and water. For measurements of lysozyme solution, one layer of adsorbed lysozyme was added on top of the titanium oxide layer. A fit to the data with more layers instead of a single slab for the protein, which often yields a better adaption of the fit [83], caused no improvements. Due to this, it was decided to keep the model system as simple as possible. Since no changes in the substrate material during protein adsorption are expected, the substrate parameters obtained from the reference measurements were kept fixed within the corresponding measurement series. Changes in the reflectivity data were expected to be produced by changes within the lysozyme layer. During pressure variation, the electron density of water changes significantly. Thus, this parameter was calculated for each pressure and kept constant during analysis.

With the electron density profiles of the pure water measurements $\rho_{ref}(z)$ and the lysozyme solution electron density profiles $\rho(z)$, the volume fraction profile $\phi(z)$ along

the surface normal can be calculated by

$$\phi(z) = \frac{\rho(z) - \rho_{\text{ref}}(z)}{\rho_{\text{lys}} - \rho_{\text{water}}} \tag{3.6}$$

where ρ_{lys} is the electron density of lysozyme, ρ_{water} the electron density of water (e.g. 0.334 $e^-/\text{Å}^3$ at ambient conditions) [195, 74] and $\phi(z)$ the lysozyme portion in the adsorption layer, which is assumed to be a composite of lysozyme and water. The value for ρ_{lys} was chosen as 0.49 $e^-/\text{Å}^3$. This value is calculated by Kiesel et al. [74] using the program package chimera [196, 197] on the basis of a PDB file without a hydration shell [152]. Other studies propose a lower electron density [83]). However, to keep the results of titanium oxide on a comparable level to silicon oxide, ρ_{lys} was set to 0.49 $e^-/\text{Å}^3$. The volume fraction profiles describe the surface coverage at position z, which can be used to calculate the adsorbed amount Γ of lysozyme via

$$\Gamma = \frac{m}{v} \int \phi(z)\mathrm{d}z \tag{3.7}$$

with the molar mass m (14.3 kg/mol) and molar volume v (9348 m^3/mol) of lysozyme [152]. Note that Γ represents the minimal adsorbed amount observable by XRR [83]. This analysis procedure is used for every measured XRR data series of lysozyme adsorption on titanium oxide for different thermodynamic conditions. The results of this study are already published in the journal Langmuir [91]. In the following, temperature-dependent measurements will be presented.

3.4.1 Temperature

Temperature-dependent XRR measurements of lysozyme on a 60 Å thick titanium oxide layer are shown in figure 3.9 a). The reflectivities were normalized by the Fresnel reflectivity of a smooth silicon-water interface.

Strong oscillations in the reflectivity data occur from the 60 Å thick titanium oxide layer. By inserting the lysozyme solution, both the minima positions and shapes vary slightly due to the adsorption of lysozyme on titanium oxide. As shown in the EDPs in figure 3.9 b), the increase of temperature results in an increase of electron density and layer thickness of the adsorbed lysozyme layer, and thus in a stronger adsorbance. The differences in the shapes of the reflectivity curves of figure 3.9 a) seem to be quite small at first sight. Thus, the temperature-dependent reflectivity data is compared to the measurements at 20 °C again in figure 3.10 to highlight the differences. It is obvious that with rising temperature, the minima are less pronounced and shifted to a lower q_z-value. This is due to a stronger adsorption of lysozyme on the titanium oxide surface.
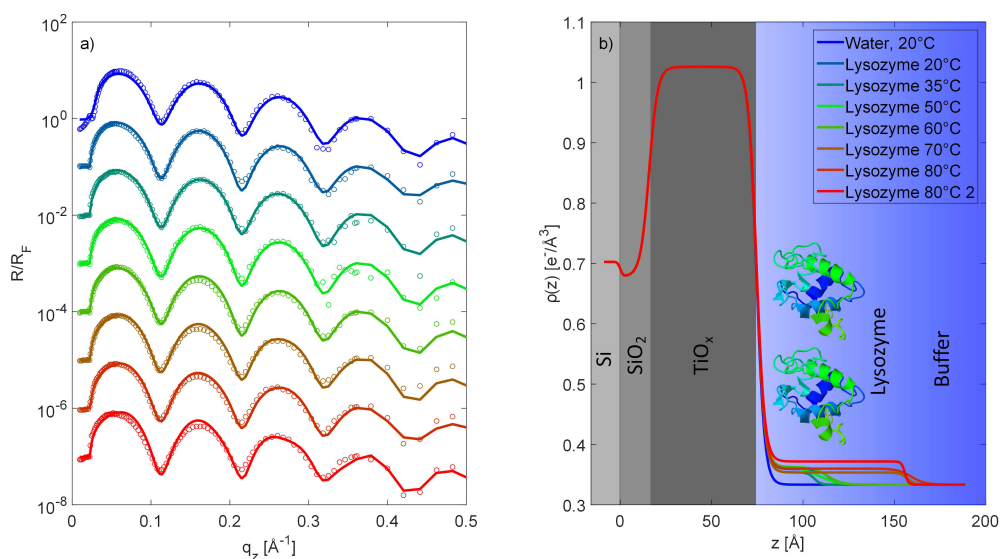
Figure 3.9: a) X-ray reflectivity data of a temperature series at ambient pressure. The measured data is displayed using open circles, while solid lines represent the fit to the data calculated from an optimized model system. The color scale corresponds to the legend in b). Lysozyme 80 °C 2 is the second measurement at 80 °C repeated one hour after the first measurement. The spectra are shifted on the y-scale for better visualization. b) Electron density profiles of the temperature series shown in a).
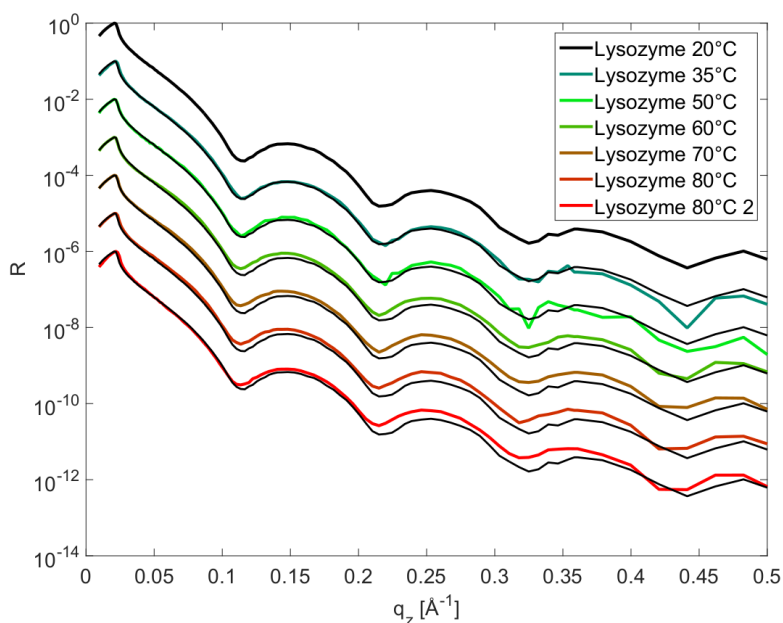

Figure 3.10: Temperature-dependent changes in the reflectivity data compared to the measurement at 20 °C (black). The spectra are shifted on the y-scale for better visualization.

For a better discussion of the results, volume fraction profiles and the adsorbed amount of lysozyme were calculated via equations 3.6 and 3.7. The volume fraction profiles of the temperature series are shown in figure 3.11 a), while the adsorbed amount of lysozyme is presented in figure 3.11 b). At a temperature of 20 °C, the adsorbed lysozyme layer has a thickness of 45 Å, which is equal to the length of the long axis of one lysozyme molecule. Hence, the adsorption with the long axis perpendicular to the sample surface seems to be preferred. However, the maximum surface coverage at this temperature is only 14%. With rising temperature up to 60 °C, only a slight increase in the surface coverage occurs. Changes in the shape of the lysozyme layer are observed starting from a temperature of 70 °C, which is close to the denaturation temperature of lysozyme (71 °C at pH 7 [198]). Here, an increase of layer thickness, which goes in hand with a decrease in layer density, is observable. While the overall surface coverage decreases
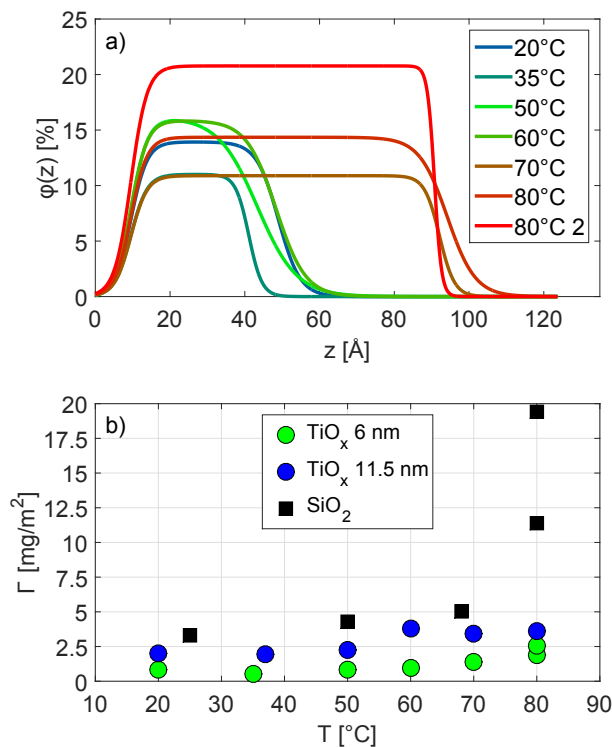
Figure 3.11: a) Volume fraction profiles of the temperature series shown in figure 3.9. b) Temperature-dependent adsorbed amount of lysozyme on titanium oxide. The green symbols correspond to the data shown in a) and figure 3.9, while the blue symbols correspond to a measurement on a thicker titanium oxide layer shown in figure 3.12. Moreover, to compare the results, the adsorbed amount of lysozyme on silicon oxide as previously published [74] is shown in black. The errorbars of the data points are smaller than the data points themselves (± 0.3 mg/m^2).

from 15.8% at 60 °C to 10.9% at 70 °C, a slight increase of adsorbed amount of lysozyme (see figure 3.11 b)) is observed. This behavior can be explained by a partial unfolding of the protein yielding lower electron densities and larger layer thicknesses. Due to this, a lower surface coverage is observed, since the surface coverage depends on the maximum density in the protein layer. The slight increase of Γ also points to an ongoing adsorption of proteins from the bulk phase. As the proteins tend to aggregate at high temperatures, a further increase of the temperature to 80 °C leads to an even higher amount of adsorbed lysozyme. This effect continues with proceeding time. A second measurement at 80 °C one hour after the first measurement reveals an even higher amount of adsorbed lysozyme on the titanium oxide surface. However, even in this measurement the adsorbed amount of lysozyme is still smaller than on silicon oxide as observed in a previous study [74].

To validate the results, a second temperature-dependent XRR series of lysozyme adsorption on titanium oxide was produced. This time, a thicker titanium oxide (115 Å) layer was chosen. The reflectivity data, as well as the EDPs and the volume fraction profiles are shown in figure 3.12. Here, the temperature-dependent behavior of lysozyme adsorption is analogous to the thinner titanium oxide layer (see figure 3.10 a)). In the temperature region between 20 °C and 50 °C, almost no change in the adsorbed amount of lysozyme is observable. However, for this sample system a significant increase in adsorbed lysozyme occurs already at 60 °C. This is different to the 60 Å thick titanium oxide layer, for which the temperature-dependent increase of the amount of the adsorbed lysozyme started at 70 °C. The EDPs and volume fraction profiles give
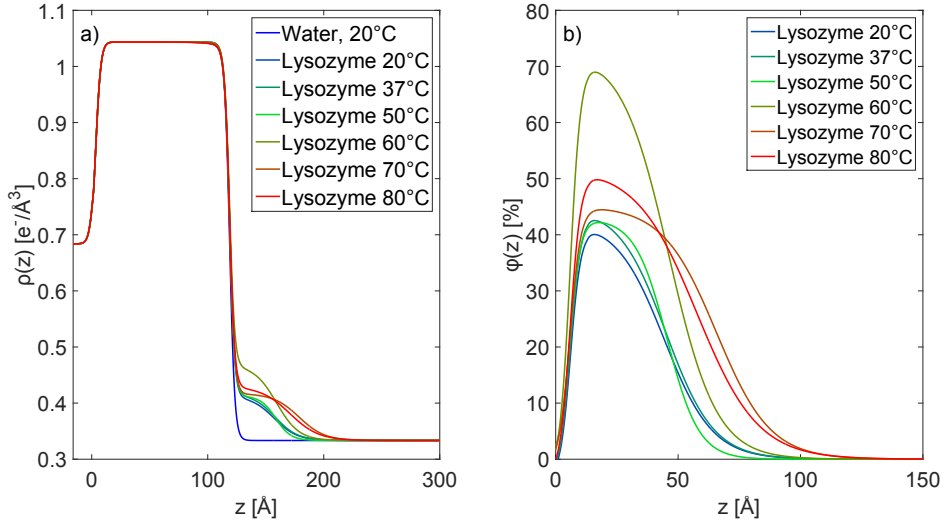
Figure 3.12: a) Electron density profiles of temperature-dependent adsorbed lysozyme amount on a 115 Å thick titanium oxide layer. b) Volume fraction profiles of the temperature series shown in a).

31

a hint on a rearrangement of the adsorbed lysozyme layer from a one layer to a two layer system due to the increase of the lysozyme layer thickness under an almost constant overall adsorbed amount of lysozyme. This rearrangement is completed at 70 °C. Here, compared to 60 °C, the amount of covered titanium oxide surface by lysozyme is smaller, but an increase in lysozyme layer thickness to a value of 90 Å is present. This layer thickness corresponds to the size of two lysozyme molecules. However, raising the temperature further to 80 °C does not lead to more lysozyme adsorption. The temperature-dependent adsorbed amount of lysozyme on this titanium oxide layer is also presented in figure 3.11 b) and compared to temperature-dependent adsorption of lysozyme at silicon oxide as well as on the thinner titanium oxide layer.

Even though the temperature-dependent adsorption behavior of lysozyme on titanium oxide is similar for both investigated titanium oxide layer thicknesses, the overall adsorbed amount varies as a function of titanium oxide layer thickness and is even in both cases smaller than the adsorbed amount of lysozyme on silicon oxide. This leads to the assumption that the lysozyme adsorption on titanium oxide covered silicon wafers is dependent on the titanium oxide layer thickness. This assumption will be further discussed in the next subsection.

3.4.2 Titanium Oxide Layer Thickness

To investigate the impact of titanium oxide layer thickness on the lysozyme adsorption at titanium oxide-water interfaces, XRR measurements on wafers with different titanium oxide layer thicknesses at room conditions were performed. The reflectivity data as well as the EDPs are shown in figure 3.13, while the volume fraction profiles and the adsorbed amount of lysozyme are shown in figure 3.14. Interestingly, there is a clear impact of the titanium oxide layer thickness on the adsorbed lysozyme amount. A thicker titanium oxide layer causes more lysozyme adsorption. This dependence might give a hint that Van der Waals interactions play an important role on the adsorption behavior of lysozyme on different surfaces [69].

In order to get an estimate of the Van der Waals contributions, the non-retarded Hamaker constants for two different sample geometries are calculated. First, the interaction between titanium oxide and lysozyme via water is analyzed. In this case, the Hamaker constant is calculated by [199]

$$A_{ijk} = (\sqrt{A_{ii}} - \sqrt{A_{kk}}) \cdot (\sqrt{A_{jj}} - \sqrt{A_{kk}}) \tag{3.8}$$

with the Hamaker constant of titanium dioxide $A_{ii} = 15.3 \cdot 10^{-20}$ J [200], the Hamaker constant of water $A_{kk} = 3.7 \cdot 10^{-20}$ J[199] and the Hamaker constant of lysozyme A_{jj}. A discussion on the interaction of lysozyme molecules in water is provided by Gripon et al. [201], leading to the value of $A_{jj} = 13.8 \cdot 10^{-20}$ J via equation 3.8. This approach yields $A_{ijk} = 3.6 \cdot 10^{-20}$ J, which indicates an attractive interaction. To estimate the effect of the silicon below the titanium oxide layer, the Hamaker constant for silicon interacting with lysozyme via titanium dioxide was calculated. Here, $A_{ii} = 18.5 \cdot 10^{-20}$ J for silicon was used [202]. This rough estimate yields a Hamaker constant of -8 · 10⁻²⁰ J, indicating a slight repulsive interaction. Thus, in the sample geometry used, the silicon
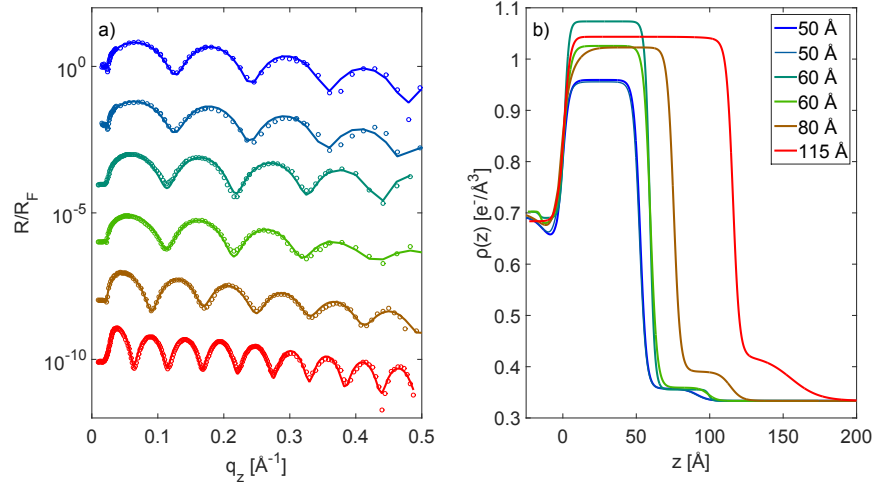
Figure 3.13: a) X-ray reflectivity data (circles) with fit (solid lines) of lysozyme adsorption on titanium oxide with different titanium oxide layer thicknesses at room conditions. b) Corresponding electron density profiles.
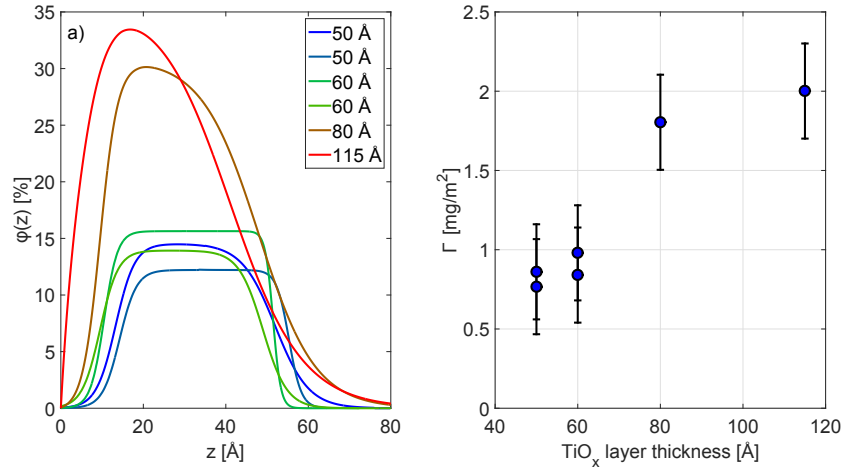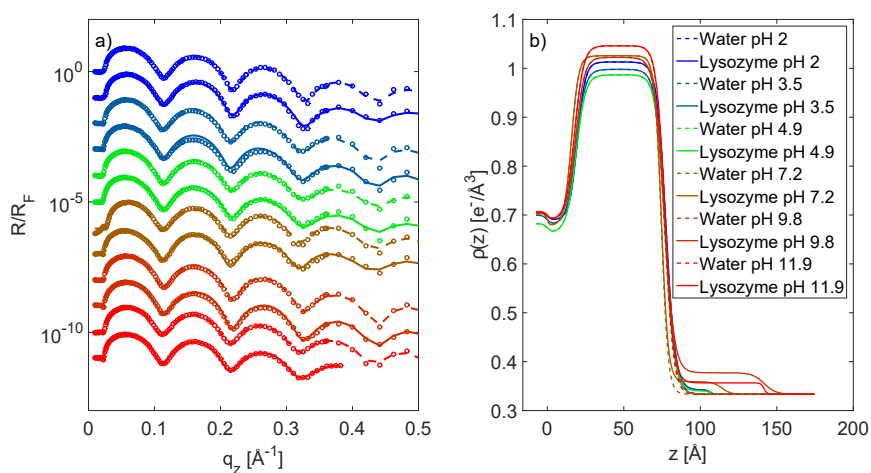

Figure 3.14: a) Volume fraction profiles of lysozyme adsorbed on titanium oxide with different titanium oxide layer thicknesses at room conditions. The electron density profiles are shown in figure 3.13 b). b) Adsorbed amount of lysozyme on titanium oxide as a function of titanium oxide layer thickness, calculated from the volume fraction profiles shown in a). The errorbars were estimated by variation of lysozyme layer fit parameters.

substrate appears to be repulsive, which might result in a reduced adsorption at low titanium oxide layer thicknesses.

To explain the weak adsorption in comparison to the silicon dioxide surface, surface charge effects have to be taken into account, since one of the key factors in the ad-

sorption process are electrostatic interactions. The experiments on silicon oxide and titanium oxide were performed at a pH value of 7±0.2. The IEP of silicon oxide is at a pH of 2.0 [203], while titanium oxide has its IEP around a pH value of 5 [204], resulting in a higher surface charge of silicon oxide at these experimental conditions and thus in a stronger attraction of lysozyme with an IEP at a pH of 11. A complete study on the pH dependence of lysozyme adsorption on titanium oxide surfaces will be presented in the next subsection.

3.4.3 pH value

The pH-dependent measurements of lysozyme adsorption and EDPs on a silicon wafer with a 60 Å thick titanium oxide coating at room conditions are shown in figure 3.15, while the corresponding volume fraction profiles and adsorbed lysozyme amounts are shown in figure 3.16.

Almost no lysozyme adsorbs at pH values below 5, since both the titanium oxide surface and lysozyme are positively charged. At a pH value of 7, which is higher than the IEP of titanium oxide, the titanium oxide surface is negatively charged. Here, the adsorption behavior of lysozyme was already shown in figure 3.11. The highest adsorbed amount occurs at a pH value of 9.8, where titanium oxide is strongly negatively charged, while lysozyme still carries a positive charge [205]. Even though the pH value difference for titanium oxide to the IEP is 4, which is equal to the difference of measurements of silicon oxide at pH 7 with an IEP at pH 3, there is still less lysozyme adsorbing than on silicon oxide. Consequently, the different adsorption behavior on silicon oxide and titanium oxide is not only occurring due to surface charge differences and thus has to be explained by material composition and structure [206, 69]. Raising the pH value
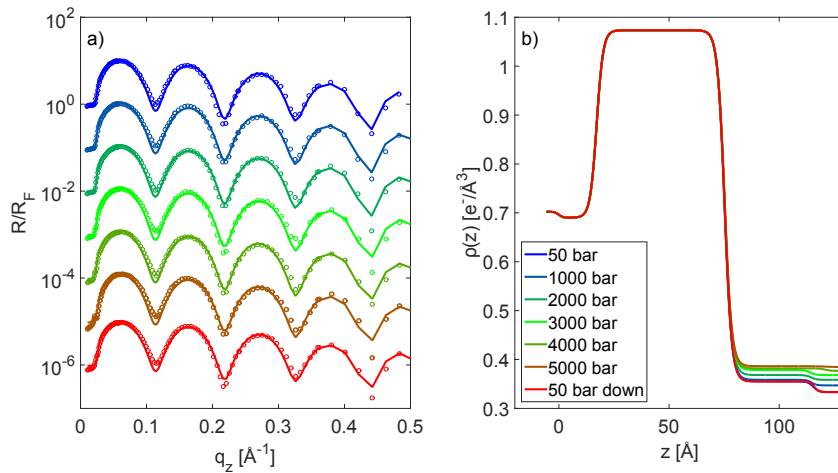

Figure 3.15: a) X-ray reflectivity data (circles) with fit (solid lines) of lysozyme adsorption on titanium oxide as a function of pH value at room conditions. b) Electron density profiles of the data shown in a).
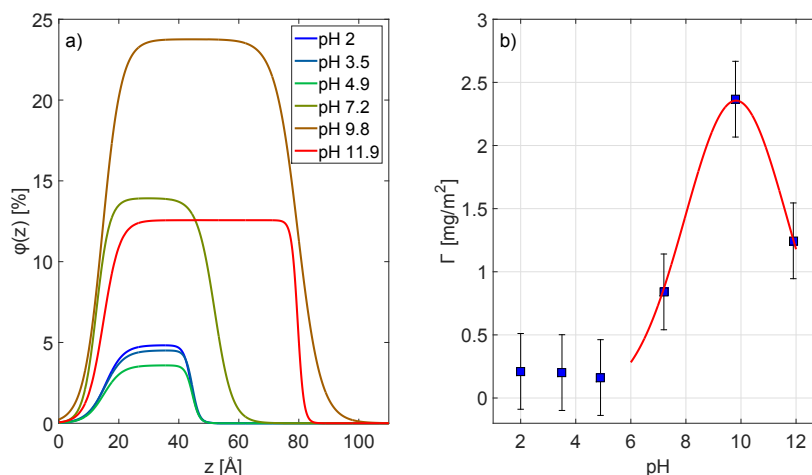
Figure 3.16: a) Volume fraction profiles of lysozyme adsorption on a 60 Å thick titanium oxide layer as a function of pH value at room conditions. The electron density profiles are shown in figure 3.15 b). b) Adsorbed amount of lysozyme on titanium oxide as a function of pH value. The errorbars were estimated by variation of lysozyme layer fit parameters. The red line is a guide to the eye to illustrate the behavior of the adsorbed amount of lysozyme as a function of pH.

further to 12 leads to less adsorption on titanium oxide. This pH value is beyond the IEP of lysozyme and thus lysozyme and the titanium oxide surface are not oppositely charged anymore.

With the pH-dependent data as well as the data of lysozyme adsorption on titanium oxide as a function of titanium oxide layer thickness, the different adsorption behavior of lysozyme on titanium oxide compared to silicon oxide can be described by differences in the material composition, structure and surface charge.

3.4.4 Pressure

Finally, pressure-dependent measurements on titanium oxide coated silicon wafers were performed. The results for measurements on a 60 Å thick titanium oxide layer are shown in figure 3.17 (reflectivity curves and EDPs) and figure 3.18. XRR data and EDPs of further pressure-dependent studies are shown in the annex in figures A.3, A.5 and A.7.

With rising pressure, lysozyme desorbs from the titanium oxide surface (see figure 3.18 a)). However, this effect is almost completely reversible by reducing pressure. The effect of pressure on proteins in solution is frequently discussed in literature. It was shown that high pressure has an impact on protein-protein interactions, protein activity, folding and hydration and on the formation of protein dimers and oligomers [207, 208, 209, 210, 211, 212]. Studies on protein adsorption under high hydrostatic pressure are rare [192, 213]. In general, the application of high pressure transfers the system under investigation into a state with reduced volume. This can cause a de-

Figure 3.17: a) X-ray reflectivity data (circles) with fit (solid lines) of lysozyme adsorption on titanium oxide as a function of pressure at room temperature. b) Corresponding electron density profiles.
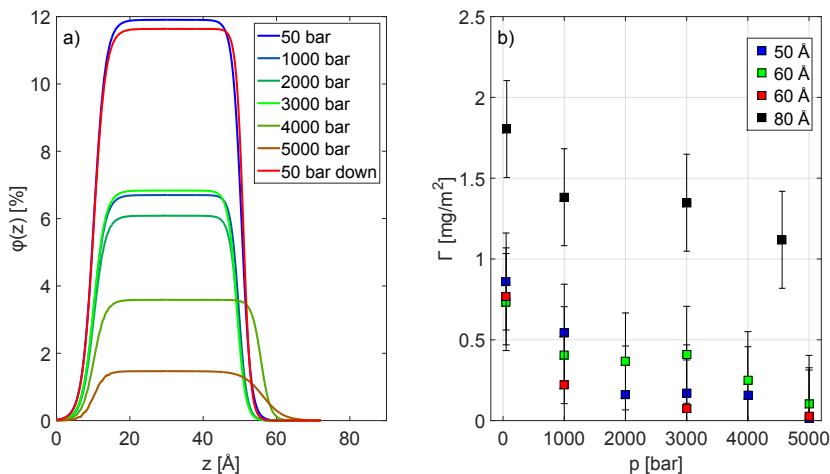

Figure 3.18: a) Volume fraction profiles of lysozyme adsorption on a 60 Å thick titanium oxide layer as a function of pressure at room temperature. The electron density profiles are shown in figure 3.17 b). b) Adsorbed amount of lysozyme on titanium oxide with different layer thicknesses between 50 Å and 80 Å as a function of pressure. The errorbars were estimated by variation of lysozyme layer fit parameters.

stabilization or denaturation of proteins, which might go in hand with an increased adsorption due to the interaction between hydrophobic parts of the protein and the surface. Moreover, the volume of the protein hydration shell and its density is changed [210], resulting in an overall reduction of the systems volume. As a consequence, a completely hydrated protein in bulk solution might be preferred compared to a weakly

bound protein offering a defective hydration shell towards the substrate. As lysozyme is very pressure stable, this scenario might explain the observed desorption.

With these results, a complete set of temperature, pressure and pH-dependent studies of lysozyme adsorption on titanium oxide layers with different layer thicknesses were presented and analyzed in this section. A final conclusion on these results will be presented together with the results of the study of ion adsorption on OTS in subsection 3.6.

3.5 Ions on OTS

The second part of this study explores the adsorption process of ions at a hydrophobic surface. The investigation of hydrophobic interfaces takes on greater importance in modern research [84, 214, 215]. Previously, OTS has often been subject of scientific interest, since this self-assembled monolayer has the property to generate spontaniously a hydrophobic surface on silicon [48, 105, 216, 217, 218]. Hence, the adsorption behavior of different substances on OTS was investigated [48, 219, 78]. However, the results of these experiments are controversially discussed and a complete description of the adsorption process is still pending. Especially the hydrophobic gap, a zone of low electron density at the interface between the OTS tail group and a liquid, is not yet completely understood [220, 221, 222, 49, 78]. In this study ions are solved in water, which may overcome the hydrophobic gap upon adsorption on OTS and hence give new insight into structural changes of the hydrophobic gap. The presence of ions at hydrophobic interfaces is of great interest, since such systems play a crucial role in several processes in industry [95, 96, 97].

The reference system (without ions) is structured as follows: Silicon was used as substrate material, followed by a silicon oxide layer, a layer for the head group of OTS, an OTS tail group layer and a layer for the hydrophobic gap. Finally, a layer of water was modeled on top. An example for an XRR measurement and an EDP of this system is shown in figure 3.19. Here, the x-axis starts at the beginning of the OTS head group, since changes in the XRR data during the addition of ions did not affect the respective signal of the silicon and the silicon oxide of each wafer. Hence, the electron density, layer thickness, and roughness of the OTS head group, OTS tail group, and the hydrophobic gap were the free parameters to be optimized to describe changes in a series of measurement. The electron density of water (or aqueous solution) was calculated and not optimized during analysis.

Ions are added to the system by solving the compounds listed in subsection 3.2.2 in water. In the case of e.g. lithium chloride, the salt solves in water, leading to a separation of both ions Li^+ and Cl^-. These ions approach to the solid-liquid interface between the OTS tail group and the aqueous solution. Three adsorption pathways are possible on how the ions adsorb at the solid-liquid interface (see also figure 3.20).

In the first case, the OTS layer is completely continuous. Due to the dense packing of OTS molecules, the OTS tail group is perpendicular to the silicon surface. Hence, ions
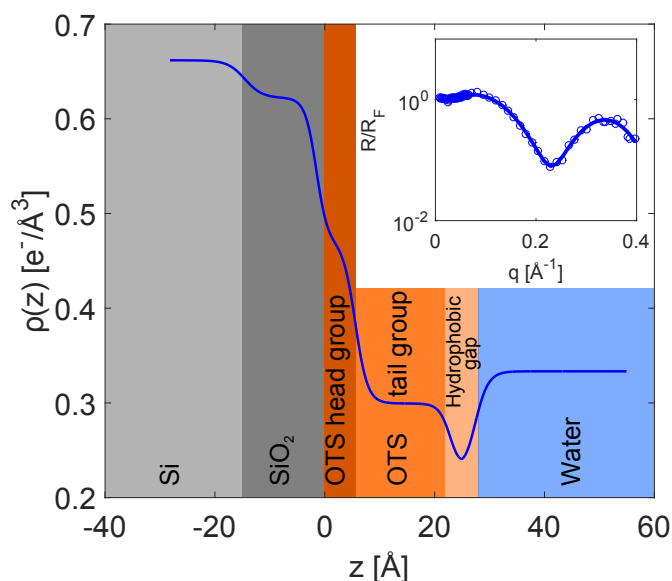
Figure 3.19: Example sample system of OTS coated silicon wafers: Silicon is the substrate material, followed by silicon oxide, the OTS head and tail groups and a hydrophobic gap between the OTS tail group and water.
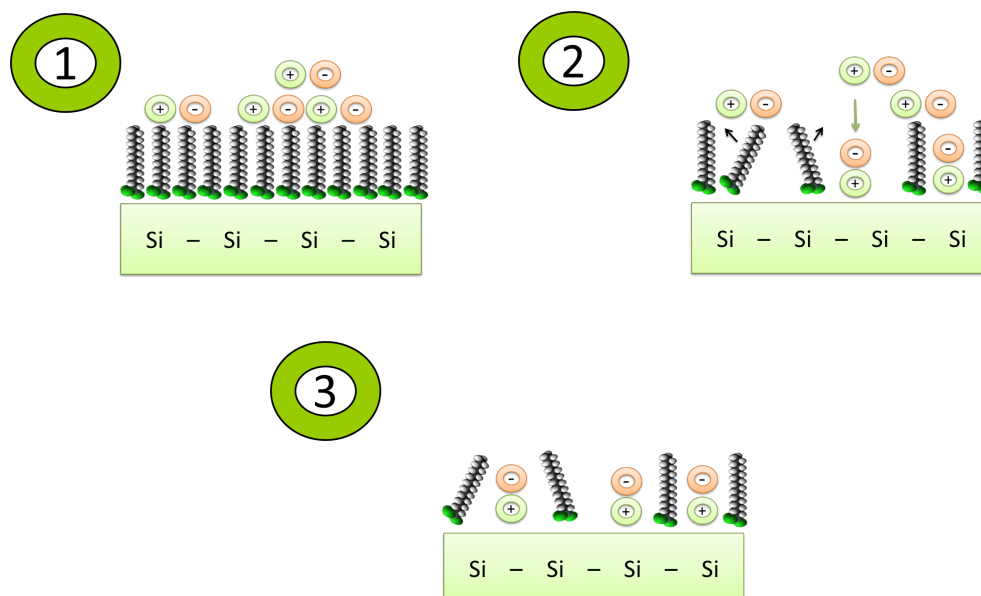

Figure 3.20: Three possible adsorption pathways for the adsorption of ions on OTS: 1. The OTS layer is completely closed and the ions adsorb on top of the tail groups of the OTS. 2: The OTS layer is not completely closed, so that ions may pass through the OTS layer and adsorb both on the OTS tail group as well as on the silicon surface below the OTS. 3: The OTS layer is not completely closed and has enough gaps that ions only adsorb on the silicon surface.

can only adsorb on top of the OTS tail groups without affecting the shape of the OTS head and tail groups in the EDP. Thus, both electron density and layer thickness of the OTS head and tail groups should not change and differences between measurements with different ion concentrations on the same surface should only be reflected by changes in the hydrophobic gap and the adsorbed amount of ions.

The second case describes a not entirely continuous OTS layer, so that ions fit between the OTS molecules and thus may both adsorb on top of the OTS tail group as well as on the silicon oxide layer of the wafer. Since there is space between the OTS molecules, it is possible that they are tilted and do not point exactly perpendicular from the surface. This will cause a decrease of the layer thickness of the OTS tail group in the EDP. However, with ion adsorption on top of the silicon oxide layer of the wafer, the space between OTS molecules is reduced, which will straighten the OTS molecules. After straightening all OTS molecules, no more increase in OTS tail group layer thickness is expected, which means that with rising ion concentration a saturation in the layer thickness of the OTS tail groups has to be reached. Moreover, the adsorbed ions between the OTS molecules should raise the electron density of the OTS head and tail groups.

In the third case, it is again assumed that the OTS layer is not completely continuous and thus there is enough space for the ions to adsorb on silicon oxide between the OTS molecules. However, the difference to the second case is that the gaps between the OTS molecules are so large that the adsorption of ions does not affect the OTS. In this case, no interaction between the ions and OTS occurs, which would result in a constant layer thickness of OTS head and tail groups. However, because of the adsorption of the ions between the OTS molecules, the electron density at least of the OTS head group should increase.

All of these assumptions do have a distinguishable fingerprint on the EDP and may thus be verified by XRR. Therefore, XRR is the method of choice to investigate the adsorption behavior of ions at hydrophobic interfaces. In the next subsection, the results of the adsorption behavior of lithium chloride solved in water on OTS will be presented as a function of lithium chloride concentration. Afterwards, the cation and the anion will be replaced by other cations and anions, respectively, to investigate the effect of ion size as well as the position of ions in the Hofmeister series (see section 2.1.1 for further details).

3.5.1 Lithium Chloride

In a first step, to identify effects caused by impurities of the purchased compounds, the adsorption behavior of a baked out (30 minutes at 400 °C) lithium chloride-water mixture and untreated lithium chloride-water mixture on OTS was investigated. The XRR data of lithium chloride solved in buffer on OTS is shown in figure 3.21. Main differences in the reflectivity occur in the region of the first local minimum around $0.2\,\text{Å}^{-1}$. With rising ion concentration, the minimum is more pronounced and shifts towards lower q_z-values. As shown in figure 3.22, this induces changes in the EDPs in the properties of the OTS tail group, the hydrophobic gap and in an appearance of an additional layer at the interface of the hydrophobic gap. In the case of baked out
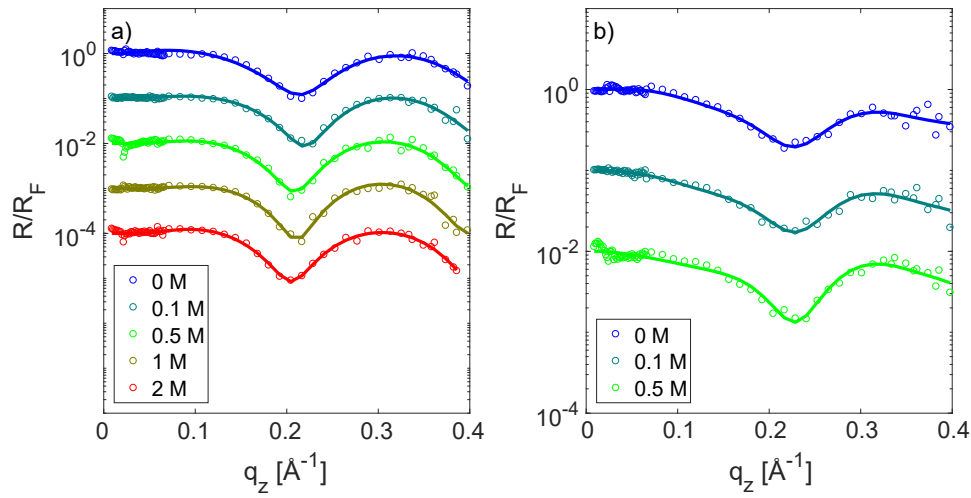
Figure 3.21: XRR data of in water solved lithium chloride adsorption on an OTS wafer as a function of concentration. In case a), the lithium chloride was baked out for 30 minutes at 400 °C before solved in water, while in b) the XRR data of untreated lithium chloride is shown. The circles represent the measured data, while the solid lines show the fit to the data. The data as well as the fits are shifted on the y-scale for better visualization.
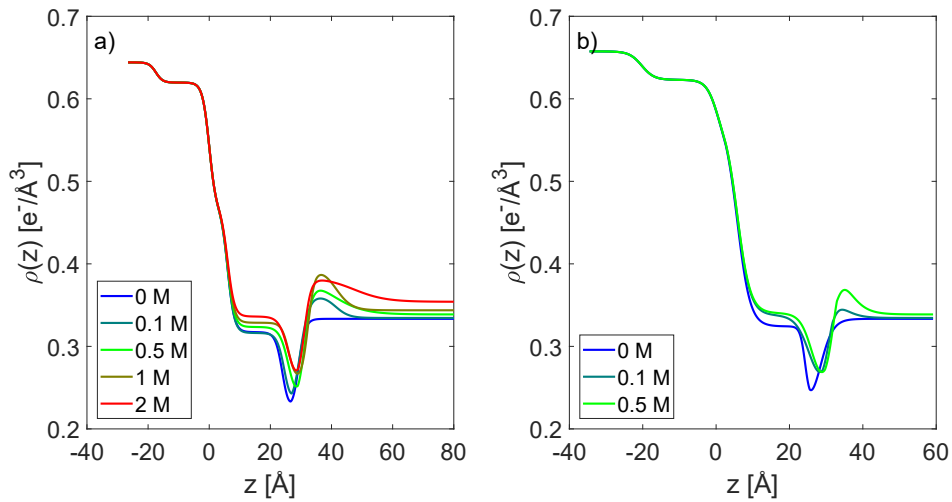

Figure 3.22: EDPs of in water solved baked out (a)) and untreated (b)) lithium chloride adsorption on an OTS wafer as a function of ion concentration.

compounds (see figure 3.22 a)), the electron density and layer thickness of the OTS tail group increase continuously with rising ion concentration. Moreover, the shape of

the hydrophobic gap changes as well as the adsorbed amount of ions at the interface of the hydrophobic gap with rising concentration. The hydrophobic gap becomes smaller with increasing concentration. Due to the high amount of solved ions in water, also the overall electron density of the LiCl solution increases. These results differ from the adsorption behavior of lithium chloride that was not treated before the measurements. In this case, already at a concentration of 0.1 M a strong increase in the electron density and layer thickness of the OTS tail group occurs, while the adsorbed amount of ions at the interface of the hydrophobic gap is quite small. Raising the concentration to 0.5 M does not lead to further significant changes in the hydrophobic gap region.

To investigate systematic changes in the EDPs with rising ion concentration as well as changes between different ions, the following parameters will be analyzed in detail in this chapter: the OTS tail group electron density ρ_{tg} and its increase with added ions $\Delta\rho_{tg}$ (as the difference between the OTS tail group electron density of a measurement with and without ions), the OTS tail group layer thickness d_{tg} and its increase with added ions Δd_{tg}, the integral over the hydrophobic gap I_{hg} and its increase with added ions ΔI_{hg} as well as the integral over the adsorbed ion layer I_{ion}. The meanings of these parameters are illustrated in figure 3.23 for clarification on the example of an XRR measurement of an OTS wafer in pure water and on an OTS wafer in a LiCl-water solution with the concentration of 2 M. In this figure, only the significant z-region of the EDPs is shown.

The integral value of the hydrophobic gap I_{hg} is calculated by the integral over electron density values lower than the electron density of the OTS tail group and bulk liquid for all positive z-positions. The value I_{ion} is calculated by the integral over electron density values higher than the electron density of the bulk liquid, starting at z-positions higher than the z-position of the minimum of the hydrophobic gap. As no changes in the OTS head group were observed, only the parameters presented in figure 3.23 are evaluated. Furthermore, because of the fact that error analysis in XRR measurements is difficult, errors for these parameters are determined by varying fit parameters of the OTS tail group and hydrophobic gap around the best fit and checking the fit consistency. Hence, depending on the data quality, following error ranges were estimated: The error of the electron density of the OTS tail group ρ_{tg} varies in the range between ± 0.002 and ± 0.005 electrons per cubic angstrom, errors of the OTS tail group layer thickness d_{tg} in the range between ± 0.2 and ± 0.5 angstrom and errors in the integral values of the hydrophobic gap and ion layer in the region between ± 0.01 and ± 0.03 electrons per square angstrom, respectively. The error values of the differences between two values are calculated according to Gaussian error propagation.

For further analysis, the parameters that were presented in figure 3.23 will be compared between the baked out and the untreated lithium chloride. A comparison of these parameters is shown in figure 3.24. In the case of the electron density of the OTS tail group (see figure 3.24 a)), solved baked out lithium chloride in water lead to a continuous increase of this parameter with rising concentration. Only for a 0.1 M concentration, a small decrease in electron density of the OTS tail group is observable. However, this deviation is within the uncertainty of the measurement. At the maximum LiCl concentration of 2 M, the increase of electron density in the OTS tail group is 0.02±0.002
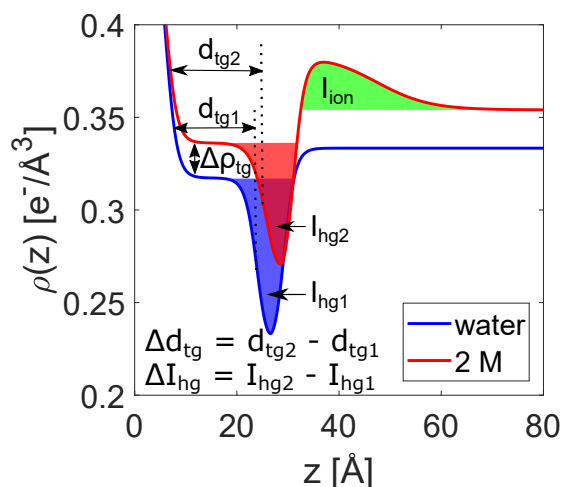
Figure 3.23: Illustration of the investigated parameters of the increase of OTS tail group electron density $\Delta\rho_{tg}$, increase of OTS tail group layer thickness Δd_{tg}, integral over the hydrophobic gap I_{hg} and integral over the adsorbed ion layer I_{ion} on the example of the EDP differences between a 2 M LiCl-water mixture and a pure water measurement.

electrons per cubic angstrom. Using the untreated compound also lead to a continuous increase of the electron density of the OTS tail group, but this increase is significantly stronger than for the baked out compound. Starting at a concentration of 0.1 M, the increase in electron density is as strong as at concentrations between 0.5 M and 1 M for the baked out compound, even though the electron density of the OTS tail group of the pure water measurement was already higher for the wafer that was used to investigate the adsorption effect of the untreated compound. Comparing the resulting values of electron density and length of the OTS tail groups of each salt concentration to those of pure water measurements show the changes in the OTS arrangement on the wafer as a function of salt concentration. Here, higher values of OTS tail group electron density and length represent a denser packed arrangement of OTS molecules on the silicon wafer. Hence, in the case of baked out lithium chloride, there were less ions adsorbing in-between the OTS tail groups. This is even more pronounced by looking at the differences in electron density of the OTS tail groups (see figure 3.24 b)).

A similar behavior can be observed for the length of the OTS tail group (see figure 3.24 c)). Adding the untreated compound leads already at a concentration of 0.1 M to an increase of the length of the OTS tail group of 2.19 ± 0.2 Å, which is comparable to the maximum possible increase for the baked out LiCl system (see figure 3.24 d) for differences in OTS tail group lengths as a function of concentration). Moreover, this study reveals that the increase of the OTS tail group in length is restricted to a value between 2 Å and 3 Å, depending on the value of the length of the OTS tail group for a pure water measurement (between 17.5 Å and 22 Å).

Another significant difference between the two systems is revealed by investigating the integrals of the hydrophobic gap and their differences between a pure water measure-
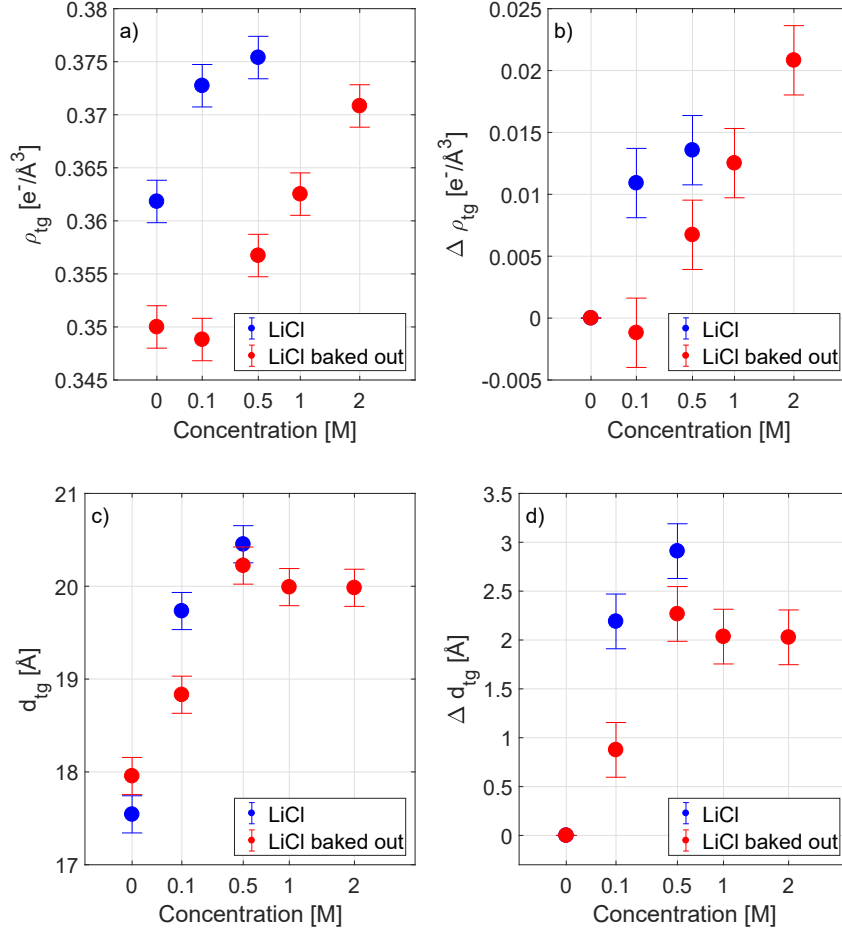
Figure 3.24: Comparison of the changes of the electron density (a)) and layer thickness (c)) of the OTS tail group as well as their differences (b) and d)) compared to a pure water measurement as a function of ion concentration between baked out and untreated lithium chloride. The x-axis is scaled to the square root of the concentration for better visualization.

ment and the system with added ions (see figure 3.25 a) and b)). Whereas in the case of the baked out compound the integral value of the hydrophobic gap decreases with rising concentration, this value increases for the untreated compound. In contrast, an ion layer adsorbs at the interface of the hydrophobic gap in both cases (see figure 3.25 c)). However, the baked out compound tends to adsorb significantly stronger on the hydrophobic surface, represented by much higher I_{ion} values compared to the untreated sample, even though no trend in the maximum concentration of the adsorbed ion layer is observable (see figure 3.25 d)).

All these results point out the difference in the behavior of the systems as a function of pre-experimental treatment. These differences indicate impurities in the used compounds that are reduced or even eliminated by baking out. Hence, to obtain correct
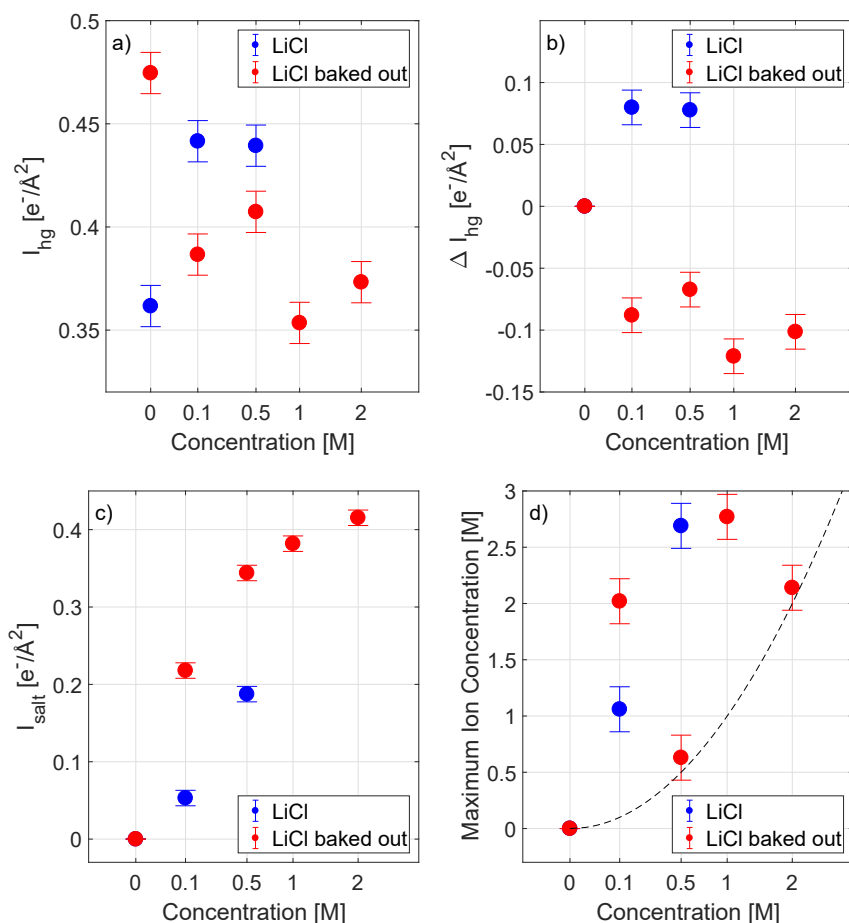
Figure 3.25: Comparison of the changes of the integral value of the hydrophobic gap (a)) and its difference compared to a pure water measurement (b)), the adsorbed ion layer (c)) and the maximum concentration of the adsorbed ion layer (d)) as a function of in water solved ion concentration between baked out and untreated lithium chloride. The x-axis is scaled to the square root of the concentration for better visualization. The dotted line in d) represents the case of no ion adsorption on OTS.

results of the adsorption behavior of ions on OTS, every sample was baked out before usage. Moreover, the adsorption behavior of lithium chloride hints the second pathway of ion adsorption on OTS (see figure 3.20) due to the increase of electron density and layer thickness of the tail group.

To confirm this adsorption pathway, the adsorption behavior of different ions on OTS was investigated and will be shown in the following subsections. First, several cations were examined with regard to their different sizes as well as position in the Hofmeister series.

3.5.2 Cation Variation

In a first step, lithium is replaced by other cations such as sodium, potassium, rubidium and caesium. Moreover, the adsorption behavior of ions resulting from a solution of hydrochloric acid in water is studied. The experiments and data analysis were performed analogously to the previous section. Figures 3.26 and 3.27 show the EDPs of ion-water mixtures on OTS as a function of ion concentration of hydrochloric acid, sodium chloride, potassium chloride, rubidium chloride and caesium chloride (the corresponding XRR data is shown in the appendix in figures B.1 - B.5).

Investigating the adsorption behavior of hydrochloric acid on OTS (see figure 3.26 a)) leads to a surprising result: In opposition to the adsorption behavior of lithium chloride (see figure 3.22 a)), for which adding lithium chloride led to changes in the electron density and length of the tail group, almost no changes are observable by adding hydrochloric acid in the OTS region. Even by increasing the hydrochloric acid concentration to 5 M, no changes in the OTS tail group are detected. Only the shape of the hydrophobic gap changes very slightly with a very small ion layer forming at the interface of the hydrophobic gap. This result coincides with pre-experimental expectations due to the fact that the hydrochloric acid is extremely soluble in water.

In opposition to this, replacing the hydrochloric acid with sodium chloride (see figure 3.26 b)) yields considerable changes. Here, even small amounts of ions lead to a strong increase in the OTS tail group length and a small increase in the OTS tail group electron density. Furthermore, a significantly larger layer of adsorbed ions forms at the interface of the hydrophobic gap compared to the measurement of hydrochloric acid at a concentration of 5 M. Raising the concentration of sodium chloride to 0.5 M and 1 M leads to a continuous, slight increase in OTS tail group electron density and length, while the amount of adsorbed ions at the interface of the hydrophobic gap increases strongly. Hence, with rising concentration, more ions are adsorbing in-between the OTS tail groups as well as at the hydrophobic interface. The maximal investigated NaCl concentration of 2 M reveals another strong increase in electron density of the OTS tail group, while the length of the OTS tail group decreases slightly. This implies that the maximum length of the OTS tail group is reached. The adsorbed amount of ions at the interface of the hydrophobic gap increases only slightly, too, which is a hint on a saturation of the adsorbed ion amount for solved sodium chloride. Measurements on higher NaCl concentrations were not possible. For all measured concentrations only small changes in the integral value and shape of the hydrophobic gap occurred.

Figure 3.26 c) shows the adsorption behavior of potassium chloride on OTS as a function of ion concentration. Like in the case of sodium chloride, electron density and layer thickness of the OTS tail group increases with rising concentration. Furthermore, an additional layer at the interface of the hydrophobic gap is formed. However, there are also differences in the EDPs: In the case of a 0.1 M KCl-water mixture, only the OTS tail group electron density increases, while the OTS tail group decreases slightly. Raising the concentration further to 0.5 M leads to a significant increase of the OTS tail group length, while the electron density of the OTS tail group increases only slightly. This is different to sodium chloride, where the maximal OTS tail group length was
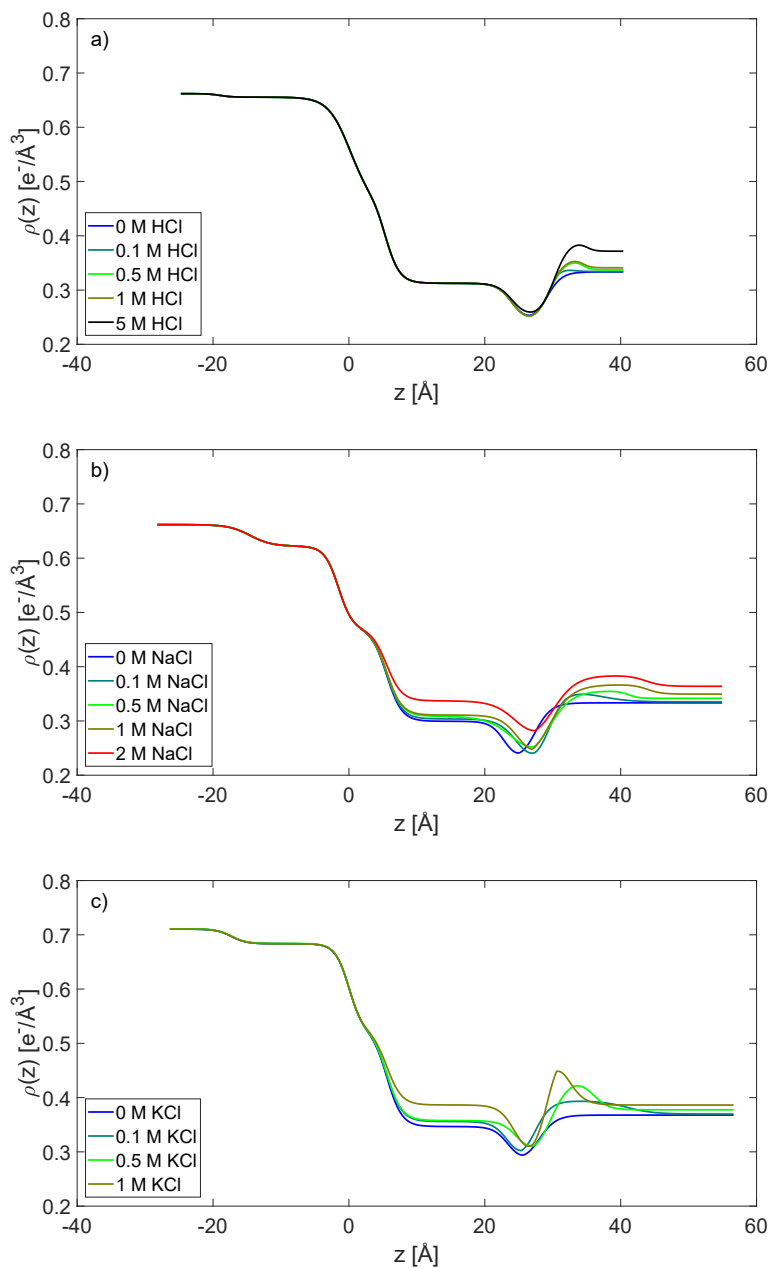
Figure 3.26: EDPs of HCl (a)), NaCl (b)) and KCl (c)) on OTS as a function of ion concentration. The corresponding XRR data is shown in the appendix in figures B.1, B.2 and B.3.

already reached at a concentration of $0.1\,\mathrm{M}$. Raising the potassium chloride concentration to $1\,\mathrm{M}$ leads to a further strong increase in the OTS tail group electron density, while the OTS tail group length decreases slightly. During all these measurements, the
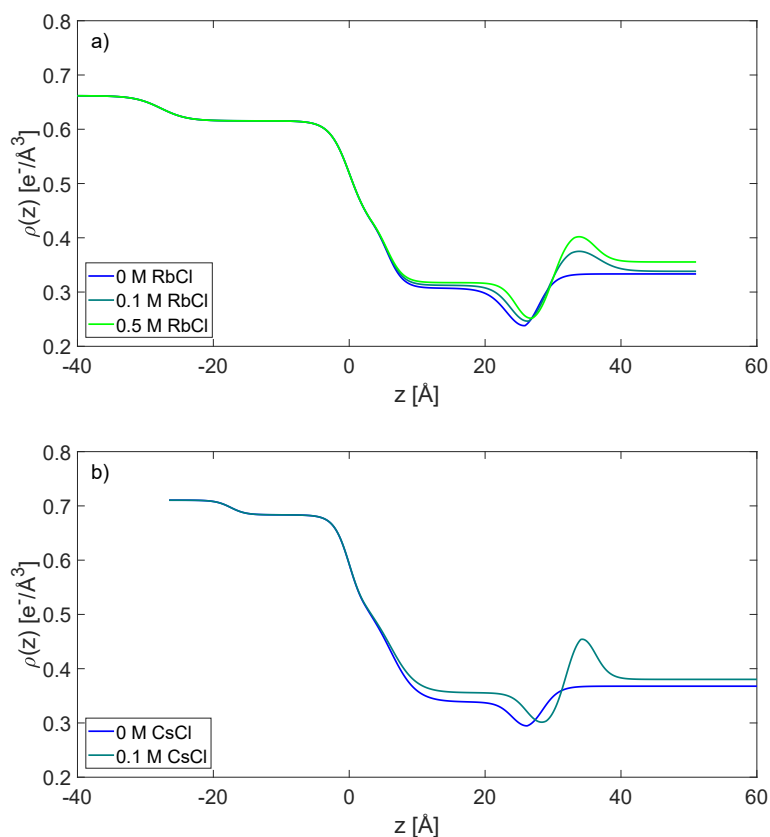
Figure 3.27: EDPs of RbCl (a)) and CsCl (b)) on OTS as a function of ion concentration. The corresponding XRR data is shown in the appendix in figures B.4 and B.5.

integral value of the hydrophobic gap as well as the amount of adsorbed ions stayed almost constant. However, their shape changed continuously with increasing concentration. The hydrophobic gap becomes sharper with increasing concentration, while the adsorbed ion layer is shifted to lower z-values. This means that the ions adsorb closer to the interface, which may affect the shape of the hydrophobic gap and thus lead to a decrease of the hydrophobic gap. However, the integral value of the hydrophobic gap does not increase due to the fact that the rising electron density of the hydrophobic gap is counteracted by rising electron density of the OTS tail group. Again, due to the high absorption of X-rays in the KCl-water mixture, it was not possible to investigate the adsorption behavior of ions for higher concentrations of KCl.

The adsorption behavior of rubidium chloride is shown in figure 3.27 a). Here, with rising concentration, OTS tail group electron density and length increase continuously. The behavior of the hydrophobic gap and the adsorbed ions is comparable to the observations on KCl-water mixtures: with rising concentration, the layer of adsorbed ions as well as the hydrophobic gap become sharper. Here, the integral value of the hydrophobic gap decreases continuously with rising concentration, while the amount

of adsorbed ions increases slightly. Unfortunately, due to the strong absorption, the highest concentration possible to investigate was 0.5 M.

Finally, the largest investigated cation was caesium. However, the maximally possible concentration to investigate was 0.1 M. Figure 3.27 b) shows the adsorption behavior of caesium chloride. Already at the concentration of 0.1 M, a strong increase in OTS tail group electron density as well as length is observed. Moreover, a distinct layer of adsorbed ions forms at the hydrophobic interface. However, this concentration is not high enough to produce changes in the shape of the hydrophobic gap, while its integral value rises slightly with ion addition.

As already presented in the case of lithium chloride in figure 3.24, changes of the OTS tail group electron density and length, the integral values of the hydrophobic gap and adsorbed ions as well as their difference values compared to pure water measurements are shown for all the compounds discussed in this section in figure 3.28 as a function of concentration.

Figures 3.28 a) and b) show changes in the OTS tail group electron density as a function of concentration. Hydrochloric acid is the only compound showing almost no changes in the OTS tail group electron density with rising concentration, while all other compounds cause an increase in the OTS tail group electron density with rising concentration. Figure 3.28 b) indicates that the increase in the OTS tail group electron density is correlated to the ion size. Larger ions induce a stronger increase in the OTS tail group electron density at a given concentration. Rubidium is the only ion not following this trend by increasing the OTS tail group electron density slightly less than expected at a concentration of 0.1 M. However, these results support the conclusion that for every concentration an almost equal amount of ions adsorb between the OTS tail groups. The different increase in electron density then results from the different amount of electrons and thus electron density of each cation. This suggests that the adsorbed amount of ions between the OTS tail groups is almost independent of the cation type, but may be controlled by the anion type. The influence of the anion variation will be investigated in the next subsection. Nevertheless, due to the lack of data at high concentration for large ions, these results need to be validated by further experiments.

The increase in the OTS tail group length as a function of concentration for different compounds is shown in figures 3.28 c) and d). All compounds (except hydrochloric acid) increase the OTS tail group length to a maximum value between 19 Å and 20.5 Å, which is equal to an increase of 1 Å to 2.5 Å. Smaller ions (lithium and sodium) generate a strong increase in OTS tail group length (2 Å to 2.5 Å), while larger ions (potassium and rubidium) generate only an increase of the OTS tail group length of 1 Å to 1.5 Å. Only caesium does not follow this trend by increasing the OTS tail group length to 2 Å at a concentration of 0.1 M. Due to the fact that the OTS tail group increase is linked to the orientation of the OTS molecules on the wafer (see figure 3.20 b)), a stronger increase in the OTS tail group is connected to more upright OTS molecules on the wafer perpendicular to the wafer surface. Neglecting the caesium measurement and considering the results of the OTS tail group electron density increase shows that lithium and sodium are able to produce a more upright orientation of the OTS molecules
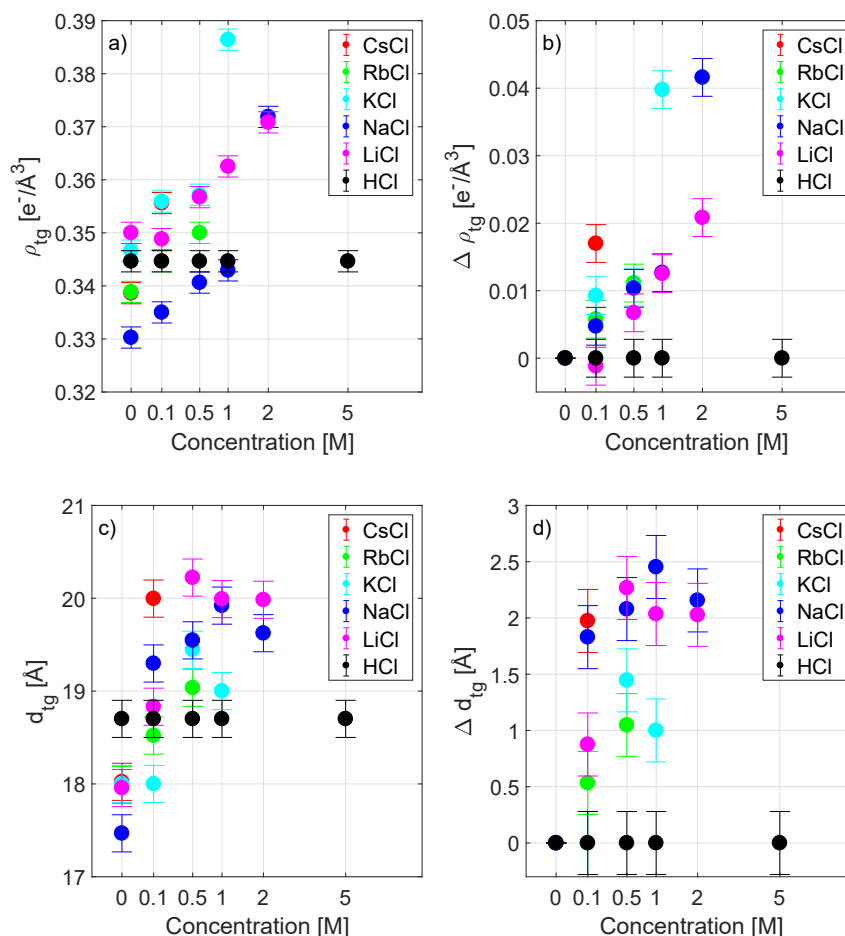
Figure 3.28: Comparison of the changes of the electron density (a)) and layer thickness (c)) of the OTS tail group as well as their differences (b) and d)) compared to a pure water measurement as a function of ion concentration for varied cations. The x-axis is scaled to the square root of the concentration for better visualization.

than potassium and rubidium. This may be indeed reasoned by the ion size, because small ions have more options to be placed around the OTS molecules. Since the cation is placed first, the ion size of the cation is relevant, even though the ion size of chloride is larger than of all cations.

Investigating the integral value of the hydrophobic gap (see figure 3.29 a)) as well as changes in this value (see figure 3.29 b)) upon concentration increase and the integral value of the adsorbed ion layer (see figure 3.29 c)), no systematic changes are observable. Moreover, the differences in the hydrophobic gap integral value vary in the range of ±0.15 electrons per square angstrom, while the integral value of the adsorbed ion layer seems not to correlate with ion size. However, the shapes of the hydrophobic gap and the ion layer change in the case of high concentrated potassium chloride, rubidium
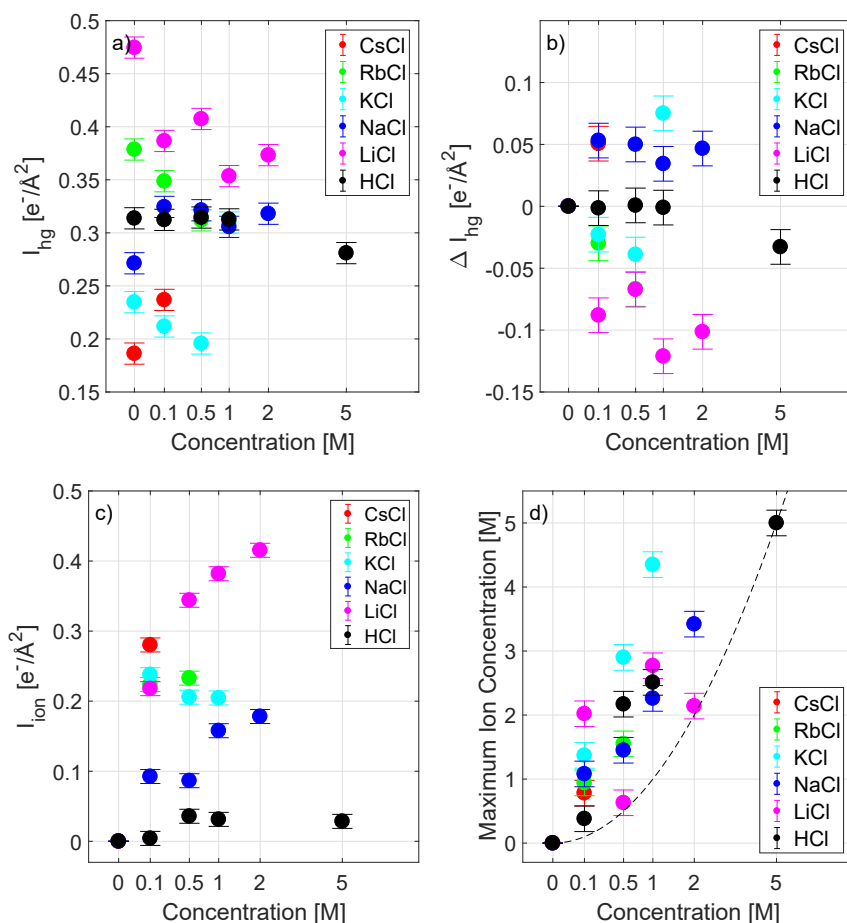
Figure 3.29: Comparison of the changes of the integral value of the hydrophobic gap (a)) and its difference compared to a pure water measurement (b)), the adsorbed ion layer (c)) and the maximum concentration of the adsorbed ion layer (d)) as a function of ion concentration for varied cations. The x-axis is scaled to the square root of the concentration for better visualization. The dotted line in d) represents the case of no ion adsorption on OTS.

chloride and caesium chloride, respectively. The larger the ion, the bigger changes are induced at equal concentrations. Here, the adsorbed ion layer shifts towards the OTS with rising concentration, leading to a sharpening of the hydrophobic gap. However, this does not affect the integral value of the hydrophobic gap. Furthermore, also the maximum ion concentration of the adsorbed ion layer (see figure 3.29 d)) is not correlated with cation size.

This study reveals that the adsorption behavior of ions at the hydrophobic interface of OTS varies for different cations. All the investigated ionic compounds have an impact on both the OTS tail group and the hydrophobic gap by adsorbing both in-between the OTS tail groups as well as at the interface of the hydrophobic gap, which is illustrated as pathway in figure 3.20 b). Investigating changes in the OTS tail group revealed that

for each concentration the overall amount of adsorbed ions is almost independent of the different cations, leading only to an increase of the OTS tail group electron density that correlates to the ion size. Moreover, small ions are able to cause a higher increase in OTS tail group length, while larger ions have a greater impact on shape changes of the hydrophobic gap and adsorbed ion layer. However, no ion type is able to induce significant changes in the integral value of the hydrophobic gap. Furthermore, the integral value as well as the maximum ion concentration of the adsorbed ion layer do not correlate with the size of the cations and show no significant changes through cation variation. To investigate the impact of the anion on the OTS structure and ion adsorption, the next subsection deals with measurements where the anion was varied. Here, sodium was chosen as the cation counterpart.

3.5.3   Anion Variation

To examine the influence of the anions on the adsorption behavior of ions at the hydrophobic interface between OTS and water, three different compounds were solved in water and investigated as a function of concentration: sodium chloride, sodium bromide and sodium iodide. Unfortunately, due to the high absorption of bromide and iodide ions, only concentrations of $0.1\,\mathrm{M}$ could be investigated. The EDPs of the investigated ionic compounds are shown as a function of concentration in figure 3.30 (the corresponding XRR data is shown in the appendix in figures B.6 and B.7).

Solved sodium bromide in water (see figure 3.30 b) leads to a significant increase in both the OTS tail group electron density and length. Furthermore, a small ion layer adsorbs at the interface of the hydrophobic gap. This ion layer induces slight changes in the shape of the hydrophobic gap. Even though the shape of the hydrophobic gap becomes sharper with sodium bromide addition, the integral value of the hydrophobic gap does not decrease, but instead increases slightly. This is the result of the same process that was discussed in the previous subsection: The integral value of the hydrophobic gap increases even though the shape of the hydrophobic gap becomes sharper due to the increase in OTS tail group electron density.

The last investigated compound upon anion variation is sodium iodide. Here, the addition of ions leads again to an increase in both the OTS tail group electron density and length. Compared to all investigated compounds before, it is the highest observed increase in OTS tail group electron density with 0.035 ± 0.002 electrons per cubic angstrom. This increase is twice as high as in the case of caesium chloride. The increase in OTS tail group length with less than $1\,\text{Å}$ is quite small. As already observed for all other compounds, also in the case of sodium iodide a small ion layer at the interface of the hydrophobic gap occurs at this concentration. This small layer causes significant changes in the shape of the hydrophobic gap, combined with an increase in the electron density of the OTS tail group. The shape of the hydrophobic gap is much sharper compared to the shape of the hydrophobic gap of the pure water measurement. Even though the shape of the hydrophobic gap becomes much sharper by adding sodium iodide, the integral value of the hydrophobic gap increases.
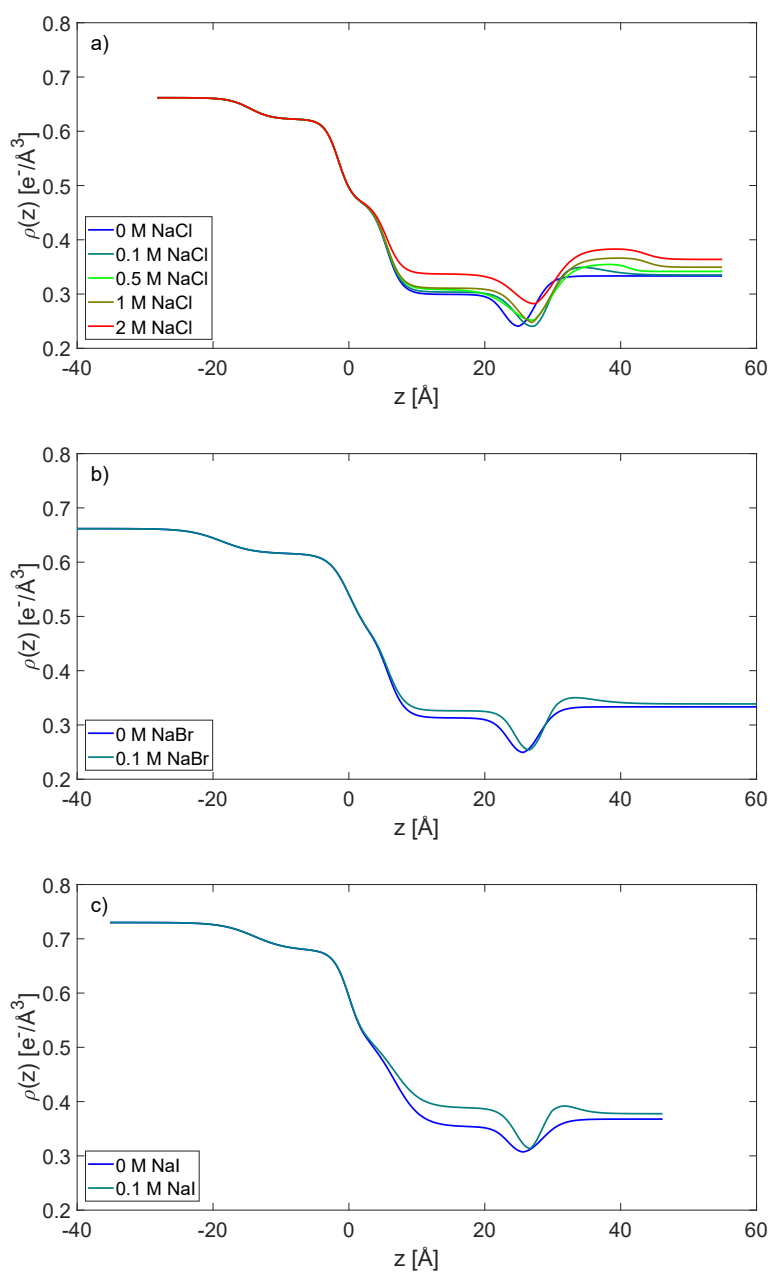
Figure 3.30: EDPs of NaCl (a), also shown in figure 3.26 b)), NaBr (b)) and NaI (c)) on OTS as a function of ion concentration. The corresponding XRR data is shown in the appendix in figures B.2, B.6 and B.7.

Quantitative changes of the OTS tail group electron density and length as well as the integral values of the hydrophobic gap and adsorbed ion layer as a function of ion con-

centration for different anions are shown in figures 3.31 and 3.32. In the case of the OTS tail group electron density (see figures 3.31 a) and b)), the addition of all compounds lead to an increase of this quality, which is correlated to the size of the ion. The larger the ion, the higher the increase in electron density of the OTS tail group. With 0.014 ± 0.002 electrons per cubic angstrom, the increase in OTS tail group electron density for a $0.1\,\text{M}$ concentrated sodium bromide-water mixture was higher than the increase of OTS tail group electron density of a $1\,\text{M}$ concentrated sodium chloride-water mixture. Replacing sodium bromide by sodium iodide lead to a more than twice as high increase in the electron density of the OTS tail group. This behavior is comparable to what was shown for the case of cation variation (see section 3.5.2). Also the behavior of the OTS tail group length (see figures 3.31 c) and d)) is comparable to the case of
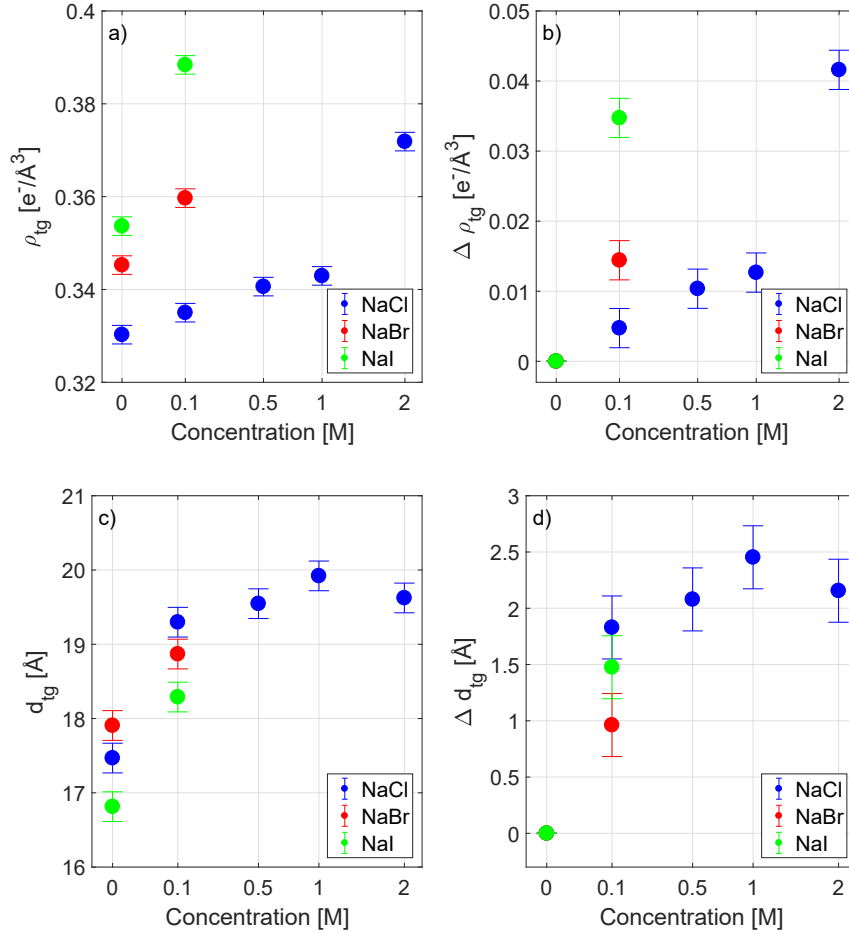
Figure 3.31: Comparison of the changes of the electron density (a)) and layer thickness (c)) of the OTS tail group as well as their differences (b) and d)) compared to a pure water measurement as a function of ion concentration for varied anions. The x-axis is scaled to the square root of the concentration for better visualization.
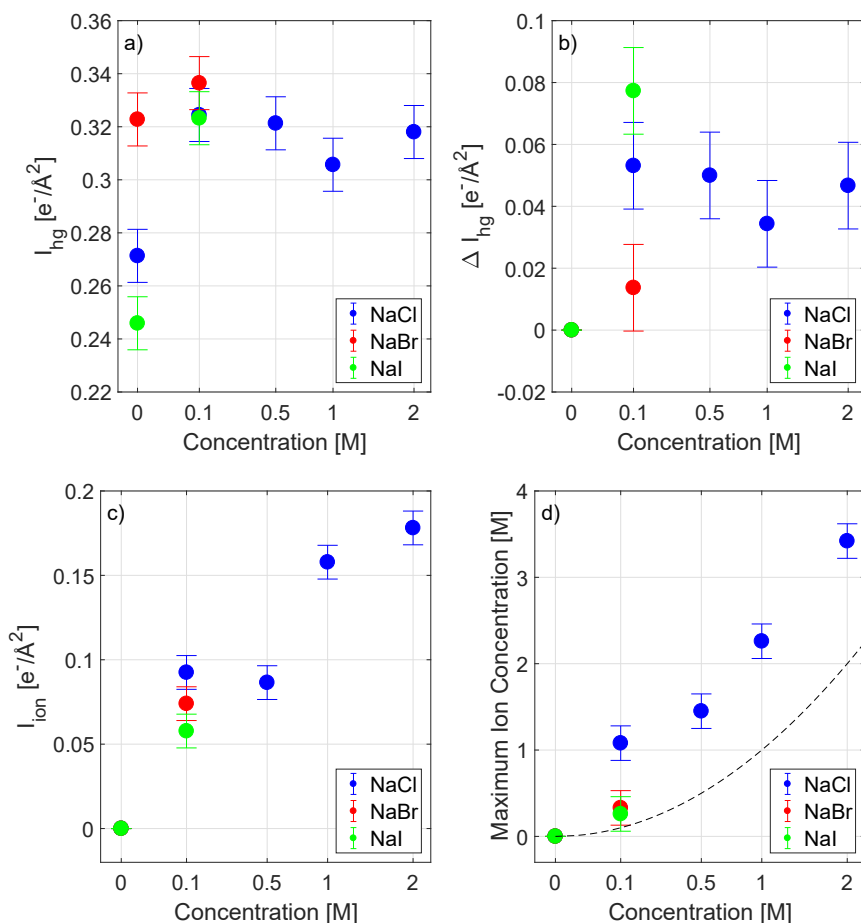
Figure 3.32: Comparison of the changes of the integral value of the hydrophobic gap (a)) and its difference compared to a pure water measurement (b)), the adsorbed ion layer (c)) and the maximum concentration of the adsorbed ion layer (d)) as a function of ion concentration for varied anions. The x-axis is scaled to the square root of the concentration for better visualization. The dotted line in d) represents the case of no ion adsorption on OTS.

cation variation (see section 3.5.2): increasing the ion size lead to a smaller increase in the OTS tail group length.

Moreover, changes in the integral value of the hydrophobic gap (see figure 3.32 a) and b)) and integral value of the adsorbed ion layer (see figure 3.32 c)) were investigated. As in the case of cation variation, a slight increase of the integral value of the hydrophobic gap is observable upon concentration increase of the ionic compounds, but being still in the region of ±0.15 electrons per square angstrom. However, the shape of the hydrophobic gap and the ion layer get sharper upon addition of a compound, which is comparable to large cations (e.g. adsorption of caesium chloride) in the previous subsection. Moreover, the maximum ion concentration of the adsorbed ion layer (see figure 3.32 d)) may be correlated to the anion size. The maximum ion concentration of the

adsorbed ion layer is decreasing for larger anions. Nevertheless, this has to be approved by further measurements.

Hence, all the conclusions drawn concerning the adsorption behavior of ions at the hydrophobic interface of OTS, which were derived from cation variation, are confirmed by anion variation. However, investigating the cation variation for another anion may provide new insight into the adsorption behavior of ions on OTS. Therefore, alkali metal hydroxides were chosen as sample material. Their adsorption behavior on OTS will be discussed in the following subsection.

3.5.4 Hydroxides

To get a greater knowledge of the adsorption behavior of ions on OTS and the consequences of the presence of ions for the OTS system, the adsorption of solved alkali metal hydroxides was investigated. The results are comparable to the results of section 3.5.2, while differences can only be reasoned by the change of anion type.

Before analyzing the results, it is necessary to mention that by adding hydroxide compounds on top of the OTS wafers, a bubble formation occurred (see figure 3.33), being stronger with increased concentration and increased cation size. After removing the ionic compound after the measurements, the OTS surface was dull. Hence, this chemical reaction may have attacked the OTS surface. However, during analysis no changes in the parameters of the substrate as well as the silicon oxide or OTS head group were observable. Therefore, the analysis was undertaken in the same way as the analysis of chlorine compounds.
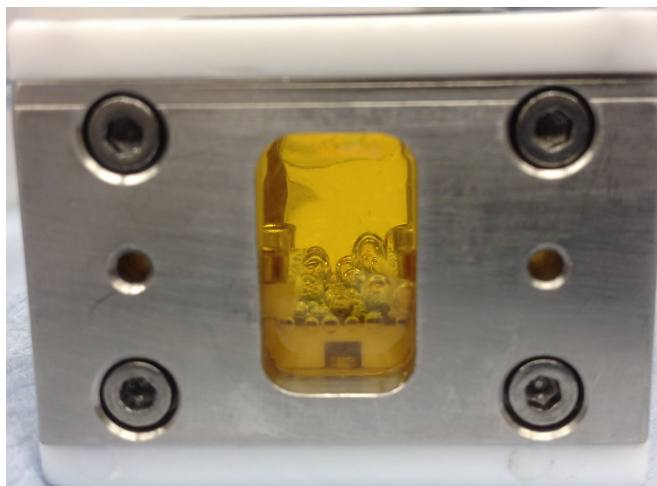
Figure 3.33: Bubble formation during measurement of a 0.5 M CsOH-water mixture on an OTS wafer.

Figures 3.34 and 3.35 show the EDPs of the concentration-dependent adsorption behavior of LiOH, NaOH, KOH, RbOH and CsOH on OTS (the corresponding XRR data
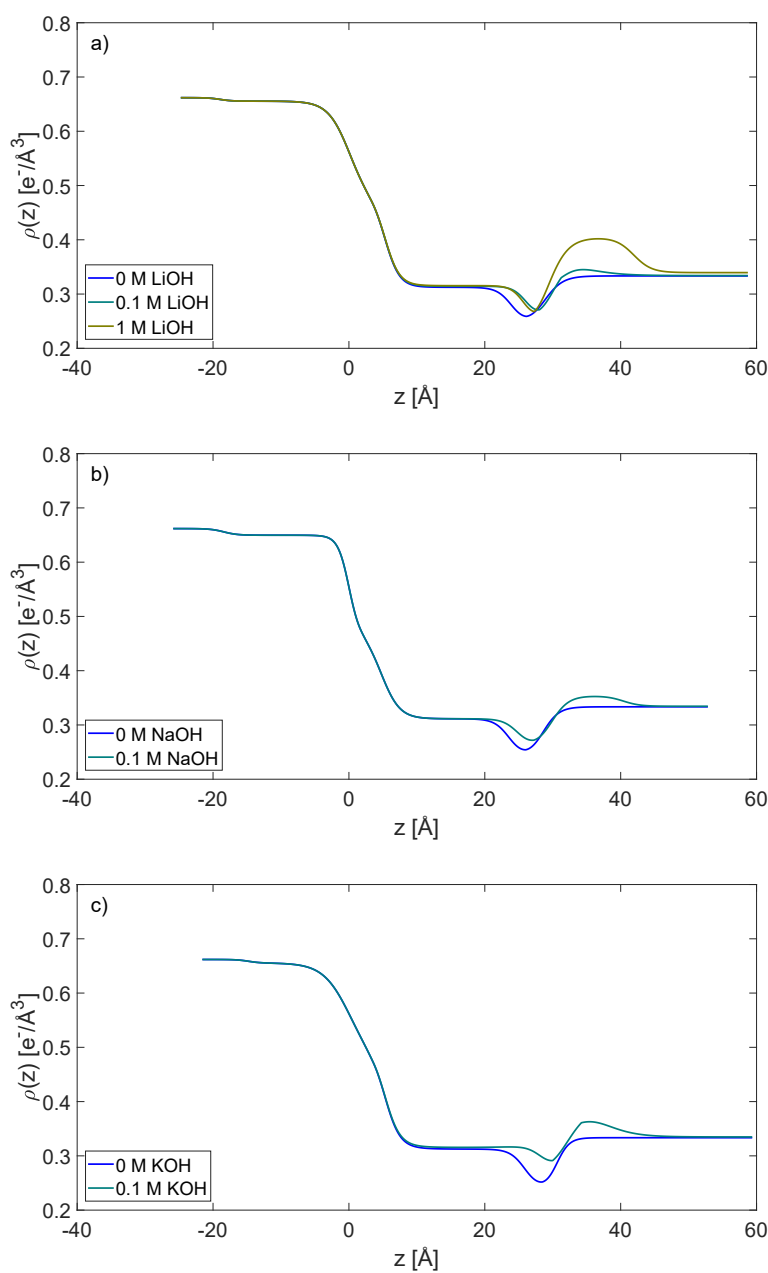
Figure 3.34: EDPs of LiOH (a)), NaOH (b)) and KOH (c)) on OTS as a function of ion concentration. The corresponding XRR data is shown in the appendix in figures B.8, B.9 and B.10.

is shown in the appendix in figures B.8 - B.12). In the case of lithium hydroxide (see figure 3.34 a)), already a small amount of ions added (concentration: 0.1 M) leads to a strong increase in the length of the OTS tail group, while the electron density of the
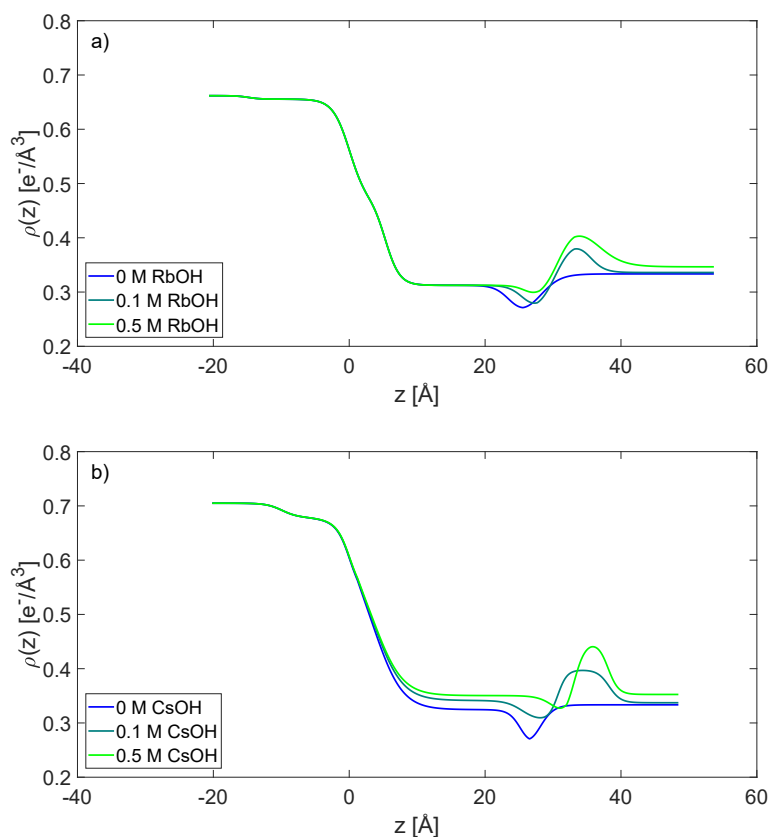
Figure 3.35: EDPs of RbOH (a)) and CsOH (b)) on OTS as a function of ion concentration. The corresponding XRR data is shown in the appendix in figures B.11 and B.12.

OTS tail group stays almost constant. Furthermore, a small amount of ions adsorbs at the interface of the hydrophobic gap, leading to a sharpening of it. Moreover, in opposite to ion adsorption with halogens as anion, a significant decrease in the integral value of the hydrophobic gap occurs. This is the result of the combination of an increase in electron density of the hydrophobic gap together with an almost constant electron density of the OTS tail group with an additionally sharper shape of the hydrophobic gap. Increasing the concentration to $1\,M$, almost no changes in the OTS tail group occur anymore. However, changes in the hydrophobic gap and the adsorbed ion layer are more pronounced in this case. The amount of adsorbed ions at the interface of the hydrophobic gap increases drastically, leading to a further sharpening of the shape of the hydrophobic gap. Hence, there is also a further decrease of the integral value of the hydrophobic gap.

The concentration-dependent adsorption behavior of sodium hydroxide is comparable to lithium hydroxide. Unfortunately, only $0.1\,M$ sodium hydroxide solution could be investigated. Here, adding ions leads to an increase in the length of the OTS tail group, while the electron density of the OTS tail group shows almost no change. There is

also a small ion layer adsorbing at the interface of the hydrophobic gap, resulting in a sharpening of the shape of the hydrophobic gap and a decrease of the integral value of the hydrophobic gap.

The adsorption behavior of potassium hydroxide on OTS differs significantly from those of lithium hydroxide and sodium hydroxide. Even though at a concentration of $0.1\,M$ there is an increase in the OTS tail group length going in hand with only a slight increase in electron density, the size of the hydrophobic gap decreases drastically. Here, the electron density of the hydrophobic gap increases to a value that is only slightly below the electron density of the OTS tail group, while the adsorption of the ion layer at the interface of the hydrophobic gap results in a sharpening of the shape of the hydrophobic gap. Hence, the integral value of the hydrophobic gap decreases much more than the integral value of the hydrophobic gap of LiOH-water and NaOH-water mixtures. Unfortunately, measurements of higher concentrated mixtures were also impossible for potassium hydroxide. Here, an investigation of the behavior of the hydrophobic gap at higher ion concentrations would have been very interesting with regard to a complete vanishing of the hydrophobic gap.

Increasing the cation size further to rubidium results in a reduction of the effects that were seen in the case of potassium hydroxide. Even though the length of the OTS tail group increases by an almost constant electron density, this increase is smaller compared to potassium hydroxide. Moreover, the electron density of the hydrophobic gap does not increase as strong as in the case of potassium hydroxide, even though in the case of rubidium hydroxide a higher amount of ions adsorbs at the interface of the hydrophobic gap. Hence, the integral value of the hydrophobic gap in the case of $0.1\,M$ concentrated rubidium hydroxide is higher compared to $0.1\,M$ concentrated potassium hydroxide. Nevertheless, raising the concentration of rubidium hydroxide to $0.5\,M$ results in a significant reduction of the integral value of the hydrophobic gap. This is caused by a strong increase of the electron density of the hydrophobic gap. Moreover, there is a strong increase of the adsorbed amount of ions upon constant electron density and length of the OTS tail group. Here, the hydrophobic gap is almost completely closed.

The last investigated compound is caesium hydroxide. Here, a $0.1\,M$ mixture induces an increase in the electron density of the OTS tail group going in hand with an increase of the length of the OTS tail group. This is the only compound of the series of hydroxides that induced a significant change in the electron density of the OTS tail group. Furthermore, a high amount of ions is adsorbing at the interface of the hydrophobic gap. Due to an increase in the hydrophobic gap electron density, the integral value of the hydrophobic gap decreases too. However, this is the smallest decrease of the integral value of the hydrophobic gap for all compounds containing hydroxide at a concentration of $0.1\,M$. With a further increase in concentration to $0.5\,M$ caesium hydroxide, the electron density of the OTS tail group increases too. There is also an increase in the OTS tail group length to $(26.7 \pm 0.2)\,\text{Å}$. This value is higher than possible for an OTS tail group. Therefore, something must adsorb directly on the OTS tail group, overcoming the hydrophobic gap. Interestingly, there is still a $2\,\text{Å}$ long area with a reduced electron density located below the adsorbed ion layer. This area has an

electron density that is comparable to the electron density of pure water. Here, further investigations are necessary to reveal the character of this area of lower electron density.

To compare the influence of the ion size as a function of concentration on the OTS tail group and the hydrophobic gap, the in figure 3.23 illustrated parameters were investigated for hydroxides and shown in figures 3.36 and 3.37. Furthermore, the parameters investigated in the case of sodium chloride that were shown previously in figures 3.28, 3.29, 3.31 and 3.32, are presented for comparison.

The concentration-dependent behavior of the electron density of the OTS tail group is presented in figure 3.36 a) and its differences compared to a pure water measurement
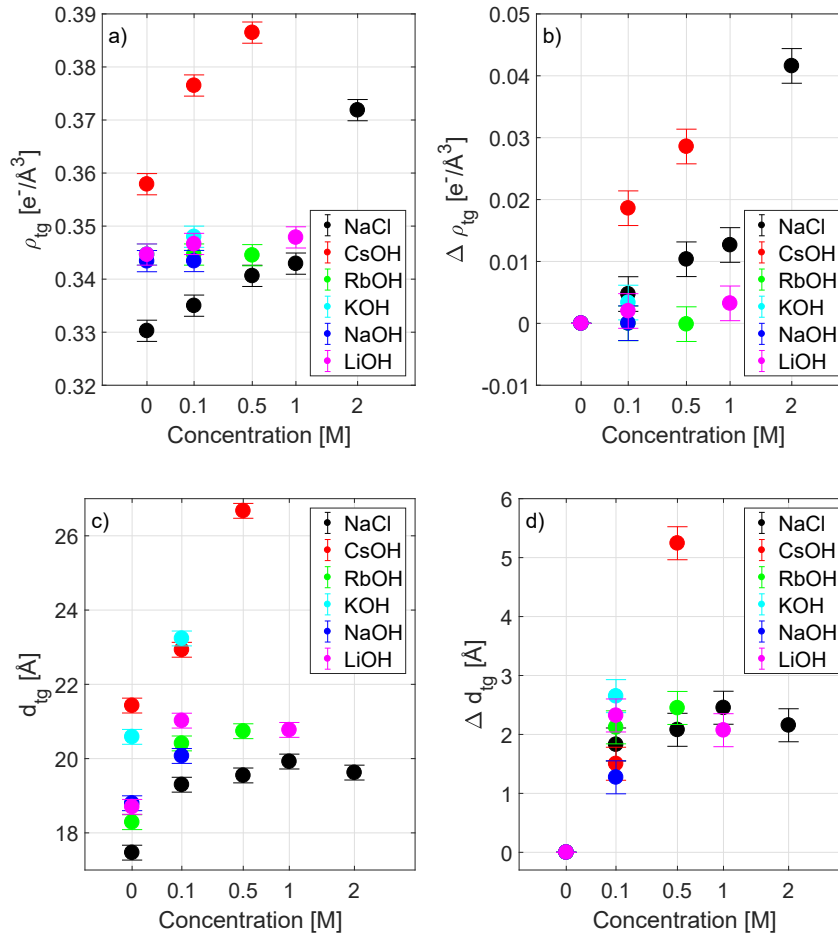
Figure 3.36: Comparison of the changes of the electron density (a)) and layer thickness (c)) of the OTS tail group as well as their differences (b) and d)) compared to a pure water measurement as a function of ion concentration for varied cations with hydroxide as anion. Additionally, the data of sodium chloride, which was shown in figures 3.28 and 3.31, is plotted for comparison. The x-axis is scaled to the square root of the concentration for better visualization.
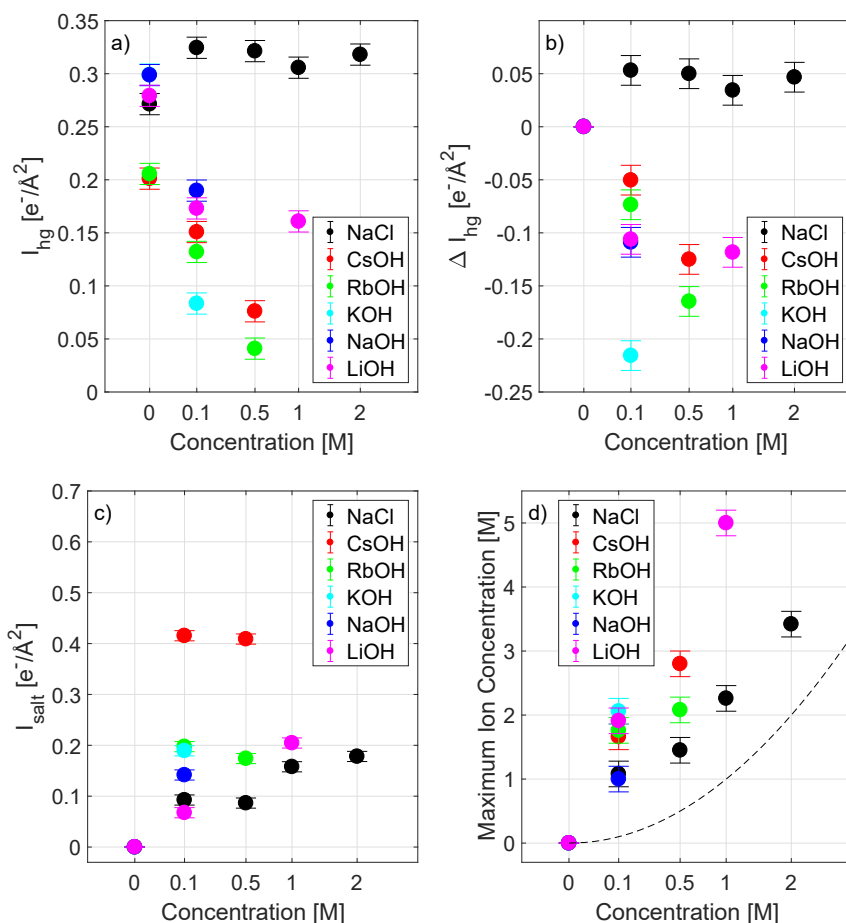
Figure 3.37: Comparison of the changes of the integral value of the hydrophobic gap (a)) and its difference compared to a pure water measurement (b)), the adsorbed ion layer (c)) and the maximum concentration of the adsorbed ion layer (d)) as a function of ion concentration for varied cations with hydroxide as anion. Additionally, the data of sodium chloride, which was shown in figures 3.29 and 3.32, is plotted for comparison. The x-axis is scaled to the square root of the concentration for better visualization. The dotted line in d) represents the case of no ion adsorption on OTS.

in figure 3.36 b). Here, it is observable that the increase in electron density by adding compounds containing hydroxide (except caesium hydroxide) are smaller compared to the increase of sodium chloride, for each concentration respectively. Moreover, there is no correlation between ion size and increase in electron density of the OTS tail group in the case of LiOH, NaOH, KOH and RbOH. The only compound causing a significant increase in the OTS tail group electron density is caesium hydroxide. Here, the electron density increases as a function of concentration with an increase of 0.019 ± 0.002 electrons per cubic angstrom at a concentration of $0.1\,\mathrm{M}$ and the maximum increase of 0.029 ± 0.002 electrons per cubic angstrom at the concentration of $0.5\,\mathrm{M}$. The value at

0.1 M is comparable to the OTS tail group electron density increase of 0.1 M caesium chloride, which was unfortunately not measured at 0.5 M. Hence, in presence of caesium, the anion seems to be unimportant for the increase of the electron density of the OTS tail group. However, for smaller cations, the anions play a crucial role. In the case of chloride, the increase of the electron density of the OTS tail group was correlated to the cation size, while in the case of hydroxides for all cations (except caesium) almost no increase in the electron density of the OTS tail group occurs. Due to the fact that the cation adsorbs first in-between the OTS tail groups, this means that in the case of hydroxides only a very small amount of ions adsorb in-between the OTS tail group, whereas in the case of chloride, an almost constant amount of ions adsorbed in-between the OTS tail groups, leading to the correlation of the increase in OTS tail groups to the ion size.

The length of the OTS tail group is also increased by addition of ionic compounds (see figures 3.36 c) and d)). However, in the case of hydroxides, no correlation between ion size and increase in the length of the OTS tail group occurs. This result is equal to the chlorine compounds, where also no correlation between ion size and increase in the length of the OTS tail group was observable. However, since the increase in the OTS tail group length is finite, a saturation in the increase of the OTS tail group length occurs with increasing ion concentration of both compound types. Nevertheless, by using 0.5 M caesium hydroxide, an even higher increase in the OTS tail group length is achievable. This is possible by a complete closure of the hydrophobic gap. Accordingly, ions may then adsorb directly on top of the OTS tail group, resulting in an artificial raise of the OTS tail group length.

Regarding the integral value of the hydrophobic gap (see figure 3.37 a) and b)), replacing the chloride anion by hydroxide provided new insights into the adsorption behavior of ions on OTS. Due to the fact that the electron density of the hydrophobic gap increases significantly with the addition of an ionic compound containing hydroxide, while the electron density of the OTS tail group stays almost constant, a significant decrease in the integral value of the hydrophobic gap is observable. Moreover, this decrease of the integral value is correlated to the cation size. Small cations (lithium, sodium and potassium) lead to a higher decrease in the integral value of the hydrophobic gap compared to larger cations like rubidium and caesium (see figure 3.37 b)). However, in the case of lithium and sodium, the integral value of the hydrophobic gap was quite high at the pure water measurement. Hence, a better overview on the changes in the integral value is given by the absolute values (see figure 3.37 a)). Here, it is clear that potassium, rubidium and caesium addition are able to reduce the integral value of the hydrophobic gap below 0.1 electrons per square angstrom. This means that the hydrophobic gap almost vanishes upon addition of these compounds, which is in opposite to the chlorine compounds, for which almost no changes in the integral value of the hydrophobic gap occurred upon addition of ionic compounds. Therefore, these results imply that the anion type has a strong impact on the hydrophobic gap. However, also the impact of the cation is not negligible. A special case is the case of caesium hydroxide at a concentration of 0.5 M, where the hydrophobic gap seems to be overcome due to the high detected OTS tail group length. This result suggests the possibility of a complete

closure of the hydrophobic gap.

Finally, the integral value of the adsorbed ions as well as the maximum ion concentration of the ion layer at the interface of the hydrophobic gap was investigated (see figure 3.37 c) and d)). Here, a strong correlation between the ion size and the adsorbed amount of ions is observable with regards to the integral value of the adsorbed ion layer. Nevertheless, the maximum ion concentration is independent of the cation. However, the integral value at a concentration of 0.1 M is below 0.2 electrons per square angstrom for all cations (except of caesium), which is smaller than the integral value of all chlorine compounds at the same concentration except of sodium chloride. Hence, also in the case of the integral value of the adsorbed ions, both the cation and the anion play an important role. Nevertheless, the fact that the ion layer is at the interface of the hydrophobic gap, which is almost completely closed in some cases, has an impact on these results.

3.6   Conclusions

Within this chapter, two different studies on the investigation of the adsorption behavior at solid-liquid interfaces were presented. These studies were performed by means of XRR, revealing high resolution EDPs with the possibility to track even very small changes *in-situ* on the investigated interface.

The first study dealt with the adsorption behavior of lysozyme on titanium oxide surfaces as a function of temperature, pressure, pH value and titanium oxide layer thickness. In accordance with a former study using silicon oxide surfaces, a slight adsorption of lysozyme on titanium oxide with rising temperature in the temperature region between 20 °C and 60 °C was observed. Raising the temperature to the region of the temperature of denaturation (71 °C) resulted in a strong increase of the adsorbed lysozyme amount. However, even beyond the denaturation temperature, the adsorbed amount of lysozyme is still smaller than on silicon oxide. Due to the fact that adsorption process is partially driven by electrostatic interactions, surface charge dependent measurements were performed by changing the pH value of the system. Below a pH value of 5 almost no lysozyme adsorption on titanium oxide was observable, because of the positive charge of both the titanium oxide and lysozyme at these conditions. Increasing the pH value further resulted in a stronger lysozyme adsorption with the maximum adsorbed amount of lysozyme at a pH value of 9.8. Nevertheless, even at this pH value the adsorbed amount of lysozyme on titanium oxide is smaller than on silicon oxide. A further increase of the pH value leads to a reduction of the adsorbed lysozyme amount due to the IEP of lysozyme being around a pH value of 11. Above this pH value, again both the titanium oxide surface and the lysozyme are equally charged, resulting in a decrease of the adsorbed amount of lysozyme. Due to different adsorbed amount of lysozyme on titanium oxide and silicon oxide surfaces at equal surface charge (compare results of titanium oxide measurements at pH 7 and silicon oxide measurements

at pH 9.8), these results indicate that not only surface charge differences, but also structural differences have to be taken into account. Therefore, titanium oxide layer thickness dependent measurements were performed, resulting in a higher amount of adsorbed lysozyme with rising layer thickness of titanium oxide. Additionally, the Hamaker constant for the sample geometry was calculated, leading to the conclusion that the silicon substrate appears to be repulsive, resulting in a reduced adsorption of lysozyme at thin titanium oxide layers. Finally, pressure-dependent measurements were performed, which showed a desorption behavior of lysozyme with rising pressure, being almost completely reversible by releasing pressure. These results indicate that lysozyme under hydrostatic pressure prefers to be completely hydrated in solution instead of having a defective hydration shell near the substrate. Thus, desorption of lysozyme at the interface is preferred leading to a smaller adsorbed amount of lysozyme at the titanium oxide surface. The presented results point out that the adsorption process of lysozyme depends strongly on the properties of the interface it adsorbs on.

After investigating protein adsorption at the hydrophilic surface of titanium oxide, a second study with regards to the adsorption behavior of ions at the hydrophobic surface of a with OTS coated silicon wafer was performed. Here, the aim was to investigate ion adsorption at the hydrophobic surface as a function of concentration and ion size. Simultaneously, changes in OTS, caused by addition of ionic compounds, were investigated. First, three different possible pathways for ion adsorption were formulated and the correct pathway of ion adsorption on OTS was determined. Moreover, the necessity to bake out the ionic compounds before usage (here: 30 minutes at 400 °C) was shown by comparing results of baked out and untreated lithium chloride adsorption behavior on OTS.

Due to the fact that upon addition of ionic compounds the electron density as well as the length of the OTS tail group changed, while all parameters of the OTS head group stayed constant, it was revealed that the OTS molecules did not form a completely closed layer and were not oriented completely perpendicular to the surface plane. Adding ions lead to a reorientation of the OTS tail groups, which resulted in an increase of the OTS tail group length in the EDP. Moreover, the ion adsorption occurred in-between the OTS tail groups, which resulted in an increased OTS tail group electron density in the EDP going in hand with no changes in the OTS head group parameters. This pathway is the second pathway that was shown in figure 3.20.

Ion size dependent studies were first performed by varying the cation. At the beginning, the adsorption behavior of hydrochloric acid was investigated. Almost no changes in the concentration-dependent EDPs were observable. Thereafter, the adsorption of in water solved alkali metals other than lithium was investigated. Raising the concentration of these compounds leads to an increase in both the electron density and layer thickness of the OTS tail groups going in hand with an increased amount of ions at the interface of the hydrophobic gap. However, the behavior of the integral value of the hydrophobic gap did neither correlate to concentration of ions nor to ion size. Concerning the electron density of the OTS tail group, the electron density increased with rising ion size. Due to the fact that the electron density of each ion increases with rising ion size by

itself, this result may be interpreted by an almost constant amount of adsorbed ions, independent of ion size. This result is also confirmed by the investigation of the maximum ion concentration in the adsorbed ion layer. Here, no correlation between ion size and the maximum ion concentration in the adsorbed ion layer is observable. The OTS tail group length increase was also dependent on the ion size. Small cations (lithium and sodium) caused a stronger increase in the OTS tail group length at low concentrations, which means that small cations are able to induce a more upright orientation of the OTS molecules than potassium and rubidium, since these cations have more available space to adsorb on. Here, the size of the cation is relevant due to the fact that the cation adsorbs first in-between the OTS tail groups, followed by the anion. However, due to the fact that an increase in the OTS tail group length is caused by reorientation of the OTS tail group, it is obvious that there is a limit in the increase of the OTS tail group length. The maximum increase of OTS tail group length was reached for large cations at higher concentrations compared to small cations.

Even though the integral value of the hydrophobic gap was not correlated neither to the concentration of ions nor to ion size, the shape of the hydrophobic gap changed upon concentration raise of large cations. Starting with potassium, the shape of the hydrophobic gap became sharper going hand in hand with a small increase in the electron density of the hydrophobic gap at high concentrations. However, due to the increase in the electron density of the OTS head group, almost no changes in the integral value of the hydrophobic gap occurred. Furthermore, also the integral value of the adsorbed amount of ions showed no correlation with ion size. However, like in the case of the hydrophobic gap, the shape of the adsorbed ion layer changed upon concentration raise of large cations. The shape of the ion layer became sharper, while the adsorption shifted towards the hydrophobic gap, which may also have an impact on the shape change of the hydrophobic gap for these cations. Furthermore, for all cations the adsorbed amount of ions increased with rising concentration.

In a next step, the anion was varied by keeping sodium as the cation. Here, raising the concentration lead also to an increase in both the OTS tail group electron density and length. These results are comparable to the cation variation, being also ion size dependent in the same way. However, in the case of OTS tail group electron density, by raising the anion size a stronger increase occurred compared to changes of the cation size. Furthermore, results in the increase of the OTS tail group length are comparable to the chlorine compounds with large cations. Also the changes in the integral values and shapes of the hydrophobic gap and adsorbed ion layer are comparable to the results of large cations, even though the overall adsorbed amount of ions for sodium bromide and sodium iodide is smaller than those of the chlorine compounds.

Finally, alkali hydroxides were solved in water and the adsorption behavior of these ions on OTS was investigated. Surprisingly, only in the case of caesium hydroxide the electron density of the OTS tail group increased significantly. All other compounds caused an electron density increase of the OTS tail group that was smaller than the one that was caused by sodium chloride. Hence, in the presence of hydroxide, only a small amount of ions adsorb in-between the OTS tail groups. Nevertheless, this is enough to reorientate the OTS tail group, resulting in an increase of the OTS tail group length

that is comparable to chlorine compounds. The strongest differences between hydroxide and chlorine as anion occurred in the hydrophobic gap. The presence of hydroxide leads to a significant decrease of the hydrophobic gap. Together with the almost constant electron density of the OTS tail group, this results in a significant decrease of the integral value of the hydrophobic gap, being below 0.1 electrons per square angstrom in the case of high concentrated potassium hydroxide, rubidium hydroxide and caesium hydroxide. In the case of a 0.5 M concentrated caesium hydroxide solution, the hydrophobic gap seems even to be completely closed due to the fact that the OTS tail group length increases beyond reasonable values. This may only be explained by ions adsorbing directly on top of the OTS tail group, overcoming the hydrophobic gap. Concerning the adsorption of ions, there are also differences compared to chlorine compounds: With the exception of caesium hydroxide, in the case of all other compounds the adsorbed amount of ions is smaller than in the case of chloride compounds. However, the results gained by the compounds containing hydroxides have to be interpreted with caution due to the fact that a chemical reaction occurred by adding these mixtures on top of the OTS, resulting in a bubble formation inside the sample cell.

Chapter 4

Electron Density Disturbance Evolution in Water on Attosecond Time Scales

The main subject of this chapter is the structure of pure water. Much effort has been made to investigate the structure of water during last centuries [223, 224, 225, 226, 36, 12]. However, there are still many unsolved questions regarding the physical and chemical properties of water and the anomalies of water that are assumed to be caused by its structure [227, 228, 26, 229, 230]. In recent years, with the construction of new, powerful synchrotron radiation sources and free electron lasers, structural investigations have proceeded to even smaller time and length scales. With the use of high energy X-rays, spatial resolution in the sub-Angstrom region is possible, while time scales shift towards femtoseconds and sub-femtoseconds [231, 232, 233]. Therefore, to study these ultrafast dynamics, usually pump-probe experiments are used, where a first laser or X-ray pulse initiates a process and a second one inspects the system after a desired time delay [111, 112, 113]. By varying the delay time, dynamics of processes on very short time scales can be investigated. However, the necessity of ultrashort pulses, a high repetition rate of the laser as well as the necessity to change the sample on short time scales limit those experiments.

In the year 2004, Abbamonte et al. presented a method to image the space and time evolution of electron density disturbances in water with non-resonant Inelastic X-ray Scattering (IXS) [114]. IXS reveals information on the dynamic structure factor of a system, which contains the electronic information of the system as a function of energy and momentum transfer of the X-rays. Here, ultrafast dynamics can be studied by investigating the sample structure up to a high energy transfer region, while a high momentum transfer provides spatial resolution in the Angstrom regime. For example, by investigating a momentum transfer region of up to $5\,\text{Å}^{-1}$ and an energy transfer region of up to $100\,\text{eV}$, dynamics with a spatial resolution of $1.27\,\text{Å}$ and a time resolution of $41.3\,\text{as}$ were investigated [114]. However, the scattering cross section of this technique is very small, resulting in long exposure times of the sample. Therefore, the

experimental conditions have to be kept constant during a long time (over one day for the experiments performed in the framework of this thesis), which limits sample systems that may be investigated by this technique. Moreover, highly absorbing sample cells cause problems due to the fact that especially in the case of high momentum and energy transfers the signal is weak.

In the framework of this thesis, electron density disturbances in space and time in water were investigated at 4 °C, 20 °C and 90 °C at ambient pressure by IXS. Momentum and energy transfers were studied up to $24.48\,\text{Å}^{-1}$ and $3000\,\text{eV}$, resulting in a time resolution of 2.1 as and a spatial resolution of $0.26\,\text{Å}$.

This chapter is structured as follows: First, the theoretical background of IXS will be presented regarding the extraction of time and space resolved information on the dynamic structure factor. Afterwards, the experimental setup and experimental procedure will be introduced, followed by a discussion of the data analysis. Here, special attention will be payed to the steps necessary to obtain the dynamic structure factor from the experimental data and to calculate the electron density propagator. Thereafter, imaging the density disturbances is possible by performing two Fourier transforms on the density propagator. Here, an analysis on the dependency of investigated momentum and energy transfer ranges on the density disturbances evolution is performed in detail for all three measured temperatures. The obtained results will then be summarized in the last section of this chapter.

4.1 Inelastic X-ray Scattering Theory

The theory of non-resonant Inelastic X-ray Scattering methods is subject of several textbooks like [117, 234]. Hence, this section gives only a short overview on the IXS technique with focus on the extraction of the dynamic structure factor and the electron density propagator. A complete theoretical description on inelastic X-ray scattering methods is given by Schülke [117].

The non-resonant Inelastic X-ray Scattering technique probes the interaction of an incoming photon and a sample with transferred momentum and energy. A scheme of the scattering geometry is shown in figure 4.1. Here, the incoming photon with wave vector $\mathbf{k}_1$, energy $\hbar\omega_1$ and polarization $\boldsymbol{\epsilon}_1$ is scattered at the sample at an angle of 2Θ into a photon with the wave vector $\mathbf{k}_2$, energy $\hbar\omega_2$ and polarization $\boldsymbol{\epsilon}_2$. The wave vector $\mathbf{k}_1$ is linked to the incident photon energy λ_1 via $|\mathbf{k}_1| = \frac{2\pi}{\lambda_1}$. The transferred energy is then

$$\hbar\omega = \hbar\omega_1 - \hbar\omega_2 \tag{4.1}$$

while the momentum transfer is equal to

$$\hbar\mathbf{k} = \hbar\mathbf{k}_1 - \hbar\mathbf{k}_2. \tag{4.2}$$

Hence, the absolute value of the momentum transfer is given by

$$\hbar k = \hbar\sqrt{\mathbf{k}_1^2 + \mathbf{k}_2^2 - 2\,|\mathbf{k}_1|\,|\mathbf{k}_2|\cos\left(2\Theta\right)} = \hbar\sqrt{\left(\frac{\omega_1}{c}\right)^2 + \left(\frac{\omega_2}{c}\right)^2 - 2\frac{\omega_1}{c}\frac{\omega_2}{c}\cos\left(2\Theta\right)}. \tag{4.3}$$
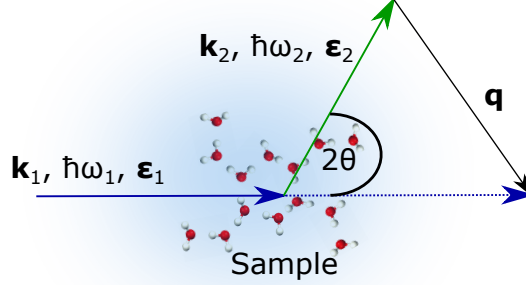
Figure 4.1: Scheme of the scattering geometry in an IXS experiment based on Schülke [117]. The incident photon with wave vector $\mathbf{k}_1$, energy $\hbar\omega_1$ and polarization $\boldsymbol{\epsilon}_1$ is scattered at the sample at the angle 2Θ. The scattered photon has a wave vector $\mathbf{k}_2$, energy $\hbar\omega_2$ and polarization $\boldsymbol{\epsilon}_2$.

In an experiment, the parameters $\mathbf{k}_1$, ω_1, $\boldsymbol{\epsilon}_1$, $\mathbf{k}_2$, ω_2 and $\boldsymbol{\epsilon}_2$ can be controlled, resulting in a free choice of energy and momentum transfer. The measured experimental quantity is proportional to the double differential scattering cross section (DDSCS) $\frac{\mathrm{d}^2\sigma}{\mathrm{d}\Omega\mathrm{d}\hbar\omega}$, which is defined as the current of the scattered photons with energy in the range $[\hbar\omega, \hbar\omega + \mathrm{d}\hbar\omega]$ into the solid angle element $[\Omega, \Omega + \mathrm{d}\Omega]$ normalized to the current of incident photons relating to the solid angle element $\mathrm{d}\Omega$ and the energy element $\mathrm{d}\hbar\omega$.

To describe the interaction between photons and matter from the theoretical point of view, the static Schrödinger equation must be solved. The DDSCS is derived by application of Fermi's golden rule to the Hamilton operator H_{int} in lowest order perturbation theory, which describes the interaction between an electromagnetic field and the sample's electrons in the non-relativistic case neglecting magnetic interactions via

$$H_{\text{int}} = \sum_j \frac{e^2}{2m_{\text{e}}c^2}\hat{\mathbf{A}}_j^2 + \sum_j \frac{e}{m_{\text{e}}c}\hat{\mathbf{p}}_j \cdot \hat{\mathbf{A}}_j. \tag{4.4}$$

Here, e is the eletron's charge and m_{e} its mass, while $\hat{\mathbf{A}}_j$ is the vector potential of the electromagnetic field and $\hat{\mathbf{p}}_j$ the momentum of the jth electron [235]. A fundamental difference between both terms of the Hamiltonian has to be taken into account: The first part of the Hamiltonian is proportional to the square of the vector potential of the electromagnetic field and hence describes a two-photon process, where the incident photon is annihilated and a new, scattered photon is created. This is a non-resonant inelastic scattering process for $\omega_1 \neq \omega_2$ and an elastic scattering process for $\omega_1 = \omega_2$. The second part of the Hamiltonian is proportional to the vector potential of the electromagnetic field and thus describes an absorption process, where the incident photon

is annihilated. This term only contributes in second order perturbation theory and therefore describes resonant inelastic scattering for incident energies in the region of the binding energy of a bound electron. Therefore, this term will be neglected in the following. Hence, the non-resonant part of the DDSCS can be derived by Fermi's golden rule in the Born approximation [236, 117] to

$$
\frac{\mathrm{d}^2\sigma}{\mathrm{d}\Omega\mathrm{d}\omega_2} = \left(\frac{\mathrm{d}\sigma}{\mathrm{d}\Omega}\right)_{\mathrm{Th}} S(\mathbf{k},\omega)
\tag{4.5}
$$

with Thomson's scattering cross section

$$
\left(\frac{\mathrm{d}\sigma}{\mathrm{d}\Omega}\right)_{\mathrm{Th}} = r_{\mathrm{e}}^2 \left(\boldsymbol{\epsilon}_1 \cdot \boldsymbol{\epsilon}_2{}^*\right)^2
\tag{4.6}
$$

describing the photon-electron coupling and the dynamic structure factor

$$
S(\mathbf{k},\omega) = \left(\frac{\omega_2}{\omega_1}\right) \sum_{\mathrm{i,f}} \left| \left\langle \mathrm{f} \left| \sum_j e^{\imath \mathbf{k} \cdot \mathbf{r}_\mathrm{j}} \right| \mathrm{i} \right\rangle \right|^2 \delta\left(E_i - E_f + \hbar\omega\right),
\tag{4.7}
$$

containing all information of the electronic system that can be extracted from the non-resonant Inelastic X-ray Scattering (NRIXS) spectrum. Here, r_e is the classical electron radius, $\mathbf{r}_\mathrm{j}$ the position operator of the jth electron and $|\mathrm{i}\rangle$ and $|\mathrm{f}\rangle$ the initial and final state, respectively. Hence, the dynamic structure factor describes the probability of all excitations from the initial states $|\mathrm{i}\rangle$ into final states $|\mathrm{f}\rangle$ with energies E_i and E_f, respectively, with ensured energy conservation via $\delta\left(E_i - E_f + \hbar\omega\right)$.

With the free choice of electron and momentum transfer, different excitations can be probed in an IXS experiment:

Phonon excitations In the case of $kr_\mathrm{d} \approx 1$ and $\omega \approx \omega_{\mathrm{ph}}$ phonon excitations occur, where r_d is the interionic distance and ω_{ph} is the phonon frequency.

Valence electron excitations With $kr_\mathrm{c} \approx 1$ and $\omega \approx \omega_{\mathrm{p}}$ valence electron excitations occur. Here, r_c is the interparticle distance and ω_{p} is the plasmon frequency. Hence, collective plasmon excitations and particle-hole excitations can be investigated.

Inner-shell excitations, X-ray Raman Scattering (XRS) Inner-shell excitations are probed in the case of $ka < 1$ (dipole excitations) or $ka \approx 1$ (non-dipole excitations) and $\hbar\omega \approx E_{\mathrm{B}}$ with the orbital radius a and the binding energy of an electronic level E_{B}.

Compton scattering For large momentum $qr_\mathrm{c} \gg 1$ and energy transfers $\hbar\omega \gg E_0$, the impulse approximation is satisfied and Compton scattering occurs. Here, E_0 denotes the characteristic energy of the system (e.g. the binding energy of core electrons or the Fermi energy for valence electrons).
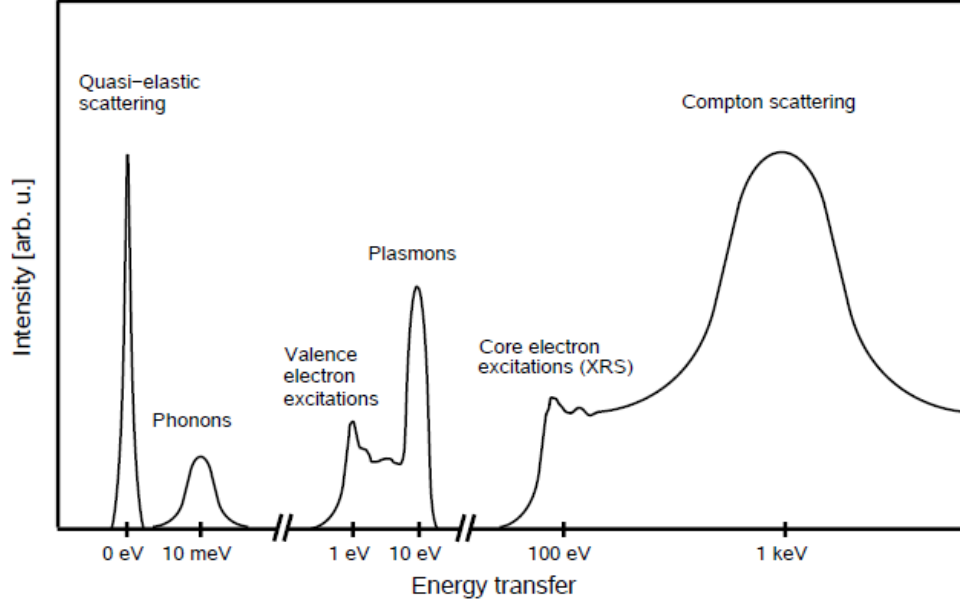
Figure 4.2: Schematic overview of possible excitations that can be stimulated in an IXS experiment, as shown by Lehmkühler [239]. The energy transfer axis represents only the dimension of the energy loss at which the different excitations occur. The effective values vary for each sample system, respectively.

The different excitations are presented in figure 4.2. Here, the energy transfer axis only represents the dimension of the energy loss at which the different excitations occur, while effective values vary for each system, respectively. For example, electron binding energies are element specific and are thus located at specific energy transfer position, depending on the element. A list with electron binding energies can be found in literature [237, 238]. In contrast, the location of the Compton scattering maximum on the energy transfer axis depends on the momentum transfer.

Due to the fact that the dynamic structure factor contains all information of the electronic system, it is possible to probe spatial and temporal phenomena of the electron density on attosecond time scales and sub-angstrom length scales by IXS experiments. However, simply performing a Fourier transformation would yield a correlation function with no causal properties, hence containing no useful information on the investigated system. However, there is a method to derive a retarded electron density propagator $\chi(\mathbf{x},t)$ from an IXS experiment [114, 118], which will be further discussed in this section. Therefore, the dynamic structure factor is first transformed to

$$S(\mathbf{k},\omega) = \sum_{i,f} |\langle f|\hat{n}(\mathbf{k})|i\rangle|^2 P_n \delta(E_i - E_f + \hbar\omega) \tag{4.8}$$

with the Boltzmann factor $P_n = exp[-E_n/k_B T]$ and $\hat{n}(\mathbf{k})$ as the Fourier transform of $\hat{n}(\mathbf{x},0)$, the operator of the total electron density at position $\mathbf{x}$ and zero time point $t = 0$. The dynamic structure factor is then related to the propagator of the electron

density via the quantum mechanical version of the Fluctuation-dissipation theorem by

$$S\left(\mathbf{k},\omega\right) = \frac{1}{\pi} \frac{1}{exp[-\hbar\omega/k_B T] - 1} Im\left[\chi\left(\mathbf{k},\omega\right)\right]. \tag{4.9}$$

Hence, an IXS experiment only provides information on the imaginary part of the propagator χ and the so-called "inverse scattering problem" for IXS has to be solved. This is the reason, why a simple double Fourier transformation of the dynamic structure factor does not contain useful information on the investigated system.

The solution of the inverse scattering problem goes in hand with the understanding of what information was lost in the experiment. Due to the fact that a propagator's function is to describe the system's evolution in time, it needs to depict the causalities of this system. However, different conventions for causality may be chosen. For example, a retarded propagator $\chi_R\left(\mathbf{x},t\right)$ describes dynamics only for times $t > 0$, leading to an entropy increase, while in the case of an advanced propagator $\chi_A\left(\mathbf{x},t\right)$ dynamics only for times $t < 0$ take place, resulting in an entropy decrease. However, the common part of all these conventions is that if these propagators are transformed into reciprocal space, they all have the same imaginary part and only differ in their real part. Hence, only the causality itself is lost in an IXS experiment, since IXS experiments provide only microscopic information and thus do not contain information about the entropy of the system. Therefore, there is a method consisting of four steps to reconstruct causality with the data from the experiment and thus to solve the inverse scattering problem. The first step is to extract the quantity $Im\left[\chi\left(\mathbf{k},\omega\right)\right]$ by symmetrizing the data via

$$Im\left[\chi\left(\mathbf{k},\omega\right)\right] = \pi\left[S\left(\mathbf{k},\omega\right) - S\left(\mathbf{k},-\omega\right)\right]. \tag{4.10}$$

In a second step, the data must be analytically continued on the energy transfer scale to preserve causality in the final result. Now, it is possible to obtain $\chi\left(\mathbf{k},t\right)$ in the third step, either by performing a sine transformation of the imaginary part $Im\left[\chi\left(\mathbf{k},\omega\right)\right]$ via [118]

$$\chi\left(\mathbf{k},t\right) = 2\int d\omega\, Im\left[\chi\left(\mathbf{k},\omega\right)\right]\sin\left(\omega t\right) \tag{4.11}$$

or by retrieving the real part of $\chi\left(\mathbf{k},\omega\right)$ over the fact that it satisfies the second Kramers-Kronig relation [240]

$$Re\left[\chi\left(\mathbf{k},\omega\right)\right] = \frac{2}{\pi}P\int_0^\infty d\omega' \frac{Im\left[\chi\left(\mathbf{k},\omega'\right)\right]}{\omega' - \omega} \tag{4.12}$$

and further perform a Fourier transform on the reconstructed $\chi\left(\mathbf{k},\omega\right)$ from the real and imaginary part by

$$\chi\left(\mathbf{k},t\right) = \frac{1}{\pi}\int_0^\infty d\omega\,\left[\sin\left(\omega t\right)Im\left[\chi\left(\mathbf{k},\omega\right)\right] + \cos\left(\omega t\right)Re\left[\chi\left(\mathbf{k},\omega\right)\right]\right]. \tag{4.13}$$

In equation 4.12, P denotes the principal part of the integral. Finally, in the fourth step, $\chi\left(\mathbf{x},t\right)$ may be obtained by a spatial Fourier transformation of $\chi\left(\mathbf{k},t\right)$. Due to

this procedure, retarded causality is imposed and $\chi\left(\mathbf{x},\mathrm{t}\right)$ is a retarded propagator that is nonzero only for times $t > 0$, resulting in increasing entropy. The propagator

$$\chi\left(\mathbf{x},\mathrm{t}\right) = -\frac{\imath}{\hbar}\left\langle[\hat{n}\left(\mathbf{x},\mathrm{t}\right),\hat{n}\left(0,0\right)]\right\rangle\Theta(t) \tag{4.14}$$

describes the probability of the evolution of a disturbance in the electron density from the origin $\hat{n}\left(0,0\right)$ at time $t = 0$ to $\hat{n}\left(\mathbf{x},\mathrm{t}\right)$ at position $\mathbf{x}$ and time $t > 0$. Here, $\Theta(t)$ is a step function to ensure the correct evolution of the time axis.

After the theoretical background was set on how to investigate disturbances in the electron density on extreme small time and space scales by an IXS experiment, an experimental setup and the experimental procedure will be introduced in the next section.

4.2   Experimental Procedure

Due to the small cross-section of an inelastic scattering event, IXS experiments can only be performed at a few synchrotron radiation sources around the world. The IXS experiments that are shown in the framework of this thesis were performed at the Taiwan inelastic X-ray scatting beamline BL12XU at SPring-8 (**S**uper **P**hoton **ring - 8** GeV) in Hyogo, Japan. The schematic setup of the beamline is shown in figure 4.3. X-rays are generated by a 4.5 m long in-vacuum undulator with a magnet period of 32 mm [241] and monochromatized by a Si(111) double-crystal monochromator with an energy width of 3 eV at 19.5 keV. The high resolution monochromator (HRM, see figure 4.3) was not used in this experiment. Subsequently, the beam is focused by Pt mirrors into a 30 μm $\times$ 30 μm spot. A phase retarding plate is additionally installed to maximize the flux at scattering angles in the region around 90 °, which is necessary due to the fact that the X-rays are parallel polarized and thus no signal can be detected at a scattering angle of 90 °. Further focusing is achieved by a Kirkpatrick-Baez mirror just in front of the sample, leading to a 15 μm $\times$ 40 μm spot with a flux of $5 \cdot 10^{12}$ photons per second at the sample position. After performing the scattering process at the sample, the beam is bragg reflected at a Si(660) analyzer crystal and is thereafter detected by a NaI(Tl) point detector. Sample, analyzer crystal and the detector are placed on a Rowland circle [117]. In this experiment, the scattering plane is in the horizontal plane, while the Rowland circle is in vertical geometry. This allows maximizing the intensity in forward scattering geometry. Moreover, silicon PIN diodes are available to monitor the beam intensity before or after the sample.

To investigate density disturbances in water as a function of water temperature, a custom made sample cell, which is produced by Dr. Nozomu Hiraoka[1] and is shown in figure 4.4 a), was used. The sample cell consists of a copper cylinder with a rectangular copper ground plate. The cylinder has a semicircular Kapton window for the X-ray path and an inner opening with a diameter of 15 mm for sample liquid storage. Moreover, the rectangular ground plate has two connections to be connected to a water flow cooling

---

[1]Dr. Nozomu Hiraoka, National Synchrotron Radiation Research Center, Hsinchu 30076, Taiwan
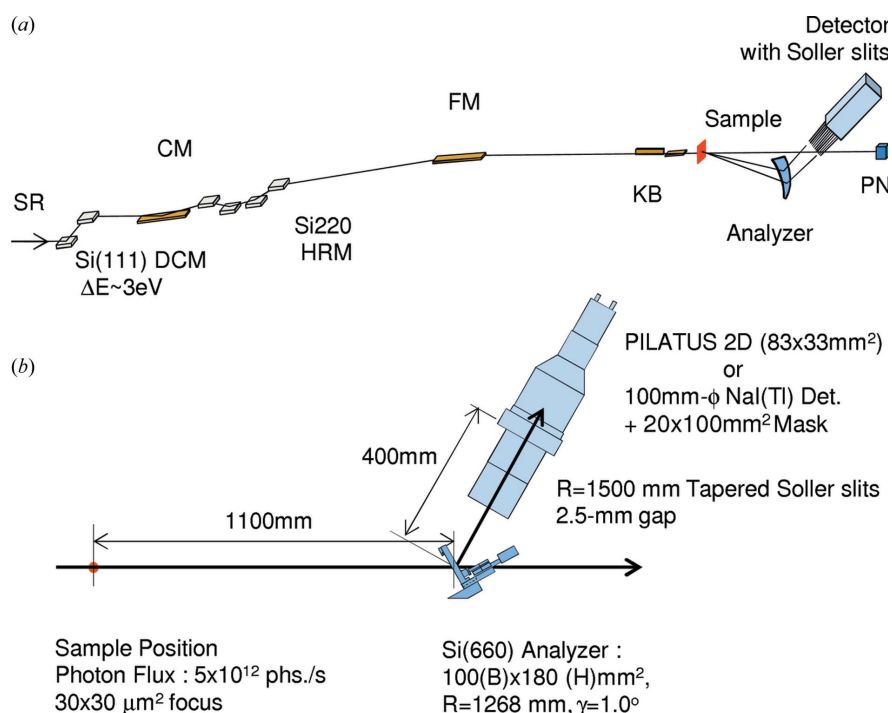
Figure 4.3: Schematic setup of the beamline BL12XU at SPring-8, published by Hiraoka et al. [242].
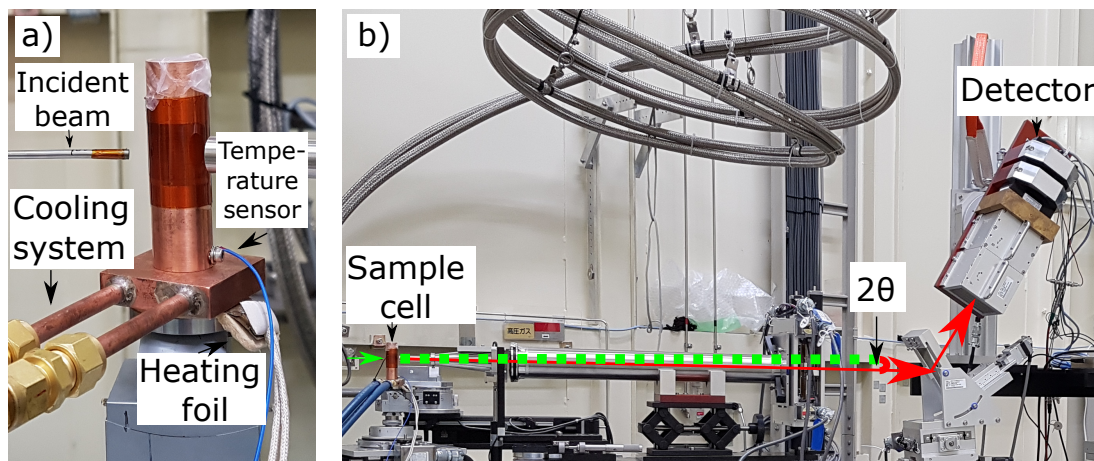
Figure 4.4: IXS sample cell (a)) and beamline BL12XU setup (b)).

system. This system is able to adjust the temperature of the whole sample cell in the temperature region between 0 °C and 95 °C with temperature fluctuations below 0.1 °C over the whole exposure time of the experiment. Additionally, a heating foil may be adapted below the sample cell to further ensure temperature stability.

Before installing the sample cell at the beamline, it is filled with degassed, ultrapure water and covered with sealing tape. A photograph of this setup is shown in figure 4.4 b). In addition to this, the beam path before (green) and after (red) the scattering process is marked and the path of the transmitted, not scattered beam is shown as a dotted green line to illustrate the scattering angle 2Θ.

With this setup, density disturbances in water were investigated at water temperatures of 4 °C, 20 °C and 90 °C. Therefore, the scattered intensity was recorded as a function of scattering angle 2Θ for angles in the region between 2 ° and 78 ° with a step size of 2 ° and in the region between 100 ° and 148 ° with a step size of 3 ° at an incident energy of 19.460 keV. Furthermore, measurements were performed for angles in the region between 55 ° and 73 ° with a step size of 2 ° and in the region between 91 ° and 142 ° with a step size of 3 ° at an incident energy of 25.540 keV. Thereby, a momentum transfer region between $0.34\,\text{Å}^{-1}$ and $24.48\,\text{Å}^{-1}$ was covered. The investigated energy transfer region was chosen as follows: -20 eV to 1000 eV energy transfer in the momentum transfer region between $0.34\,\text{Å}^{-1}$ and $4.77\,\text{Å}^{-1}$, -20 eV to 2000 eV in the momentum transfer region between $5.10\,\text{Å}^{-1}$ and $18.96\,\text{Å}^{-1}$ and -20 eV to 3000 eV for momentum transfers up to $24.48\,\text{Å}^{-1}$. This ensures to cover almost the complete Compton scattering profile within the chosen energy transfer region. Moreover, after each measurement, a shorter measurement was performed at a higher sample cell position, without any water in the flight path. This measurement is used to investigate the scattering of the empty cell for background subtraction. With all these measurements, one temperature could be investigated within two days.

After collection of the data, data analysis can be performed according to the procedure explained in section 4.1.

4.3 Imaging the Electron Density Disturbances in Water

The method presented by Abbamonte et al. [114, 118] is a powerful tool to extract electronic density disturbances in a sample system from IXS data. This section presents the analysis and results of IXS measurements of water at 4 °C, 20 °C and 90 °C. First, it is necessary to extract the dynamic structure factor from measured data. This will be presented in the next subsection. Afterwards, electron density disturbances in water will be shown at different time positions on attosecond time scales. Moreover, momentum and energy transfer dependencies on the results will be discussed in order to find the momentum and energy transfer regions that are necessary to be investigated to achieve results with desired precision. Thereafter, time resolved electron density disturbance evolution will be presented as a function of water temperature. Finally, this chapter will finish with a short conclusion of the gathered results and an outlook on further projects.

4.3.1 The Dynamic Structure Factor

Knowledge about the dynamic structure factor is necessary for investigating electronic density disturbances in water on attosecond time scales. However, the measured data contains several other contributions besides the dynamic structure factor. Hence, the first step of data analysis is the correction of the measured data with regards to these contributions. Due to the fact that high energy and momentum transfer regions were measured, Compton scattering contributions have the greatest impact on the measured IXS data. Therefore, the data underlies corrections, which are specific for Compton scattering experiments. In a Compton scattering experiment, the measured intensity I can be written as [239]

$$I = B + C \cdot (J + M) \tag{4.15}$$

with background scattering B, an energy dependent correction factor C, the experimental Compton profile J and multiple scattering contributions M. The goal is to extract the experimental Compton scattering profile, since it is correlated to the dynamic structure factor via

$$S\left(k, \omega\left(\mathrm{p_z}\right)\right) = \frac{m}{\hbar k} J\left(p_\mathrm{z}\right) \tag{4.16}$$

with

$$p_\mathrm{z} = \frac{m_\mathrm{e}\omega}{k} - \frac{\hbar k}{2} \approx m_\mathrm{e}c \left(\frac{\hbar\omega_1 - \hbar\omega_2 - \left(\hbar^2\omega_1\omega_2 / \left(m_\mathrm{e}c^2\right)\right)\left(1 - \cos\left(\Theta\right)\right)}{\sqrt{\hbar^2\omega_1^2 + \hbar^2\omega_2^2 - 2\hbar^2\omega_1\omega_2\cos\left(\Theta\right)}} \right) \tag{4.17}$$

under the consideration of a radial symmetric sample cell. Therefore, first the energy transfer axis is calibrated with regards to the elastic line and the measured background scattering is subtracted. Moreover, contributions from the tails of the elastic line have an impact on the measured IXS data. Due to the fact that already at small energy transfer values contributions from valence band electrons and plasmons occur (see figure 4.2), being overlapped by the tails of the elastic line, it is not possible to solely subtract the part of the elastic line with at positive energy transfer values. Instead, the part of the elastic line at negative energy transfer values is mirrored to positive energy transfer values and subtracted from the measured data.

Thereafter, the energy dependent correction factor C is calculated and the measured data is divided by this factor. The energy dependent factor C is a product of four correction components including the corrections for air absorption C_air, sample absorption C_sample, reflectivity of the analyzer crystals C_ac and the relativistic cross section C_rel.
The correction factor for air absorption contains the air absorption of the scattered X-rays with energy E via [239]

$$C_\mathrm{air} = e^{-d_\mathrm{air}\mu_\mathrm{air}(E)}. \tag{4.18}$$

Here, $d_\mathrm{air} = 150\,\mathrm{cm}$ denotes the distance between the sample and the detector and $\mu_\mathrm{air}(E)$ is the energy dependent absorption coefficient for air (calculated via the "Photon

Cross Section Database" of the National Institute of Standards and Technology [243]). Due to a constant incident energy, only air absorption of the scattered X-rays contributes to the correction factor C_{air}.

In the case of the sample's absorption factor, both the incident and the scattered X-rays have to be taken into account, leading to the absorption coefficient $\mu_{\text{sample}} = \mu(E_1) + \mu(E)$, where E_1 denotes the incident energy. Hence, the correction factor for sample absorption with the chosen sample geometry and sample thickness $d_{\text{sample}} = 15\,\text{mm}$ can be calculated by

$$C_{\text{sample}} = \frac{1 - e^{-d_{\text{sample}}\mu_{\text{sample}}}}{d_{\text{sample}}\mu_{\text{sample}}}. \tag{4.19}$$

The energy dependent reflectivity of the analyzer crystals is beamline specific and thus the correction factor C_{ac} is provided by the beamline scientist of beamline BL12XU, Dr. Nozomu Hiraoka.

The last required correction factor to determine C is the correction factor for the relativistic cross section. Due to the fact that IXS experiments are performed at energies higher than $25\,\text{keV}$, relativistic effects have to be taken into account. The influence of relativistic effects on X-ray Compton scattering experiments is well discussed in literature [244, 245, 246, 247, 234]. For this experiment, the relativistic cross section is therefore described by

$$C_{\text{rel}} = \frac{R_1}{R_2} + \frac{R_2}{R_1} - 2\sin^2(\Theta)\cos^2(\beta) \tag{4.20}$$

with the angle β between the scattering plane and the polarization vector of the incident beam. The factors R_1 and R_2 are defined by

$$R_1 = \hbar\omega_1\left(m_e c^2 - (\omega_1 - \omega_2\cos(\Theta))\frac{p_z}{\hbar k}\right) \tag{4.21}$$

$$R_2 = R_1 - \hbar^2\omega_1\omega_2(1 - \cos(\Theta)). \tag{4.22}$$

After the determination of all the factors for the correction factor C, the data can be divided by this correction factor, so that the last remaining step is to subtract multiple scattering effects to obtain the Compton scattering profile and thus the dynamic structure factor.

In an experiment, a finite probability for multiple scattering events is given, which depends on the incident energy and polarisation of the X-rays as well as the sample geometry and scattering angle. Multiple scattering affects the shape of the Compton profile, leading to asymmetries in the measured data. Several programs have been presented to calculate the multiple scattering contribution on the measured data utilizing a Monte Carlo code over the last decades [248, 249, 250, 251], resulting in the development of the program MUSCAT [252] that has been used to calculate multiple scattering effects. With this program, single and multiple scattering events can be separated from the data to subtract the multiple scattering effects and correct the data.

After the multiple scattering effects are subtracted, the Compton scattering profile is obtained and the dynamic structure factor can be determined. Finally, the data is normalized by the f-sum rule [117]

$$\int_0^\infty \omega \cdot S\left(k,\omega\right) \mathrm{d}\omega = \frac{\hbar k^2}{2m_e} \tag{4.23}$$

and extrapolated on a larger energy transfer axis (up to $5\,\mathrm{keV}$ using a tail of a gaussian function) as proposed by Abbamonte et al. [114, 118], to preserve causality in the final result (see also section 4.1). Furthermore, even after the subtraction of the elastic line, there are still small contributions at low energy transfer values. However, inelastic scattering is defined to converge towards zero for very small energy transfer values. Therefore, at energy transfer values below $10\,\mathrm{eV}$, the measured data is corrected by a tail of a Gaussian function. The imaginary part of the propagator $\chi\left(\mathbf{k},\omega\right)$ is then calculated via equation 4.10. A comparison between the corrected and the raw data is shown in figure 4.5 for a small momentum transfer value (a)) and a large momentum transfer value (b)). Here, the raw data was multiplied by a factor to achieve an equal intensity at the maximum of the Compton profile for comparison reasons. For both momentum transfer values, the figure shows only small deviations from the raw data to the corrected data, exhibiting the good data quality of the measurements. However, at small energy transfer values, corrections are necessary to extract the elastic line's contributions. Furthermore, the corrections lead to an increase of the Compton profile symmetry.

Finally, using this procedure, the imaginary part of the propagator $\chi\left(\mathbf{k},\omega\right)$ can be calculated for all temperatures and is shown in figures 4.6, 4.7 and 4.8. Figure 4.6 presents a 2-D plot of the imaginary part of the propagator as a function of momentum
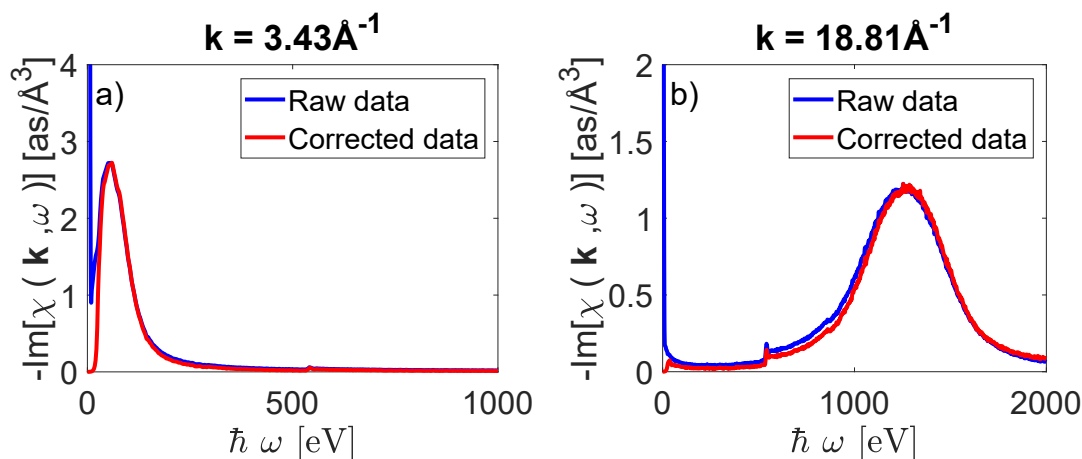
Figure 4.5: Comparison between raw and corrected IXS data for a small momentum transfer value (a)) and a large momentum transfer value (b)). for comparison reasons, The raw data is multiplied by a factor to match the intensity value at the maximum of the Compton profile.

transfer on the x-axis and energy transfer on the y-axis, while figure 4.7 shows the imaginary part of the propagator as a function of momentum transfer and figure 4.8 exhibits the imaginary part of the propagator as a function of energy transfer.
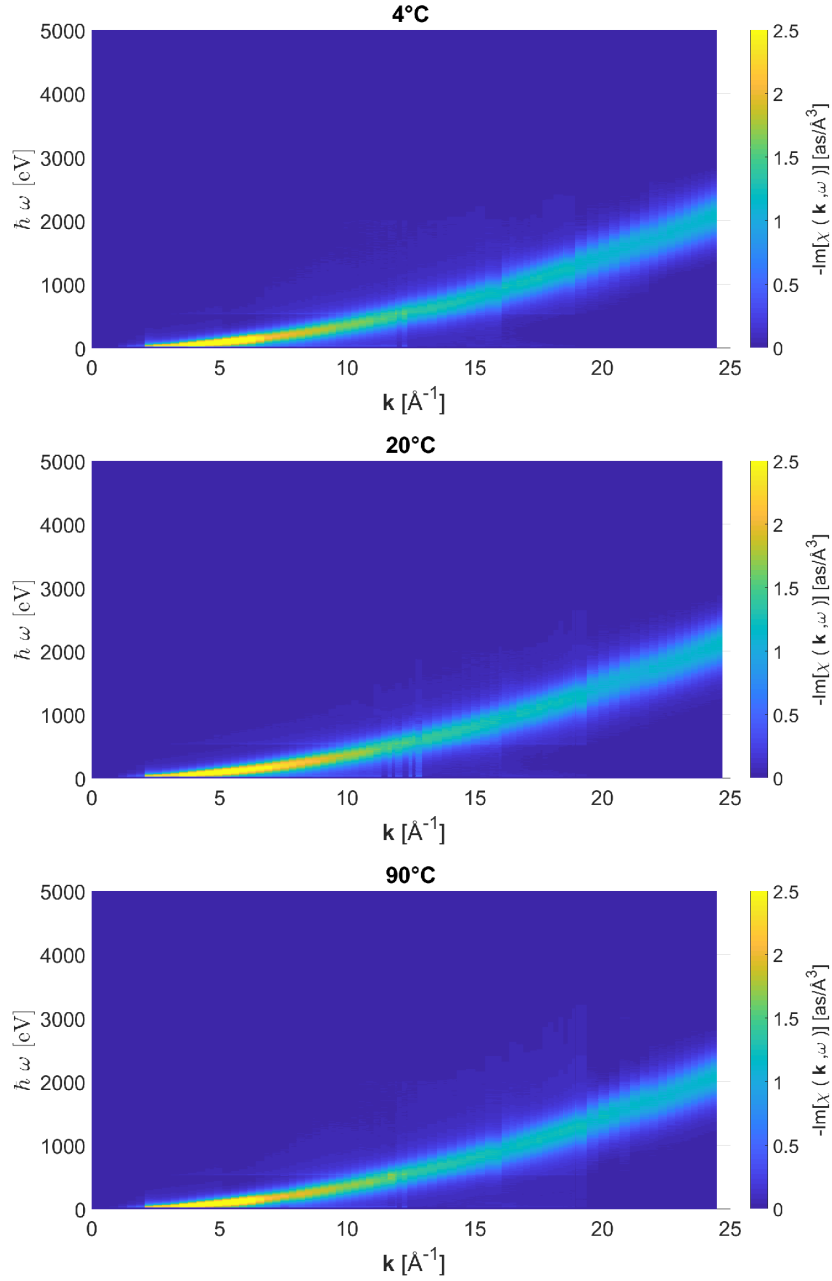
Figure 4.6: The imaginary part of the propagator $\chi\,(\mathbf{k},\omega)$ is shown for water temperatures of 4 °C, 20 °C and 90 °C as a function of momentum transfer on the x-axis and energy transfer on the y-axis.
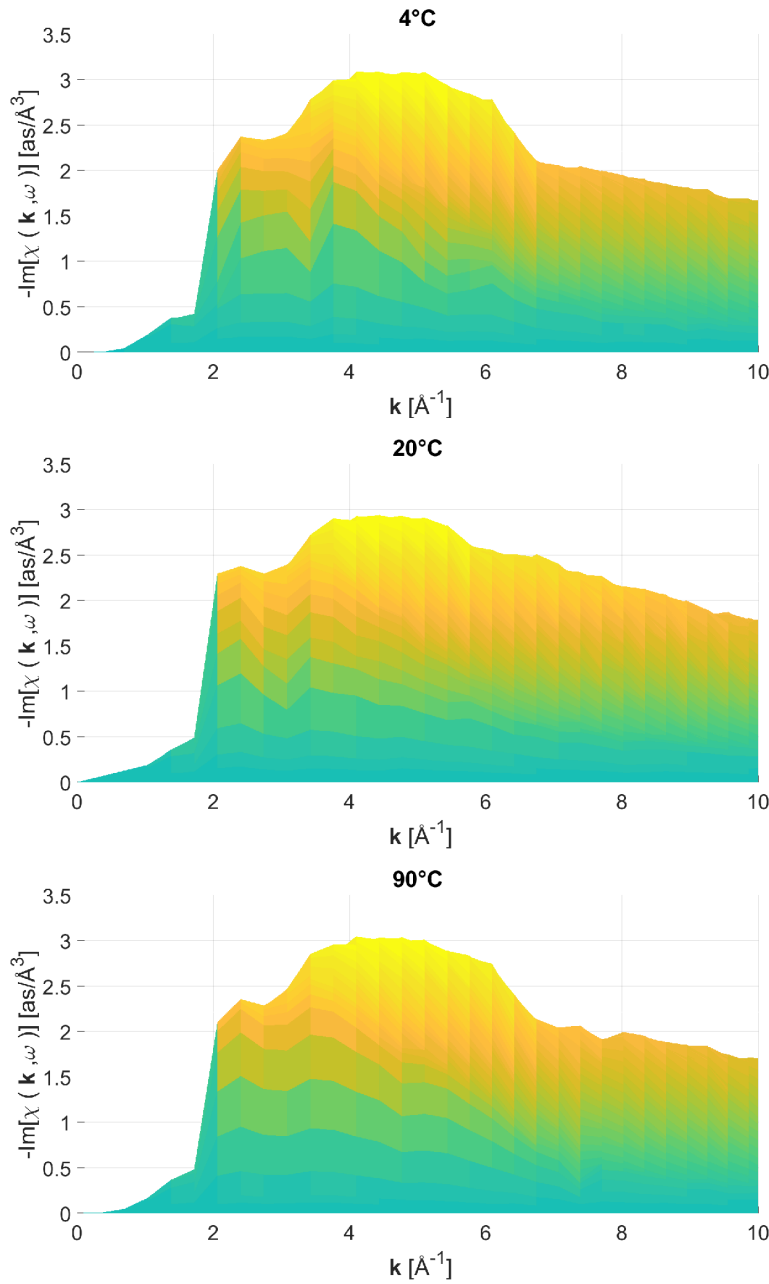
Figure 4.7: The imaginary part of the propagator $\chi(\mathbf{k},\omega)$ is shown for water temperatures of 4 °C, 20 °C and 90 °C as a function of momentum transfer.

The figures 4.6, 4.7 and 4.8 present the differences in the imaginary part of the propagator $\chi(\mathbf{k},\omega)$ for all temperatures. Only small differences occur upon temperature variation. In all cases, the propagator has its maximum in the momentum transfer region around $4.8\,\text{Å}^{-1}$ and in the energy transfer region around $80\,\text{eV}$ extending over
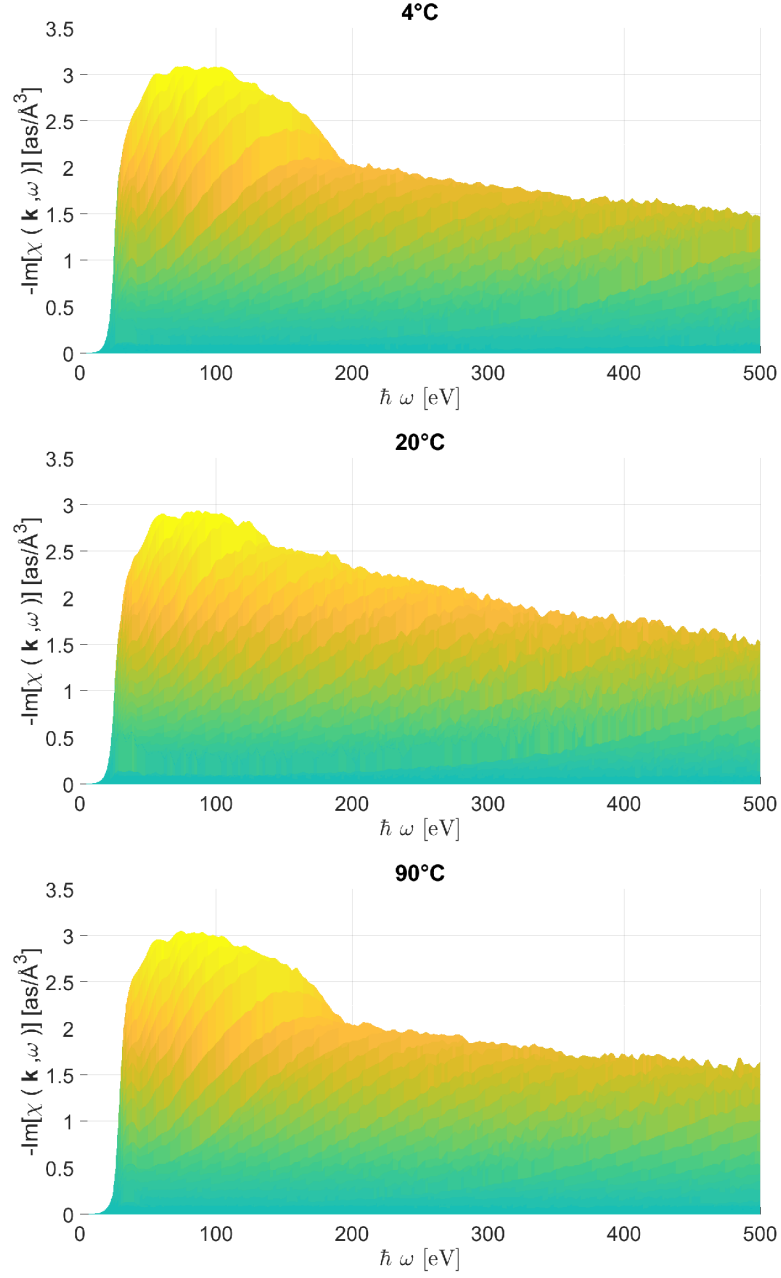
Figure 4.8: The imaginary part of the propagator $\chi(\mathbf{k},\omega)$ is shown for water temperatures of 4 °C, 20 °C and 90 °C as a function of energy transfer.

a range of $\pm 1\,\text{Å}^{-1}$ and $\pm 40\,\text{eV}$. For larger momentum and energy transfers, the intensity of the imaginary part of the propagator drops rapidly to 80% of the maximal value and lower. Since the imaginary part of the propagator $\chi(\mathbf{k},\omega)$ already contains all the information on the system's evolution in time, differences in the shape of its

maximum already hint differences in the system's evolution in time that will be further investigated in the next sections.

4.3.2 Imaging The Electron Density Disturbances

After deriving the imaginary part of the propagator $\chi(\mathbf{k},\omega)$, it is possible to proceed with the determination of the propagator $\chi(\mathbf{x},t)$ according to the instruction given in section 4.1. In the last subsection, the data was already symmetrized and analytically continued to an energy transfer region up to 5000 eV. Therefore, the next step is to perform a Fourier transform to obtain $\chi(\mathbf{k},t)$. Therefore, both possible pathways were tested to obtain $\chi(\mathbf{x},t)$ as discussed in section 4.1. First, the real part of $\chi(\mathbf{k},\omega)$ was calculated with equation 4.12. The real and imaginary parts of $\chi(\mathbf{k},\omega)$ for a small and a large momentum transfer value are shown in figure 4.9. Besides main features around 0 eV, two additional peaks in the propagator $\chi(\mathbf{k},\omega)$ at energy transfer values of -535 eV and 535 eV occur, which are stronger pronounced at large momentum transfer values compared to small momentum transfer values. These peaks are the result of the stronger pronounced oxygen K-edge of the propagator $\chi(\mathbf{k},\omega)$ at measurements at high momentum transfers.
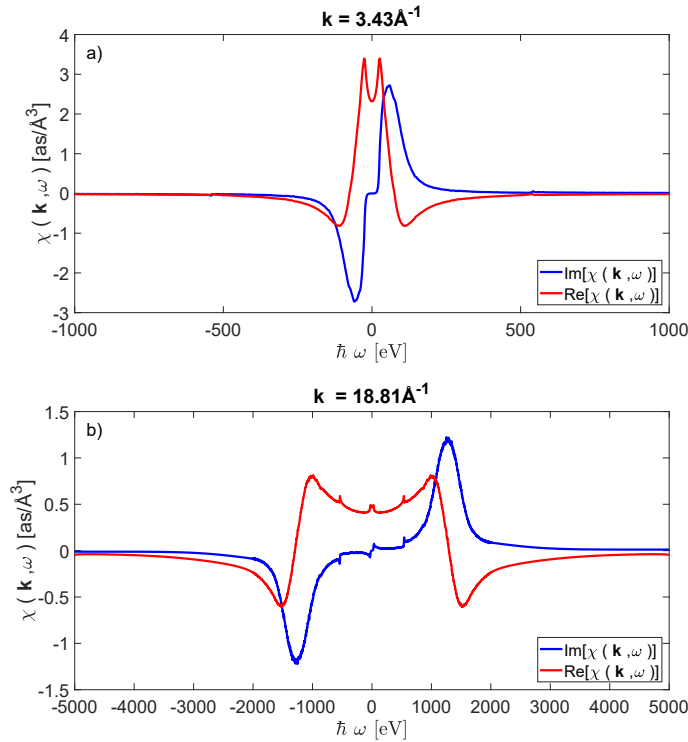
Figure 4.9: Real and imaginary part of the propagator $\chi(\mathbf{k},\omega)$ shown for a small momentum transfer value (a)) and a large momentum transfer value (b)).

With the real and imaginary part of $\chi(\mathbf{k},\omega)$, it was completely reconstructed and

a Fourier transform via equation 4.13 was performed. Alternatively, also the Fourier transform of twice the imaginary part of $\chi\,(\mathbf{k},\omega)$ was performed via equation 4.11. The results of both pathways are shown in figure 4.10 again for a small and a large momentum transfer value. Here, $\chi_1\,(\mathbf{k},t)$ denotes $\chi\,(\mathbf{k},t)$ calculated as a Fourier transform of the real and imaginary part of $\chi\,(\mathbf{k},\omega)$ and $\chi_2\,(\mathbf{k},t)$ is calculated by a Fourier transform of twice the imaginary part of $\chi\,(\mathbf{k},\omega)$. Figure 4.10 points out that both pathways lead to identical results.
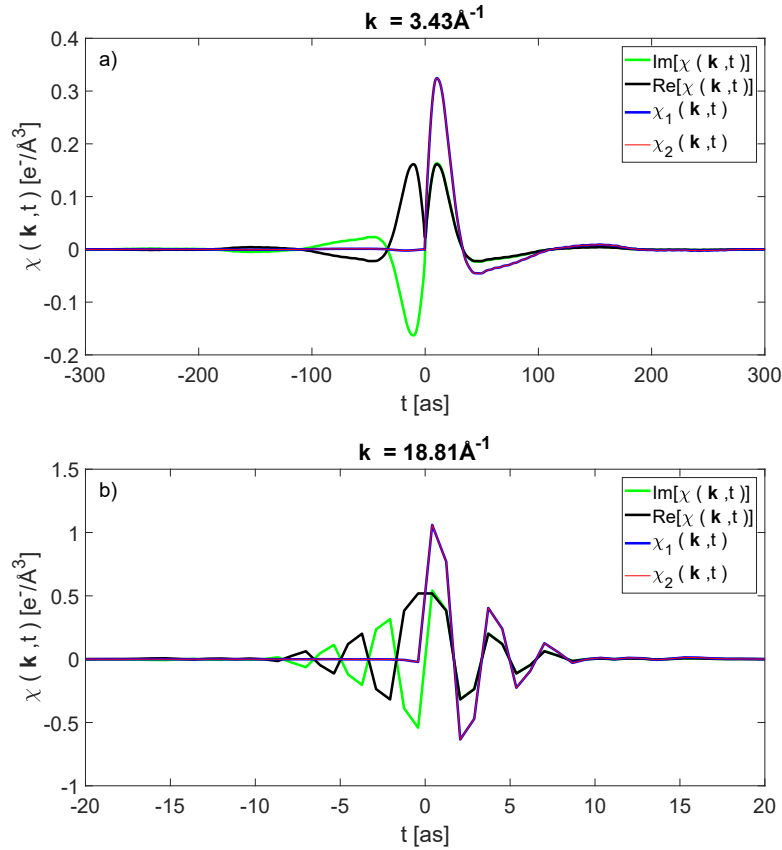
Figure 4.10: Comparison of the both possible pathways to determine $\chi\,(\mathbf{k},t)$ shown for a small momentum transfer value (a)) and a large momentum transfer value (b)). Here, $\chi_1\,(\mathbf{k},t)$ is the sum of the Fourier transforms of the real and imaginary part of $\chi\,(\mathbf{k},\omega)$, while $\chi_2\,(\mathbf{k},t)$ is the Fourier transform of twice the imaginary part of $\chi\,(\mathbf{k},\omega)$.

After deriving $\chi\,(\mathbf{k},t)$, the propagator $\chi\,(\mathbf{x},t)$ can finally be calculated by a spatial Fourier transformation. With measured momentum transfers up to $24.48\,\mathrm{\AA}^{-1}$ and energy transfers up to $3000\,\mathrm{eV}$, $\chi\,(\mathbf{k},t)$ is determined with a spatial resolution of $0.26\,\mathrm{\AA}$ and a resolution on the time axis of $1.38\,\mathrm{as}$. However, due to the extrapolation of the energy transfer axis up to $5000\,\mathrm{eV}$, the resolution of the time axis is even reduced to $0.82\,\mathrm{as}$. This reduction of time resolution may lead to incorrect conclusions of the results, because some time points are calculated instead of measured. However, due to the fact

that at all measurements almost the complete Compton profile was measured within the observed energy transfer regions, the extrapolation of the energy transfer axis only covers the end of the tails of the Compton profile and hence should not influence the results. Figure 4.11 a) shows the final result of $\chi(\mathbf{x},t)$ after the spatial Fourier transformation as a function of $\mathbf{x}$ as an example at 32.62 as. This result can also be shown in 3D by a 360° rotation of the x-axis (see figure 4.11 b)), assuming a rotational invariance of the propagator $\chi(\mathbf{x},t)$.
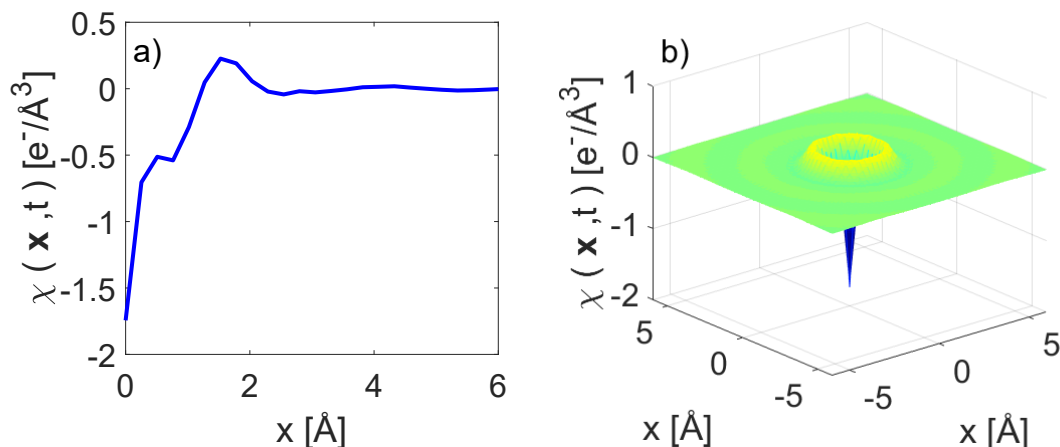
Figure 4.11: a) Snapshot of the evolution of the propagator $\chi(\mathbf{x},t)$ at 32.62 as for water at 20°C. b) The evolution of the propagator $\chi(\mathbf{x},t)$ at 32.62 as for water at 20°C is shown in 3D by a 360° rotation of the x-axis.

Figure 4.11 describes the evolution of the disturbance in electron density 32.62 as after the interaction of a photon with an electron. Here, the amplitude of $\chi(\mathbf{x},t)$ denotes electron density differences compared to the electron density at the time of interaction ($t = 0\,\text{s}$). There is a strong negative amplitude of the propagator at $x = 0\,\text{Å}$, fading away oscillating at higher distances, with the strongest amplitude at the position of $1.53\,\text{Å}$. Investigating further snapshots as a function of time, one can precisely describe the evolution of the density disturbance. This will be done in section 4.3.4 for all three measurements, but first, the dependency of the data quality on the momentum and energy transfer is investigated in the next subsection.

4.3.3 Momentum and Energy Transfer Dependency

As already introduced at the beginning of this chapter, density disturbances in water were already investigated with IXS on attosecond time scales by Abbamonte et al. [114]. However, there are differences between the results obtained in this experiment compared to Abbamonte et al. (see figure 4.12). In the experiment performed by Abbamonte et al., the main feature in the $\chi(\mathbf{k},\omega)$ spectrum occurs in the energy transfer region of the water plasmon and in the momentum transfer region around $2\,\text{Å}^{-1}$, while in this

experiment the maximum in $\chi(\mathbf{k},\omega)$ occurs from the Compton profile contribution in the energy transfer region around $100\,\mathrm{eV}$ and in the momentum transfer region around $5\,\mathring{A}^{-1}$. Nevertheless, final results on $\chi(\mathbf{x},t)$ show numerous similarities (see also figure 4.12). A key factor to determine $\chi(\mathbf{k},\omega)$ is the correct application of the f-sum rule (see equation 4.23). Due to the fact that the integral is performed over $\omega\cdot S(\mathbf{k},\omega)$, a profound insight specifically on the contributions at high energy transfer values is necessary. Furthermore, as shown in figure 4.5, the maximum of the Compton scattering profile shifts both in momentum and energy transfer towards higher values, resulting in an increased complexity for extrapolation of the data at higher momentum transfer values, as performed by Abbamonte et al [114]. Hence, a systematic analysis of the impact on the momentum and energy transfer ranges on the final results is necessary to estimate the quality of the results.
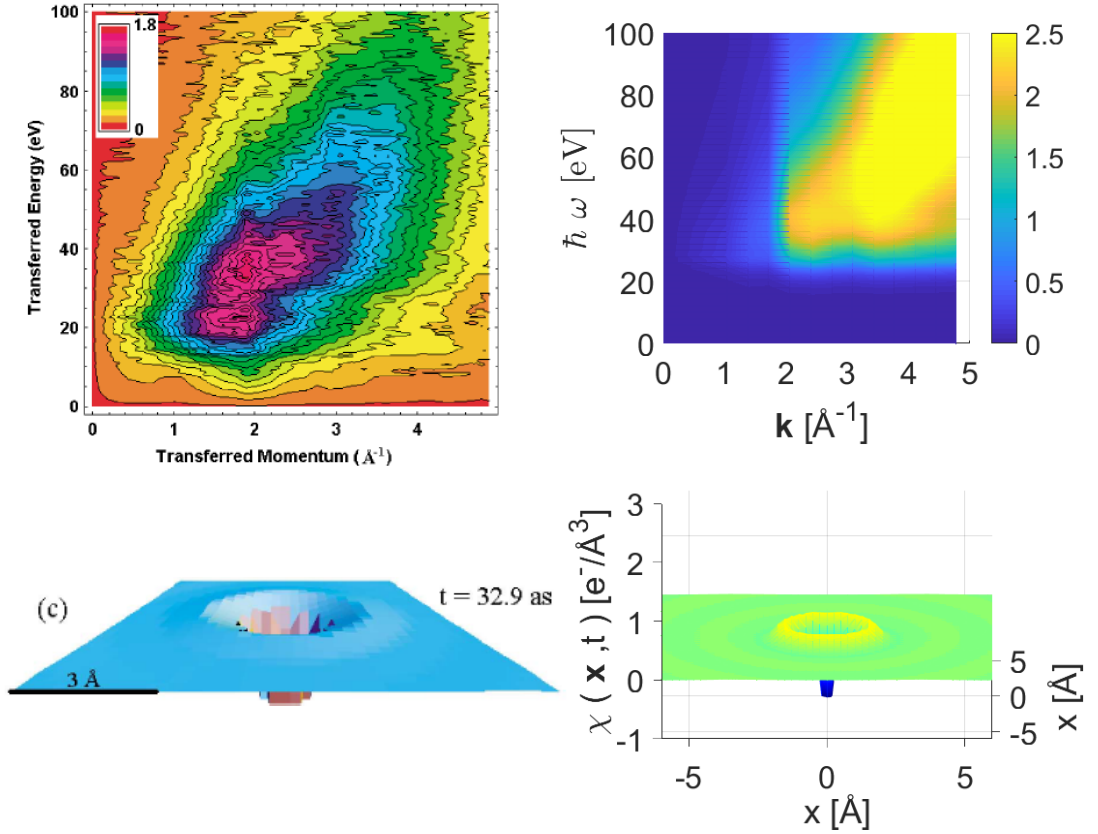
Figure 4.12: Top: Comparison of $\chi(\mathbf{k},\omega)$ obtained by Abbamonte et al. [114] (left) and in this experiment (right, inset of the middle figure in figure 4.6). Bottom: Comparion of the snapshots of $\chi(\mathbf{x},t)$ calculated by Abbamonte et al. [114] (left) at $32.9\,\mathrm{as}$ and in this experiment (right, see also figure 4.11) at $32.6\,\mathrm{as}$.

For the systematic analysis of the impact on the momentum and energy transfer range

on $\chi\left(\mathbf{x},t\right)$, momentum transfers of up to $5\,\text{Å}^{-1}$, $10\,\text{Å}^{-1}$, $15\,\text{Å}^{-1}$, $20\,\text{Å}^{-1}$ and $24.48\,\text{Å}^{-1}$ were investigated, respectively, while the energy transfer region was simultaneously varied in the region of up to $200\,\text{eV}$, $500\,\text{eV}$, $1000\,\text{eV}$, $1500\,\text{eV}$, $2000\,\text{eV}$ and $3000\,\text{eV}$, respectively. The normalization of the spectra is performed as previously in the case of energy transfer ranges that are large enough to perform this normalization. For smaller energy transfer ranges, the normalization is performed over the full energy transfer range. To obtain the impact of this variation, snapshots at all points in time were first calculated for the propagator $\chi\left(\mathbf{x},t\right)_{ref}$ with the best spatial and time resolution (with a momentum transfer region of up to $24.48\,\text{Å}^{-1}$ and an energy transfer region of up to $3000\,\text{eV}$), which is chosen as reference for the following comparison. Thereafter, the propagators $\chi\left(\mathbf{x},t\right)_{\mathbf{k},t}$ were calculated for combinations of all other momentum transfer and energy transfer regions. Due to the fact that the resolution of the propagators $\chi\left(\mathbf{x},t\right)_{\mathbf{k},t}$ is worse compared to $\chi\left(\mathbf{x},t\right)_{ref}$, missing points on the space axis were calculated by linear interpolation. Points missing on the time axis were omitted in case of lacking temporal resolution. Subsequently, for each point in time, the linear interpolated data of $\chi\left(\mathbf{x},t\right)_{\mathbf{k},t}$ was subtracted from $\chi\left(\mathbf{x},t\right)_{ref}$ and the resulting, absolute values were summed to obtain a difference value. Finally, this difference value was normalized by the number of investigated time points to be comparable for all combinations of $\chi\left(\mathbf{x},t\right)_{\mathbf{k},t}$, calling it Δ henceforth. The value was determined in the spatial region between -6 Å and 6 Å and in the time region between -1000 as and 1000 as due to the fact that beyond these regions only background signal occurred.

Figure 4.13 represents the differences Δ as a function of momentum transfer for all investigated energy transfer regions. It clearly shows that with rising maximum momentum transfers the difference value Δ decreases significantly. This is most likely caused by a better spatial resolution, resulting in less differences due to less necessary interpolation points of the data (see figure 4.14 a) for graphical details). Furthermore, increasing the energy transfer region results in an increase of Δ, even though the time resolution becomes better with increasing energy transfer region. However, this effect can be neglected due to the approach by which Δ is calculated. Since there is no interpolation on the time axis, errors between two time points are neglected. Hence, only differences on the space axis are investigated by Δ as a function of momentum transfer for different energy transfer regions. Nevertheless, as shown in figure 4.5 b), it is necessary to obtain information on large energy transfer regions when investigating high momentum transfer regions due to the fact that the maximum of the Compton profile shifts towards higher energy transfer values.

The impact of momentum and energy transfer is shown for two examples in figure 4.14. Using momentum transfer regions with different maximum momentum transfer values, starting with $5\,\text{Å}^{-1}$ up to $24.48\,\text{Å}^{-1}$, result in different spatial resolutions, which are shown for the snapshot taken at 32.6 as in figure 4.14 a). Here, for example, only the largest momentum transfer region enables resolving the shoulder at 0.5 Å. Reducing the momentum transfer region, and thus the spatial resolution, lead to significant differences in obtained structures, e.g. for $5\,\text{Å}^{-1}$. This was also determined in the case of time resolution, which is shown in figure 4.14 b) for the electron density disturbance
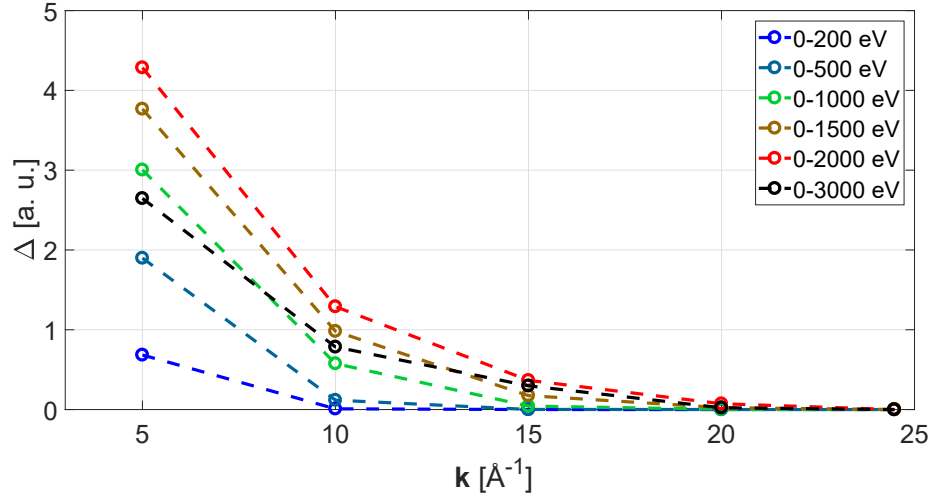
Figure 4.13: The difference value Δ is shown as a function of momentum transfer for different energy transfer regions.
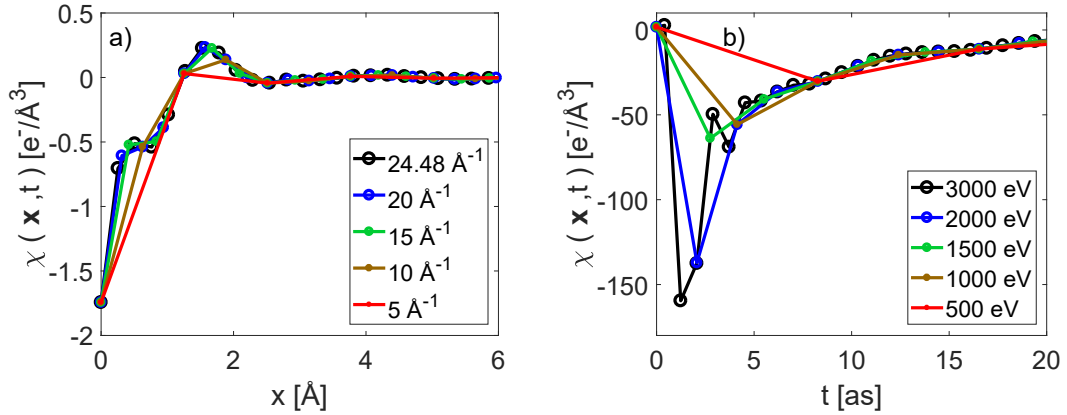
Figure 4.14: a) The impact of space resolution on $\chi\left(\mathbf{x},t\right)$ is shown as a function of momentum transfer energy on a snapshot at 32.6 as. b) The impact of time resolution on $\chi\left(\mathbf{x},t\right)$ is shown as a function of energy transfer for the electron density disturbance evolution at $x = 0\,\text{Å}$.

evolution at $x = 0\,\text{Å}$. Here, features in the region of up to 5 as can only be resolved by the largest investigated energy transfer region. Therefore, especially at small time and space regions, the investigation of large energy and momentum transfers is crucial to obtain correct results for the propagator $\chi\left(\mathbf{x},t\right)$.

After the impact of momentum and energy transfer regions on $\chi\left(\mathbf{x},t\right)$ is discussed, the electron density disturbance evolution is presented for all three investigated temperatures in the next subsection. Here, the maximally investigated momentum and energy

transfer regions were chosen to determine $\chi(\mathbf{x},t)$.

4.3.4 Time Resolved Density Disturbance Evolution

The evolution of disturbances in electron density in water for water temperatures of 4 °C, 20 °C and 90 °C at different time points after the scattering event is presented in figures 4.15, 4.16 and 4.17.

Before 0 as, which is equal to the time before the interaction between X-rays and water's electrons, no disturbance in electron density is expected. This is the case as shown in figure 4.15 a) (with the exception of small noise effects due to a finite energy transfer and momentum transfer scale before the Fourier transformation). At $t = 0$ as (see figure 4.15 b)), the electron density disturbance appears as a strong maximum in $\chi(\mathbf{x},t)$ at the point of interaction ($x = 0$ Å), fading out rapidly with rising distance to the interaction point. However, due to the time resolution of 0.82 as, a correct calculation of $\chi(\mathbf{x},t)$ at $t = 0$ as is difficult. On small time scales, a strong decrease in the electron density is expected due to the X-ray interaction with electrons. This is observed already after one attosecond (see figure 4.15 c)), when at the interaction point a minimum occurs. In the following, the first maximum of the electron density disturbance wave is propagating, represented by a broadening of $\chi(\mathbf{x},t)$ in space at 4 as (see figure 4.15 d)). At 15 as (see figure 4.16 a)), the first maximum of the electron density disturbance wave already propagated to a distance of 1 Å from the interaction point, while the minimum at the point of interaction is about to switch into a maximum. Before 40 as (see figure 4.16 b)), the turnover of the minimum into a maximum is completed, when also first differences as a function of temperature occur. This is represented by an increase of the amplitude of $\chi(\mathbf{x},t)$ at the point of interaction, which becomes larger with rising temperature, indicating a faster evolution of $\chi(\mathbf{x},t)$ at 90 °C.

The intensity of the first maximum of the electron density disturbance wave slowly decreases with proceeding time, while a second maximum of the electron density disturbance wave is about to be emitted at 66 as, represented by a broadening of $\chi(\mathbf{x},t)$ at the point of interaction (see figure 4.16 c)). With proceeding time, differences in the density disturbance evolution velocity as a function of temperature are apparent too, being mostly pronounced at zero points of the amplitude of $\chi(\mathbf{x},t)$ at the point of interaction. As shown in figure 4.16 d) at 116 as, the amplitude of $\chi(\mathbf{x},t)$ is still positive at 4 °C, almost zero at 20 °C and negative at 90 °C. This means, that the electron density disturbance evolves faster at 90 °C than at 20 °C and 4 °C. With further proceeding time (see figures 4.17 a)-c)), the amplitude movement of $\chi(\mathbf{x},t)$ at the point of interaction is similar in the case of 4 °C and 20 °C, while it is completely opposite at 90 °C. Finally, at times above 600 as, the electron density disturbance is almost completely faded out and only a small impact at the point of interaction is still noticeable (see figure 4.17 d)).

In the following, differences in the evolution of electron density disturbance maxima as a function of temperature are investigated. Therefore, the amplitude of $\chi(\mathbf{x},t)$ at the point of interaction is plotted as a function of time for all three temperatures in figure 4.18.
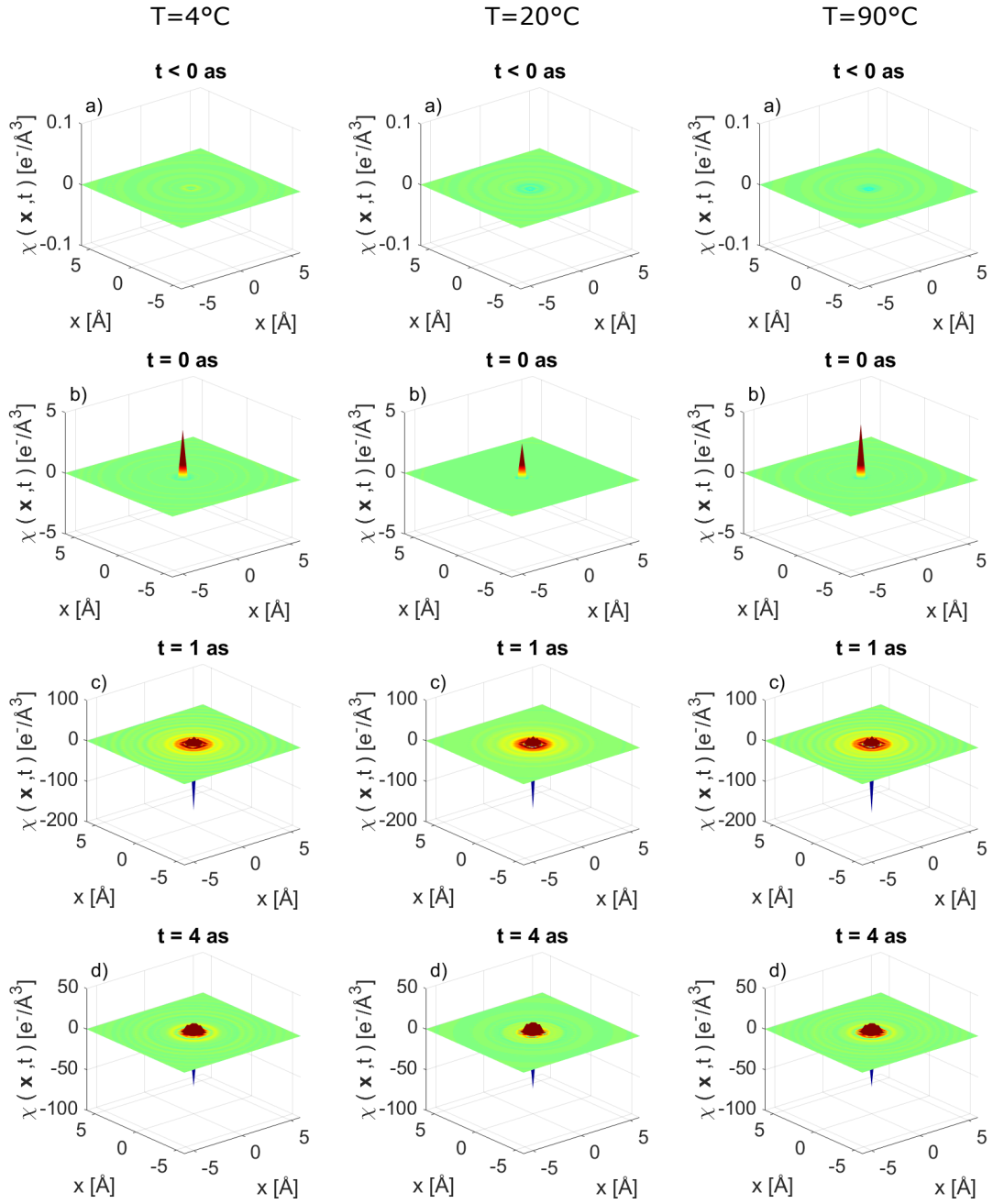
Figure 4.15: Electron density disturbance evolution in water for 4 °C (left), 20 °C (middle) and 90 °C (right) at following time points: a) <0 as, b) 0 as, c) 1 as and d) 4 as.

Figure 4.18 shows that the amplitude of $\chi(\mathbf{x},t)$ at the point of interaction has the largest absolute values for all three temperatures on short time scales. Directly after the
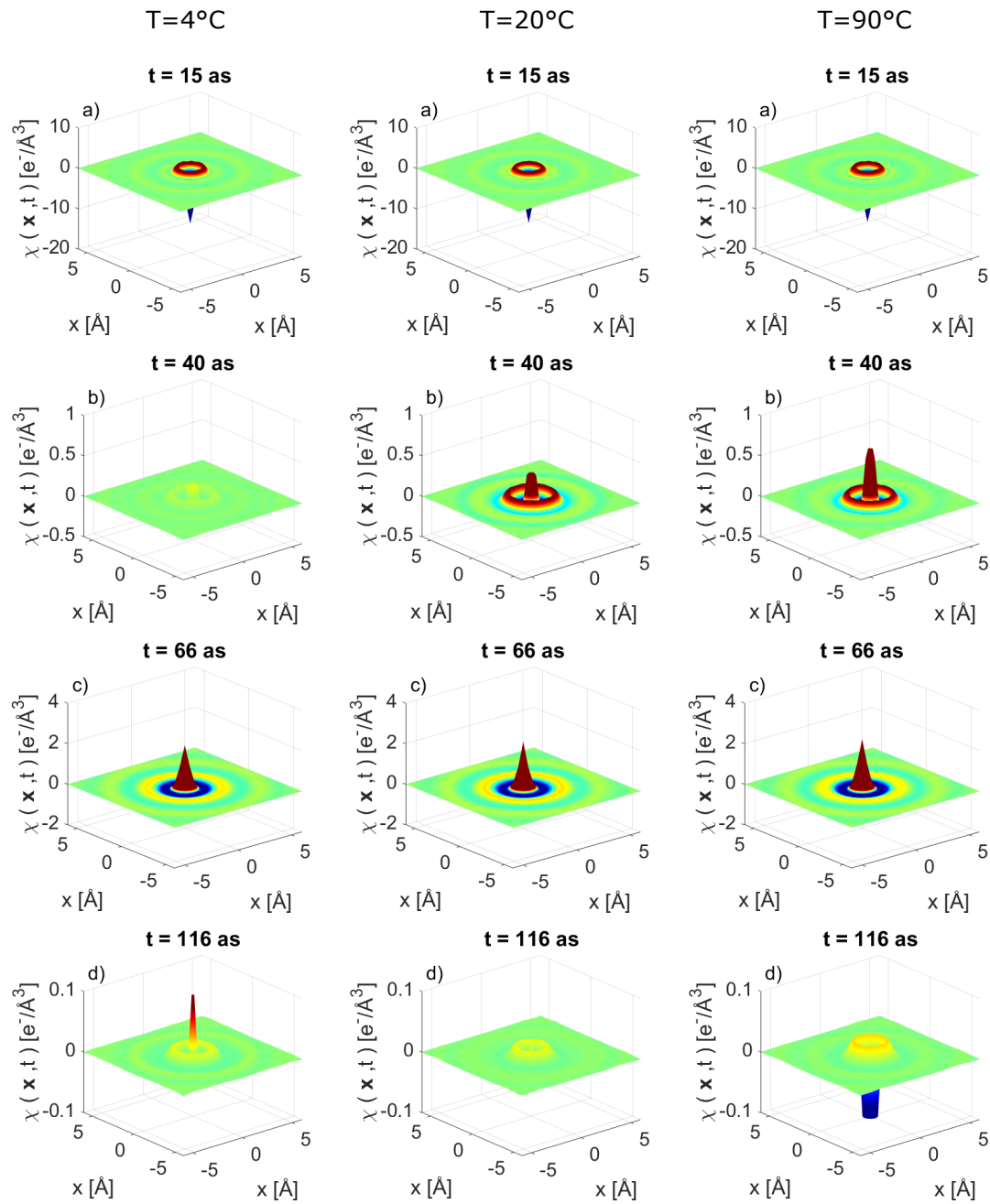
Figure 4.16: Electron density disturbance evolution in water for 4 °C (left), 20 °C (middle) and 90 °C (right) at following time points: a) 15 as, b) 40 as, c) 66 as and d) 116 as.

interaction at $t > 0$ as, the amplitude decreases on short time scales. This is the moment when the first maximum of the electron density disturbance wave is emitted, which is
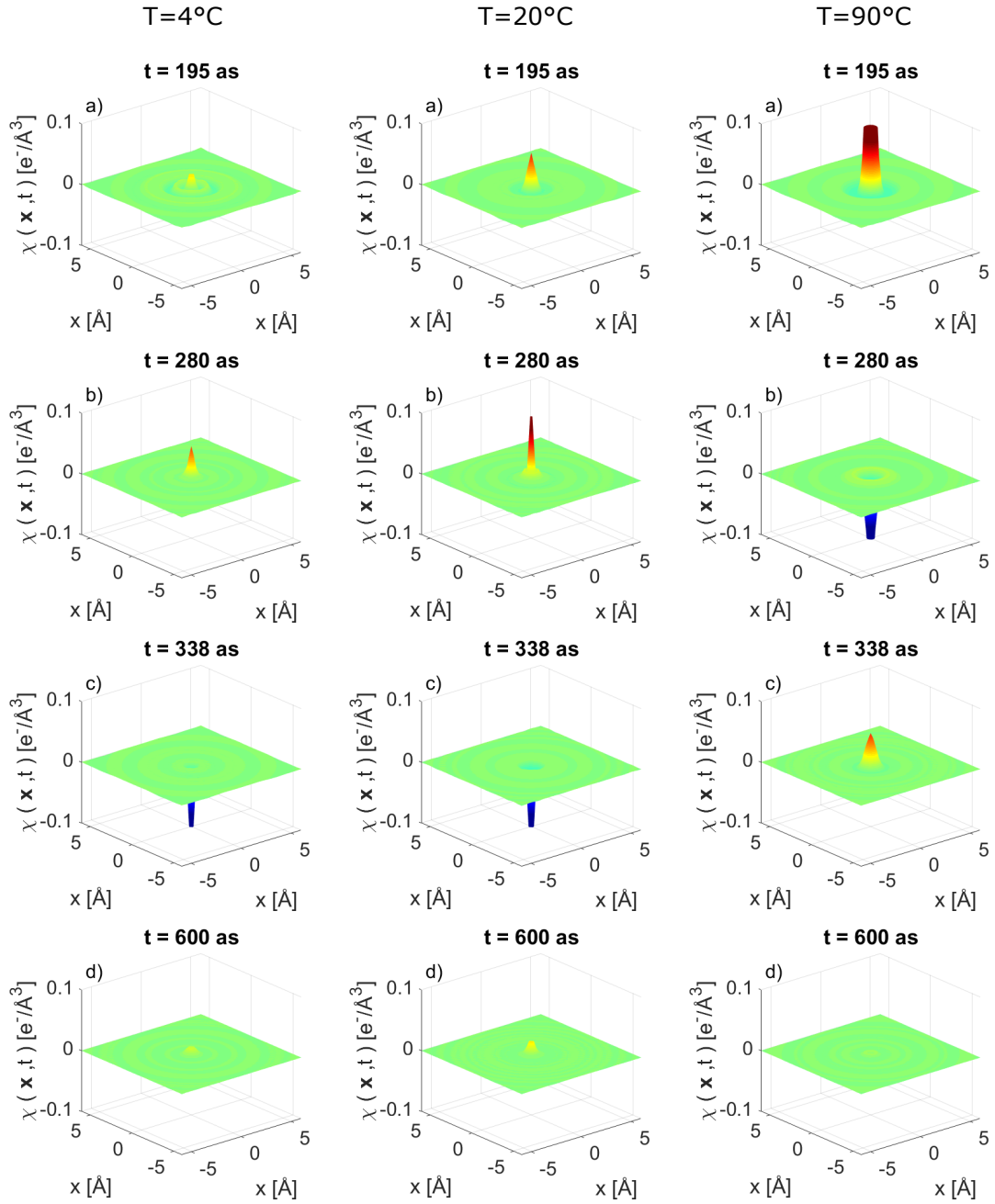
Figure 4.17: Electron density disturbance evolution in water for 4 °C (left), 20 °C (middle) and 90 °C (right) at following time points: a) 195 as, b) 280 as, c) 338 as and d) 600 as.

equal for all temperatures within the available range of time resolution (0.82 as). With proceeding time, the amplitude of $\chi(\mathbf{x},t)$ oscillates, reaching a state of complete relaxa-
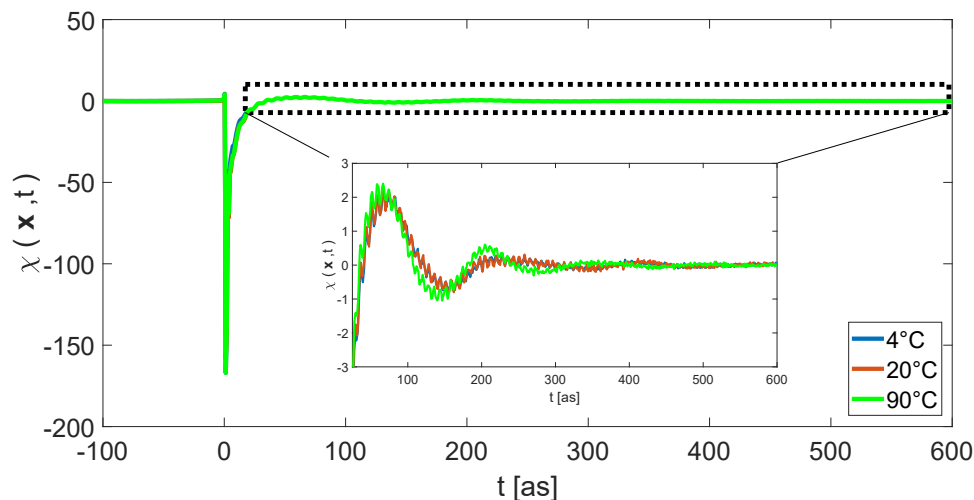
Figure 4.18: The amplitude of $\chi(\mathbf{x},t)$ is shown at the point of interaction as a function of time for all three temperatures. The inset is a zoom of the figure for smaller amplitude values.

tion around 600 as. However, differences as a function of temperature occur during these oscillations of $\chi(\mathbf{x},t)$ (see inset in figure 4.18). Already the second local maximum of $\chi(\mathbf{x},t)$ is at slightly different time points for each temperature, occurring first at 90 °C at 62±5 as, followed by 20 °C at 67±5 as and 4 °C at 75±5 as. In the following, the electron density disturbance evolution at 90 °C develops faster than at 20 °C and 4 °C, that have almost the same evolution velocity, resulting in an earlier time point of the emission of the second electron density disturbance maximum at 90 °C (at 107±5 as) compared to 20 °C and 4 °C (at 118±5 as). The third local maximum of the amplitude of $\chi(\mathbf{x},t)$ at the point of interaction at 90 °C occurs at 205±5 as, where at 20 °C and 4 °C the amplitude of $\chi(\mathbf{x},t)$ is almost zero. From this time point, the evolution of the amplitude of $\chi(\mathbf{x},t)$ has shifted by half a phase at 90 °C, resulting in an inverted amplitude compared to 20 °C and 4 °C. At time points, when at 20 °C and 4 °C a local maximum in the amplitude of $\chi(\mathbf{x},t)$ occurs, there is a local minimum at 90 °C and vice versa until the oscillation of the amplitude of $\chi(\mathbf{x},t)$ fades out. Differences in the evolution might be explained by different densities of water at investigated temperatures. The density of water is equal to $1\,\mathrm{g/cm^3}$ at 4 °C, which is the highest possible electron density of liquid water, leading to water molecules being located as closely as possible to each other. Hence, at this temperature, the evolution of an electron density disturbance may be suppressed by neighboring molecules as strong as possible in liquid water. At 20 °C, the density has still a value of $0.998\,\mathrm{g/cm^3}$, resulting in an almost equal suppression of the electron density disturbance, while at 90 °C the density is already reduced to $0.965\,\mathrm{g/cm^3}$. Here, compared to water at 4 °C, the electron density disturbance wave may propagate more freely due to less electron density caused by the surrounding atoms.

Next, the propagation of the first maximum of the electron density disturbance wave in space and time as a function of temperature is investigated. Therefore, the temporal evolution of the electron density disturbance is shown for different distances from the point of interaction for all three temperatures in figure 4.19.
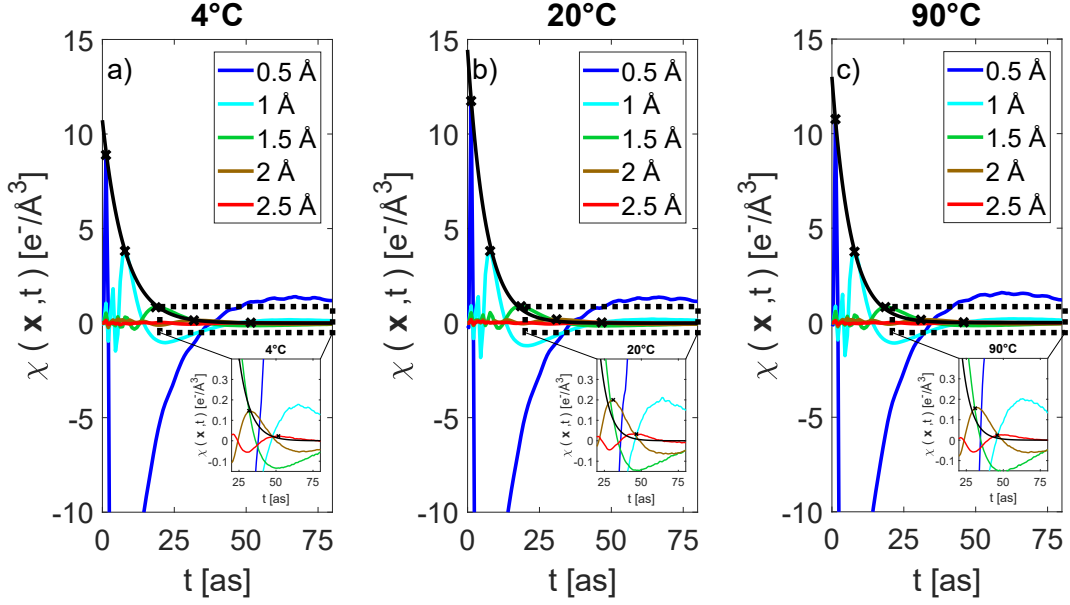
Figure 4.19: The temporal evolution of $\chi(\mathbf{x},t)$ is shown for different distances from the point of interaction for $4\,^\circ\mathrm{C}$ (a)), $20\,^\circ\mathrm{C}$ (b)) and $90\,^\circ\mathrm{C}$ (c)) with the zoom on time points above 20 as as inset. The black markers represent the local maxima of the electron density disturbance wave, describing its evolution in space and time, while the black lines represent an exponential fit of the local maxima points.

Figure 4.19 demonstrates the evolution of the first maximum of the electron density disturbance wave for all three temperatures, showing only small deviations in the evolution of it in time and space as a function of temperature. The amplitude of the first maximum of the electron density disturbance wave is represented by black markers in figure 4.19, showing its exponential decrease as a function of time. An exponential fit to the data via

$$\chi(\mathbf{x},t) = \chi_t e^{-t/\tau_t} \qquad (4.24)$$

is also shown in figure 4.19 as black line to calculate the temporal dampening exponent of the first maximum of the electron density disturbance wave τ_t. Here, χ_t denotes the amplitude of $\chi(\mathbf{x},t)$ at $t = 0$ as. This value is fitted together with τ_t, but was kept at almost equal values for all temperatures. The fitted temporal exponential dampening of the first maximum of the electron density disturbance wave is also plotted for all temperatures together in figure 4.20 a), where the colored lines correspond to the black lines in figure 4.19 a)-c). The evolution of the exponential dampening is almost equal for all temperatures. However, on small time scales the amplitude of $\chi(\mathbf{x},t)$ is equal

93

at 4 °C and 90 °C, being a bit higher at 20 °C, while in the time region beyond 20 as the amplitudes of $\chi(\mathbf{x},\mathrm{t})$ at 20 °C and 90 °C become similar, while the amplitude of $\chi(\mathbf{x},\mathrm{t})$ at 4 °C is slightly above those of the other temperatures. As expected, the values for τ_t differ only slightly for each temperature. However, with 7.7±0.1 as at 4 °C the dampening exponent is higher compared to 6.3±0.1 as at 20 °C and 6.4±0.1 as at 90 °C, which means that the evolution of the first maximum of the electron density disturbance wave is more strongly suppressed at 20 °C and 90 °C.
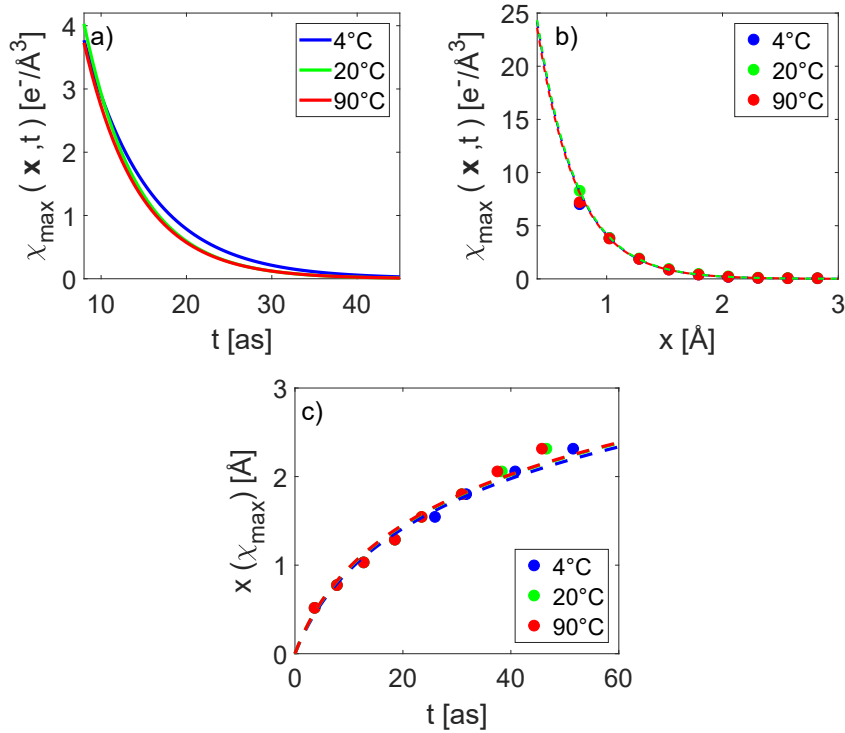
Figure 4.20: The evolution of the exponential dampening of the first maximum of the electron density disturbance wave is shown for all three temperatures as a function of time a) and space b). The colored lines in a) correspond to the black lines in figure 4.19 for all three temperatures. c) Positions of the local maxima of the electron density disturbance wave at different distances from the point of interaction are presented as a function of time for all three temperatures. The dotted lines represent a logarithmic fit to the data to calculate the lifetime of the first electron density disturbance wave.

It is further possible to calculate the evolution of the first maximum of the electron density disturbance wave in space, which is presented in figure 4.20 b) for all three temperatures. Comparably to the evolution of the first maximum of the electron density disturbance wave in time, in this case an exponential decrease for all three temperatures is also observable. However, differences occur only on short distances. A dampening coefficient can be calculated by fitting an exponential function to the data, which is

adapted by

$$\chi\left(\mathbf{x},\mathrm{t}\right) = \chi_x e^{-x/\tau_x} \tag{4.25}$$

with χ_x as the amplitude of $\chi\left(\mathbf{x},\mathrm{t}\right)$ at $x = 0\,\text{Å}$ and the spatial dampening coefficient τ_x. For all temperatures, the spatial dampening coefficient is equal to $0.34\pm0.01\,\text{Å}$, which means that there are no differences in the dampening of the first maximum of the electron density disturbance wave in space.

Finally, other properties of the first maximum of the electron density disturbance wave, like its lifetime or mean velocity, are calculated. Therefore, in figure 4.20 c), the positions of the local maxima of the electron density disturbance wave at different distances from the point of interaction are shown as a function of time for all three temperatures. With a logarithmic fit via

$$x\left(t\right) = log\left(\frac{t}{\tau} + 1\right), \tag{4.26}$$

the lifetime τ of the first maximum of the electron density disturbance wave can be calculated to $6.43\pm0.1\,\mathrm{as}$ at $4\,^{\circ}\mathrm{C}$, $6.13\pm0.1\,\mathrm{as}$ at $20\,^{\circ}\mathrm{C}$ and $6.09\pm0.1\,\mathrm{as}$ at $90\,^{\circ}\mathrm{C}$. Moreover, the mean velocity of the first maximum of the electron density disturbance wave during the first $2.3\,\text{Å}$ is calculated to $0.0448\,\text{Å}/\mathrm{as}$ at $4\,^{\circ}\mathrm{C}$, $0.0495\,\text{Å}/\mathrm{as}$ at $20\,^{\circ}\mathrm{C}$ and $0.0504\,\text{Å}/\mathrm{as}$ at $90\,^{\circ}\mathrm{C}$, resulting in the fastest evolution of the first maximum of the electron density disturbance wave at $90\,^{\circ}\mathrm{C}$. Compared to the speed of light c, this is equal to $0.0149\,c$ at $4\,^{\circ}\mathrm{C}$, $0.0165\,c$ at $20\,^{\circ}\mathrm{C}$ and $0.0168\,c$ at $90\,^{\circ}\mathrm{C}$

4.4 Conclusions

In this chapter, a complete study on the evolution of the electron density disturbance in water on attosecond time scales by means of IXS is presented for water temperatures of $4\,^{\circ}\mathrm{C}$, $20\,^{\circ}\mathrm{C}$ and $90\,^{\circ}\mathrm{C}$. For this purpose, a setup was implemented to perform such experiments at the Taiwan inelastic X-ray scatting beamline BL12XU at SPring-8. This study contains a detailed analysis of the temporal behavior of the propagator $\chi\left(\mathbf{x},\mathrm{t}\right)$ at the point of interaction between the X-rays and water's electrons as well as the evolution of the first electron density disturbance wave front in space and time for all three temperatures, accompanied by 3D snapshots of the spatial evolution of the electron density disturbance in water at selected time points.

Several steps in data analysis were necessary to extract the propagator $\chi\left(\mathbf{x},\mathrm{t}\right)$ from the raw data and imaging the electron density disturbances. The data treatment and application of correction factors were described in detail. Subsequently, the procedure to extract $\chi\left(\mathbf{x},\mathrm{t}\right)$ by calculating the imaginary part of $\chi\left(\mathbf{k},\omega\right)$ from the dynamic structure factor and applying two Fourier transformations is presented. Moreover, a study on the effect of momentum and energy transfer ranges on $\chi\left(\mathbf{x},\mathrm{t}\right)$ was shown due to the fact that the final results of $\chi\left(\mathbf{x},\mathrm{t}\right)$ depend on the investigated momentum and energy transfer ranges. Thus, compared to the study presented by Abbamonte et al. [114], it was possible to investigate the evolution of the electron density disturbance in time and

space more precisely with a better resolution in time (0.82 as) and space (0.26 Å). Finally, 3D snapshots of $\chi(\mathbf{x},t)$ were presented for certain time points and the evolution of $\chi(\mathbf{x},t)$ for all three temperatures was discussed. Therefore, first the temporal behavior of the propagator $\chi(\mathbf{x},t)$ at the point of interaction between the X-rays and water's electrons was investigated with the result that dynamics occur on faster time scales at 90 °C compared to 4 °C and 20 °C, where the evolution of $\chi(\mathbf{x},t)$ is almost equal. This result can be explained by changes in water's density as a function of temperature. Due to the fact that water has the highest density at 4 °C, with a comparable density at 20 °C, the evolution of the electron density disturbance is suppressed by surrounding molecules in a similar way. At 90 °C, the density of water is significantly smaller, leading to less suppression of the evolution of the electron density disturbance.

Furthermore, the evolution of the first maximum of the electron density disturbance wave in space and time was analyzed for all three temperatures. Even though the evolution of the first maximum of the electron density disturbance is almost equal for all temperatures, small deviations could be determined. Whereas the evolution of the maximum of the first electron density disturbance wave in space is almost completely equal for all three temperatures, it is suppressed the strongest at 4 °C in time. With the calculation of the dampening coefficient in space and time, as well as the lifetime of the electron density disturbance wave and its mean velocity, the description of the evolution of the first maximum of the electron density disturbance wave was completed.

Chapter 5

Summary and Outlook

In this thesis three different studies on water and aqueous solutions were presented. Two of these studies were investigating adsorption processes at solid-liquid interfaces by means of XRR, while the third study probed electron density disturbances in water on attosecond time scales by means of IXS.

First, a complete description on the lysozyme adsorption on the hydrophilic surface of titanium oxide coated on a silicon wafer as a function of temperature, pH value, titanium oxide layer thickness and pressure was presented. This were the first successful performed XRR experiments on a titanium oxide surface revealing the information that the adsorbed amount of lysozyme on titanium oxide differs from that of lysozyme on silicon oxide both at same thermodynamic conditions and at same electrostatic conditions (modulated by pH value variation). These results confirm that the adsorption process of lysozyme is not only depending on surface charge differences, but depends strongly on the interface it adsorbs on. The calculation of the Hamaker constant leads to the conclusion that the silicon substrate appears to be repulsive, which results in a reduced adsorption of lysozyme at thin titanium oxide layers. These results were verified by measurements of lysozyme adsorption on titanium oxide as a function of titanium oxide layer thickness. Moreover, pressure-dependent measurements revealed a desorption of lysozyme from titanium oxide with rising pressures, being almost reversible by releasing pressure. Hence, it is indicated that under hydrostatic pressure lysozyme prefers to be fully hydrated in solution instead of having a defective hydration shell, which would result in an increased amount of lysozyme at the titanium oxide surface.

This description of the adsorption behavior of lysozyme was performed at a lysozyme concentration of 1 mg/mL to be comparable to the study of lysozyme adsorbing on silicon oxide [74]. However, investigating the adsorption behavior of differently concentrated lysozyme solutions may provide new insight into the adsorption behavior. Furthermore, titanium oxide is a reactive material that alters its biocompatibility by UV-light irradiation [253]. Hence, investigating the adsorption behavior of lysozyme on titanium oxide under UV-light irradiation should also be considered as an future project due to its importance for technical applications [254].

The second study of this thesis dealt with the adsorption behavior of ions on the hydrophobic surface of an with OTS coated silicon wafer. The adsorption of different alkali metal halogens as well as alkali metal hydroxides provided information on the adsorption process of ions at this hydrophobic interface as a function of ion size and concentration. First, the adsorption pathway of the solved ions was determined. Thereafter, under cation variation of alkali metal halogens, concentration-dependent measurements revealed the higher ability of small ions to straighten up the tail groups of the OTS layer compared to larger ions, which includes the information that the OTS molecules are not completely straight perpendicular to the surface plane before ion addition. Furthermore, the shape of the adsorbed ion layer on top of the hydrophobic gap varies with ion size. Large ions produce an adsorbed layer that is thinner but has a higher electron density compared to small ions. These results were confirmed upon anion variation of alkali halogens. However, changing the anion to hydroxide resulted in differences in the electron density profiles compared to alkali metal halogens. In the case of hydroxides significantly less ions adsorbed in-between the OTS tail groups, being still able to straighten up the OTS tail groups to full length perpendicular to the surface plane. Moreover, hydroxides induced strong changes in the shape of the hydrophobic gap. At high concentrated alkali metal hydroxide solutions, the ions even seem to adsorb directly on top of the OTS tail group, overcoming the hydrophobic gap. However, these results of alkali metal hydroxide adsorption on OTS have to be interpreted with caution since the addition of this aqueous solution on OTS directly leads to a chemical reaction resulting in bubble formation inside the sample cell.

Even though this study reveals new insight into ion adsorption processes at the hydrophobic surface of OTS, further measurements of higher concentrated ion solutions as well as other ion types would complete the knowledge of this processes. The use of $CaCl_2$ would probe a cation that is more chaotropic than other studied cations, while the investigation of the adsorption behavior of ionic liquids would probe larger ions with regards to the possibility to adsorb in-between the OTS tail groups.

Finally, the evolution of electron density disturbances in water was investigated on ultrashort time scales (with a resolution of 0.82 as) with sub-angstrom resolution (0.26 Å) for water temperatures of 4 °C, 20 °C and 90 °C. This study extended an earlier study presented by Abbamonte et al. [114] and provided new insight into the density disturbance evolution in water on ultrashort time scales due to the significantly improved time and space resolution. The necessity of increasing the resolution in time and space was shown by calculating differences in the final results by variation of the momentum and energy transfer range. Moreover, the comparison of two additional temperatures revealed differences in the electron density evolution of water as a function of temperature. There is a phase shift in the oscillation of the electron density at 90 °C compared to 4 °C and 20 °C at time points beyond 200 as after the interaction, which is suggested to originate by differences in the density of water. However, significant differences are not observable on shorter time ranges, as was shown for the evolution of the first maximum of the electron density disturbance for all three temperatures.

Hence, investigating the evolution of the electron density disturbance in water with different densities (e.g. by a further increase of the temperature of water going in hand

with an increase in the pressure of water) may provide new insights into this research field. Furthermore, also the investigation of the evolution of the electron density disturbance in aqueous solutions would be of high interest.

List of Figures

List of Tables

Bibliography

[1] M. Chaplin. Water: a Brief Early History of its Science. 2018-08-31, http://www1.lsbu.ac.uk/water/water.html.

[2] I. Tuñón, M. T. C. Martins-Costa, C. Millot, and M. F. Ruiz-López. Molecular dynamics simulations of elementary chemical processes in liquid water using combined density functional and molecular mechanics potentials. i. proton transfer in strongly h-bonded complexes. *The Journal of chemical physics*, 106(9):3633–3642, 1997.

[3] C.-J. Li and L. Chen. Organic chemistry in water. *Chemical Society Reviews*, 35(1):68–82, 2006.

[4] J. D. Barrow, R. M. Lynden-Bell, S. C. Morris, J. L. Finney, and C. Harper. *Water and life: The unique properties of H2O*. CRC Press, 2010.

[5] M. Henry. The state of water in living systems: from the liquid to the jellyfish. *Cellular and molecular biology (Noisy-le-Grand, France)*, 51(7):677–702, 2005.

[6] H. Cavendish. Xix. three papers, containing experiments on factitious air. *Philosophical Transactions*, 56:141–184, 1766.

[7] A. Avogadro. Essay on a manner of determining the relative masses of the elementary molecules of bodies, and the proportions in which they enter into these compounds. *Journal de physique*, 73:58–76, 1811.

[8] S. Arrhenius. Über die dissociation der in wasser gelösten stoffe. *Zeitschrift für physikalische Chemie*, 1(1):631–648, 1887.

[9] H. Tanaka. Simple physical explanation of the unusual thermodynamic behavior of liquid water. *Physical review letters*, 80(26):5750, 1998.

[10] R. C. Dougherty and L. N. Howard. Equilibrium structural model of liquid water: evidence from heat capacity, spectra, density, and other properties. *The Journal of chemical physics*, 109(17):7379–7393, 1998.

[11] G. S. Kell. Density, thermal expansivity, and compressibility of liquid water from 0. deg. to 150. deg.. correlations and tables for atmospheric pressure and saturation reviewed and expressed on 1968 temperature scale. *Journal of Chemical and Engineering Data*, 20(1):97–105, 1975.

[12] I. Brovchenko and A. Oleinikova. Multiple Phases of Liquid Water. *ChemPhysChem*, 9(18):2660–2675, 2008.

[13] L. G. M. Pettersson, R. H. Henchman, and A. Nilsson. Water - the most anomalous liquid, 2016.

[14] P. Gallo, K. Amann-Winkel, C. A. Angell, M. A. Anisimov, F. Caupin, C. Chakravarty, E. Lascaris, T. Loerting, A. Z. Panagiotopoulos, J. Russo, J. A. Sellberg, H. E. Stanley, H. Tanaka, C. Vega, L. Xu, and L. G. M. Pettersson. Water: A tale of two liquids. *Chemical reviews*, 116(13):7463–7500, 2016.

[15] E. A. Jagla. The interpretation of water anomalies in terms of core-softened models. *Brazilian journal of physics*, 34(1):17–23, 2004.

[16] J. R. Errington and P. G. Debenedetti. Relationship between structural order and the anomalies of liquid water. *Nature*, 409(6818):318, 2001.

[17] A. Nilsson and L. G. M. Pettersson. The structural origin of anomalous properties of liquid water. *Nature communications*, 6:8998, 2015.

[18] K. Stokely, M. G. Mazza, H. E. Stanley, and G. Franzese. Effect of hydrogen bond cooperativity on the behavior of water. *Proceedings of the National Academy of Sciences*, 107(4):1301–1306, 2010.

[19] P. Ball. Water: water-an enduring mystery. *Nature*, 452(7185):291, 2008.

[20] M. S. Shell, P. G. Debenedetti, and A. Z. Panagiotopoulos. Molecular structural order and anomalies in liquid silica. *Physical Review E*, 66(1):011202, 2002.

[21] W. Hujo, B. S. Jabes, V. K. Rana, C. Chakravarty, and V. Molinero. The rise and fall of anomalies in tetrahedral liquids. *Journal of Statistical Physics*, 145(2):293–312, 2011.

[22] B. S. Jabes, D. Nayar, D. Dhabal, V. Molinero, and C. Chakravarty. Water and other tetrahedral liquids: order, anomalies and solvation. *Journal of Physics: Condensed Matter*, 24(28):284116, 2012.

[23] F. Smallenburg, L. Filion, and F. Sciortino. Erasing no-man's land by thermodynamically stabilizing the liquid-liquid transition in tetrahedral particles. *Nature physics*, 10(9):653, 2014.

[24] F. Perakis, K. Amann-Winkel, F. Lehmkühler, M. Sprung, D. Mariedahl, J. A. Sellberg, H. Pathak, A. Späh, F. Cavalca, D. Schlesinger, A. Ricci, A. Jain, B. Massani, F. Aubree, C. J. Benmore, T. Loerting, G. Grübel, L. G. M. Pettersson, and A. Nilsson. Diffusive dynamics during the high-to-low density transition in amorphous ice. *Proceedings of the National Academy of Sciences*, 114(31):8193–8198, 2017.

[25] Y. Shinohara, W. Dmowski, T. Iwashita, B. Wu, D. Ishikawa, A. Q. R. Baron, and T. Egami. Viscosity and real-space molecular motion of water: Observation with inelastic x-ray scattering. *Physical Review E*, 98(2):022604, 2018.

[26] A. K. Soper. Structural transformations in amorphous ice and supercooled water and their relevance to the phase diagram of water. *Molecular Physics*, 106(16-18):2053–2076, 2008.

[27] F. Lehmkühler, Y. Forov, T. Büning, Ch. J. Sahle, I. Steinke, K. Julius, Th. Buslaps, M. Tolan, M. Hakala, and C. Sternemann. Intramolecular structure and energetics in supercooled water down to 255 k. *Physical Chemistry Chemical Physics*, 18(9):6925–6930, 2016.

[28] P. Ball and J. E. Hallsworth. Water structure and chaotropicity: their uses, abuses and biological implications. *Physical Chemistry Chemical Physics*, 17(13):8297–8305, 2015.

[29] J. A. Sellberg, C. Huang, T. A. McQueen, N. D. Loh, H. Laksmono, D. Schlesinger, R. G. Sierra, D. Nordlund, C. Y. Hampton, D. Starodub, D. P. DePonte, M. Beye, C. Chen, A. V. Martin, A. Barty, K. T. Wikfeldt, T. M. Weiss, C. Caronna, J. Feldkamp, L. B. Skinner, M. M. Seibert, M. Messerschmidt, G. J. Williams, S. Boutet, L. G. M. Pettersson, M. J. Bogan, and A. Nilsson. Ultrafast X-ray probing of water structure below the homogeneous ice nucleation temperature. *Nature*, 510(7505):381–384, 2014.

[30] E. Duboué-Dijon and D. Laage. Characterization of the local structure in liquid water by various order parameters. *The Journal of Physical Chemistry B*, 119(26):8406–8418, 2015.

[31] P. G. Debenedetti, M. A. Ricci, and F. Bruni. *Water: Fundamentals as the Basis for Understanding the Environment and Promoting Technology*, volume 187. IOS Press, 2015.

[32] A. Nilsson, D. Schlesinger, and L. G. M. Pettersson. X-ray and simulation studies of water (*). *RIVISTA DEL NUOVO CIMENTO*, 39(5):225–278, 2016.

[33] D. Eisenberg and A. D. McLachlan. Solvation energy in protein folding and binding. *Nature*, 319(6050):199, 1986.

[34] A. V. Marenich, C. J. Cramer, and D. G. Truhlar. Universal solvation model based on solute electron density and on a continuum model of the solvent defined by the bulk dielectric constant and atomic surface tensions. *The Journal of Physical Chemistry B*, 113(18):6378–6396, 2009.

[35] K. Mathew, R. Sundararaman, K. Letchworth-Weaver, T. A. Arias, and R. G. Hennig. Implicit solvation model for density-functional study of nanocrystal surfaces and reaction pathways. *The Journal of chemical physics*, 140(8):084106, 2014.

[36] P. Ball. Water as an Active Constituent in Cell Biology. *Chemical Reviews*, 108(1):74–108, 2008.

[37] W. C. Still, A. Tempczyk, R. C. Hawley, and T. Hendrickson. Semianalytical treatment of solvation for molecular mechanics and dynamics. *Journal of the American Chemical Society*, 112(16):6127–6129, 1990.

[38] I. Brovchenko and A. Oleinikova. Which properties of a spanning network of hydration water enable biological functions? *ChemPhysChem*, 9(18):2695–2702, 2008.

[39] M. Boudart. *Kinetics of Chemical Processes: Butterworth-Heinemann Series in Chemical Engineering*. Elsevier, 2014.

[40] P. Fenter and N. C. Sturchio. Mineral-water interfacial structures revealed by synchrotron x-ray scattering. *Progress in Surface Science*, 77(5-8):171–258, 2004.

[41] P. Fenter and S. S. Lee. Hydration layer structure at solid-water interfaces. *MRS Bulletin*, 39(12):1056–1061, 2014.

[42] F. E. G. Güner, J. Wåhlin, M. Hinge, and S. Kjelstrup. The temperature jump at a growing ice-water interface. *Chemical Physics Letters*, 622:15–19, 2015.

[43] J. Israelachvili. *Intermolecular and surface forces*. Academic press, 2011.

[44] G. B. Kaggwa, P. C. Nalam, J. I. Kilpatrick, N. D. Spencer, and S. P. Jarvis. Impact of hydrophilic/hydrophobic surface chemistry on hydration forces in the absence of confinement. *Langmuir*, 28(16):6589–6594, 2012.

[45] W. D. Kaplan and Y. Kauffmann. Structural order in liquids induced by interfaces with crystals. *Annu. Rev. Mater. Res.*, 36:1–48, 2006.

[46] J. Janeček and R. R. Netz. Interfacial water at hydrophobic and hydrophilic surfaces: Depletion versus adsorption. *Langmuir*, 23(16):8417–8429, 2007.

[47] A. K. Doerr, M. Tolan, J.-P. Schlomka, and W. Press. Evidence for density anomalies of liquids at the solid/liquid interface. *EPL (Europhysics Letters)*, 52(3):330, 2000.

[48] M. Mezger, H. Reichert, S. Schöder, J. Okasinski, H. Schröder, H. Dosch, D. Palms, J. Ralston, and V. Honkimäki. High-resolution in situ x-ray study of the hydrophobic gap at the water–octadecyl-trichlorosilane interface. *Proceedings of the National Academy of Sciences*, 103(49):18401–18404, 2006.

[49] M. Mezger, F. Sedlmeier, D. Horinek, H. Reichert, D. Pontoni, and H. Dosch. On the origin of the hydrophobic water gap: An x-ray reflectivity and md simulation study. *Journal of the American Chemical Society*, 132(19):6735–6741, 2010.

[50] S. I. Mamatkulov, P. K. Khabibullaev, and R. R. Netz. Water at hydrophobic substrates: curvature, pressure, and temperature effects. *Langmuir*, 20(11):4756–4763, 2004.

[51] H. Xie, S. Vucetic, L. M. Iakoucheva, C. J. Oldfield, A. K. Dunker, V. N. Uversky, and Z. Obradovic. Functional anthology of intrinsic disorder. 1. biological processes and functions of proteins with long disordered regions. *Journal of proteome research*, 6(5):1882–1898, 2007.

[52] T. Hsu, M. Trojanowska, and D. K. Watson. Ets proteins in biological control and cancer. *Journal of cellular biochemistry*, 91(5):896–903, 2004.

[53] I. Garrn, C. Reetz, N. Brandes, L. W. Kroh, and H. Schubert. Clot-forming: the use of proteins as binders for producing ceramic foams. *Journal of the European Ceramic Society*, 24(3):579–587, 2004.

[54] I. Yosef, M. G. Goren, and U. Qimron. Proteins and dna elements essential for the crispr adaptation process in escherichia coli. *Nucleic acids research*, 40(12):5569–5576, 2012.

[55] J. Strotmann, O. Levai, J. Fleischer, K. Schwarzenbacher, and H. Breer. Olfactory receptor proteins in axonal processes of chemosensory neurons. *Journal of Neuroscience*, 24(35):7754–7761, 2004.

[56] B. Kasemo. Biological surface science. *Surface science*, 500(1-3):656–677, 2002.

[57] C. Czeslik. Factors ruling protein adsorption. *Zeitschrift für physikalische Chemie*, 218(7):771–801, 2004.

[58] W. Norde. Adsorption of proteins from solution at the solid-liquid interface. *Advances in colloid and interface science*, 25:267–340, 1986.

[59] M. Kieliszek and A. Misiewicz. Microbial transglutaminase and its application in the food industry. a review. *Folia Microbiologica*, 16(9):715–725, 2014.

[60] C. Kuraishi, K. Yamazaki, and Y. Susa. Transglutaminase: its utilization in the food industry. *Food Reviews International*, 17(2):221–246, 2001.

[61] K. S. Soppimath, T. M. Aminabhavi, A. R. Kulkarni, and W. E. Rudzinski. Biodegradable polymeric nanoparticles as drug delivery devices. *Journal of controlled release*, 70(1-2):1–20, 2001.

[62] S. V. Wegner, A. Okesli, P. Chen, and C. He. Design of an emission ratiometric biosensor from merr family proteins: a sensitive and selective sensor for hg2+. *Journal of the American Chemical Society*, 129(12):3474–3475, 2007.

[63] C. Czeslik. Proteinadsorption an festen grenzflächen. erwünscht und unerwünscht. *Chemie in unserer Zeit*, 40(4):238–245, 2006.

[64] H. Hosseinkhani, P.-D. Hong, and D.-S. Yu. Self-assembled proteins and peptides for regenerative medicine. *Chemical Reviews*, 113(7):4837–4861, 2013.

[65] P. S. Stewart and J. W. Costerton. Antibiotic resistance of bacteria in biofilms. *The lancet*, 358(9276):135–138, 2001.

[66] J. D. Bryers. Medical biofilms. *Biotechnology and bioengineering*, 100(1):1–18, 2008.

[67] L. Le Guéhennec, A. Soueidan, P. Layrolle, and Y. Amouriq. Surface treatments of titanium dental implants for rapid osseointegration. *Dental materials*, 23(7):844–854, 2007.

[68] M. Rabe, D. Verdes, and S. Seeger. Understanding protein adsorption phenomena at solid surfaces. *Advances in colloid and interface science*, 162(1-2):87–106, 2011.

[69] H. Hähl, F. Evers, S. Grandthyll, M. Paulus, C. Sternemann, P. Loskill, M. Lessel, A. K. Hüsecken, T. Brenner, M. Tolan, and K. Jacobs. Subsurface influence on the structure of protein adsorbates as revealed by in situ x-ray reflectivity. *Langmuir*, 28(20):7747–7756, 2012.

[70] F. Evers, K. Shokuie, M. Paulus, C. Sternemann, C. Czeslik, and M. Tolan. Exploring the interfacial structure of protein adsorbates and the kinetics of protein adsorption: An in situ high-energy x-ray reflectivity study. *Langmuir*, 24(18):10216–10221, 2008.

[71] F. Höök, M. Rodahl, B. Kasemo, and P. Brzezinski. Structural changes in hemoglobin during adsorption to solid surfaces: effects of ph, ionic strength, and ligand binding. *Proceedings of the National Academy of Sciences*, 95(21):12271–12276, 1998.

[72] A. K. Hüsecken, F. Evers, C. Czeslik, and M. Tolan. Effect of urea and glycerol on the adsorption of ribonuclease a at the air- water interface. *Langmuir*, 26(16):13429–13435, 2010.

[73] S. Tiemeyer, M. Paulus, and M. Tolan. Effect of surface charge distribution on the adsorption orientation of proteins to lipid monolayers. *Langmuir*, 26(17):14064–14067, 2010.

[74] I. Kiesel, M. Paulus, J. Nase, S. Tiemeyer, C. Sternemann, K. Rüster, F. J. Wirkert, K. Mende, T. Büning, and M. Tolan. Temperature-driven adsorption and desorption of proteins at solid-liquid interfaces. *Langmuir*, 30(8):2077–2083, 2014.

[75] G. Jackler, R. Steitz, and C. Czeslik. Effect of temperature on the adsorption of lysozyme at the silica/water interface studied by optical and neutron reflectometry. *Langmuir*, 18(17):6565–6570, 2002.

[76] B. Nowak, M. Paulus, J. Nase, P. Salmen, P. Degen, F. J. Wirkert, V. Honkimäki, and M. Tolan. Solid-supported lipid multilayers under high hydrostatic pressure. *Langmuir*, 32(11):2638–2643, 2016.

[77] S. Dogan, M. Paulus, Y. Forov, C. Weis, M. Kampmann, C. Cewe, I. Kiesel, P. Degen, P. Salmen, H. Rehage, and M. Tolan. Human apolipoprotein a1 at solid/liquid and liquid/gas interfaces. *The Journal of Physical Chemistry B*, 122(14):3953–3960, 2018.

[78] P. Salmen. *Röntgenreflektometrie an der hydrophoben Festkörper-Flüssigkeits-Grenzäche*. PhD thesis, Technische Universität Dortmund, 2017.

[79] F. Höök, J. Vörös, M. Rodahl, R. Kurrat, P. Böni, J. J. Ramsden, M. Textor, N. D. Spencer, P. Tengvall, J. Gold, and B. Kasemo. A comparative study of protein adsorption on titanium oxide surfaces using in situ ellipsometry, optical waveguide lightmode spectroscopy, and quartz crystal microbalance/dissipation. *Colloids and Surfaces B: Biointerfaces*, 24(2):155–170, 2002.

[80] M. Lehnert, M. Gorbahn, C. Rosin, M. Klein, I. Köper, B. Al-Nawas, W. Knoll, and M. Veith. Adsorption and conformation behavior of biotinylated fibronectin on streptavidin-modified tiox surfaces studied by spr and afm. *Langmuir*, 27(12):7743–7751, 2011.

[81] C. A. Siedlecki and R. E. Marchant. Atomic force microscopy for characterization of the biomaterial interface. *Biomaterials*, 19(4-5):441–454, 1998.

[82] I. M. Tucker, J. T. Petkov, J. Penfold, R. K. Thomas, A. R. Cox, and N. Hedges. Adsorption of hydrophobin/β-casein mixtures at the solid-liquid interface. *Journal of Colloid and Interface Science*, 478(Supplement C):81–87, 2016.

[83] A. G. Richter and I. Kuzmenko. Using in situ x-ray reflectivity to study protein adsorption on hydrophilic and hydrophobic surfaces: Benefits and limitations. *Langmuir*, 29(17):5167–5180, 2013.

[84] V. Jakobi, P. Salmen, M. Paulus, M. Tolan, and A. Rosenhahn. Compositional fingerprint of soy sauces via hydrophobic surface interaction. *Food Chemistry*, 218(Supplement C):256 – 260, 2017.

[85] S. M. George. Atomic layer deposition: An overview. *Chemical Reviews*, 110(1):111–131, 2010.

[86] S. Trost, K. Zilberberg, A. Behrendt, A. Polywka, P. Görrn, P. Reckers, J. Maibach, T. Mayer, and T. Riedl. Overcoming the "light-soaking" issue in inverted organic solar cells by the use of al:zno electron extraction layers. *Advanced Energy Materials*, 3(11):1437–1444, 2013.

[87] D. P. Macwan, P. N. Dave, and S. Chaturvedi. A review on nano-tio2 sol-gel type syntheses and its applications. *Journal of Materials Science*, 46(11):3669–3686, 2011.

[88] S. P. Albu, A. Ghicov, J. M. Macak, R. Hahn, and P. Schmuki. Self-organized, free-standing tio2 nanotube membrane for flow-through photocatalytic applications. *Nano Letters*, 7(5):1286–1289, 2007.

[89] R. Adell, U Lekholm, B. Rockler, and P.-I. Brånemark. A 15-year study of osseointegrated implants in the treatment of the edentulous jaw. *International Journal of Oral Surgery*, 10(6):387 – 416, 1981.

[90] M. Quirynen, B. Al-Nawas, H. J. A. Meijer, A. Razavi, T. E. Reichert, M. Schimmel, S. Storelli, E. Romeo, and the Roxolid Study Group. Small-diameter titanium grade iv and titanium-zirconium implants in edentulous mandibles: three-year results from a double-blind, randomized controlled trial. *Clinical Oral Implants Research*, 26(7):831–840, 2015.

[91] Y. Forov, M. Paulus, S. Dogan, P. Salmen, C. Weis, T. Gahlmann, A. Behrendt, C. Albers, M. Elbers, W. Schnettger, S. Egger, E. Zwar, H. Rehage, I. Kiesel, T. Riedl, and M. Tolan. Adsorption behavior of lysozyme at titanium oxide-water interfaces. *Langmuir*, 34(19):5403–5408, 2018.

[92] D. Chandler. Interfaces and the driving force of hydrophobic assembly. *Nature*, 437(7059):640, 2005.

[93] A. R. Hirst, B. Escuder, J. F. Miravet, and D. K. Smith. High-tech applications of self-assembling supramolecular nanostructured gel-phase materials: from regenerative medicine to electronic devices. *Angewandte Chemie International Edition*, 47(42):8002–8018, 2008.

[94] M. Mrksich and G. M Whitesides. Using self-assembled monolayers to understand the interactions of man-made surfaces with proteins and cells. *Annual review of biophysics and biomolecular structure*, 25(1):55–78, 1996.

[95] X. Wang, J. Zhuang, Q. Peng, and Y. Li. A general strategy for nanocrystal synthesis. *Nature*, 437(7055):121, 2005.

[96] B. Dong, N. Li, L. Zheng, L. Yu, and T. Inoue. Surface adsorption and micelle formation of surface active ionic liquids in aqueous solution. *Langmuir*, 23(8):4178–4182, 2007.

[97] M. Hoernke, B. Koksch, and G. Brezesinski. Influence of the hydrophobic interface and transition metal ions on the conformation of amyloidogenic model peptides. *Biophysical chemistry*, 150(1-3):64–72, 2010.

[98] S. H. Donaldson Jr, A. Røyne, K. Kristiansen, M. V. Rapp, S. Das, M. A. Gebbie, D. Woog Lee, P. Stock, M. Valtiner, and J. Israelachvili. Developing a general interaction potential for hydrophobic and hydrophilic interactions. *Langmuir*, 31(7):2051–2064, 2014.

[99] D. Horinek and R. R. Netz. Specific ion adsorption at hydrophobic solid surfaces. *Physical Review Letters*, 99(22):226104, 2007.

[100] R. Zangi and J. B. F. N. Engberts. Physisorption of hydroxide ions from aqueous solution to a hydrophobic surface. *Journal of the American Chemical Society*, 127(7):2272–2276, 2005.

[101] D. Horinek, A. Herz, L. Vrbka, F. Sedlmeier, S. I. Mamatkulov, and R. R. Netz. Specific ion adsorption at the air/water interface: The role of hydrophobic solvation. *Chemical Physics Letters*, 479(4-6):173–183, 2009.

[102] S. Maolin, Z. Fuchun, W. Guozhong, F. Haiping, W. Chunlei, C. Shimou, Z. Yi, and H. Jun. Ordering layers of [bmim][pf 6] ionic liquid on graphite surfaces: Molecular dynamics simulation. *The Journal of chemical physics*, 128(13):134504, 2008.

[103] S. Ghosal, J. C. Hemminger, H. Bluhm, B. S. Mun, E. L. D. Hebenstreit, G. Ketteler, D. F. Ogletree, F. G. Requejo, and M. Salmeron. Electron spectroscopy of aqueous solution interfaces reveals surface enhancement of halides. *Science*, 307(5709):563–566, 2005.

[104] E. Sloutskin, J. Baumert, B. M. Ocko, I. Kuzmenko, A. Checco, L. Tamam, E. Ofer, T. Gog, O. Gang, and M. Deutsch. The surface structure of concentrated aqueous salt solutions. *The Journal of chemical physics*, 126(5):054704, 2007.

[105] A. Poynor, L. Hong, I. K. Robinson, S. Granick, Z. Zhang, and P. A. Fenter. How water meets a hydrophobic surface. *Phys. Rev. Lett.*, 97:266101, 2006.

[106] A. Uysal, M. Chu, B. Stripe, A. Timalsina, S. Chattopadhyay, C. M. Schlepütz, T. J. Marks, and P. Dutta. What x rays can tell us about the interfacial profile of water near hydrophobic surfaces. *Phys. Rev. B*, 88:035431, 2013.

[107] G. M. Gale, G. Gallot, F. Hache, N. Lascoux, S. Bratos, and J.-Cl. Leicknam. Femtosecond dynamics of hydrogen bonds in liquid water: A real time study. *Physical review letters*, 82(5):1068, 1999.

[108] C. J. Fecko, J. D. Eaves, J. J. Loparo, A. Tokmakoff, and P. L. Geissler. Ultrafast hydrogen-bond dynamics in the infrared spectroscopy of water. *Science*, 301(5640):1698–1702, 2003.

[109] A. Pietzsch, F. Hennies, P. S. Miedema, B. Kennedy, J. Schlappa, T. Schmitt, V. N. Strocov, and A. Föhlisch. Snapshots of the fluctuating hydrogen bond network in liquid water on the sub-femtosecond timescale with vibrational resonant inelastic x-ray scattering. *Physical review letters*, 114(8):088302, 2015.

[110] M. Thämer, L. De Marco, K. Ramasesha, A. Mandal, and A. Tokmakoff. Ultrafast 2d ir spectroscopy of the excess proton in liquid water. *Science*, 350(6256):78–82, 2015.

[111] S. Woutersen, U. Emmerichs, and H. J. Bakker. Femtosecond mid-ir pump-probe spectroscopy of liquid water: Evidence for a two-component structure. *Science*, 278(5338):658–660, 1997.

[112] S. T. Van Der Post, C.-S. Hsieh, M. Okuno, Y. Nagata, H. J. Bakker, M. Bonn, and J. Hunger. Strong frequency dependence of vibrational relaxation in bulk and surface water reveals sub-picosecond structural heterogeneity. *Nature communications*, 6:8384, 2015.

[113] G. Schmid and A. Moshammer, R.and Wolf. *Two-Color Pump-Probe Experiments on Small Quantum Systems at the Free-Electron Laser in Hamburg*. PhD thesis, Ruprecht-Karls-Universität Heidelberg, 2018.

[114] P. Abbamonte, K. D. Finkelstein, M. D. Collins, and S. M. Gruner. Imaging density disturbances in water with a 41.3-attosecond time resolution. *Phys. Rev. Lett.*, 92:237401, 2004.

[115] Ch. J. Sahle, C. Sternemann, C. Schmidt, S. Lehtola, S. Jahn, L. Simonelli, S. Huotari, M. Hakala, T. Pylkkänen, A. Nyrow, K. Mende, M. Tolan, K. Hämäläinen, and M. Wilke. Microscopic structure of water at elevated pressures and temperatures. *Proceedings of the National Academy of Sciences*, page 201220301, 2013.

[116] C. Sternemann and M. Wilke. Spectroscopy of low and intermediate z elements at extreme conditions: in situ studies of earth materials at pressure and temperature via x-ray raman scattering. *High Pressure Research*, 36(3):275–292, 2016.

[117] W. Schülke. *Electron Dynamics Studied by Inelastic (Hard) X-Ray Scattering*. Oxford University Press, 2007.

[118] P. Abbamonte, G. C. L. Wong, D. G. Cahill, J. P. Reed, R. H. Coridan, N. W. Schmidt, G. H. Lai, Y. I. Joe, and D. Casa. Ultrafast imaging and the phase problem for inelastic x-ray scattering. *Advanced Materials*, 22(10):1141–1147, 2010.

[119] J. L. Aparicio and M. P. Elizalde. From water to h2o: Using the human dimension of science to teach the nature of science. *Journal of Chemical Education*, 95(10):1763–1770, 2018.

[120] N. E. Dorsey. Properties of ordinary water-substance in all its phases: Water-vapor, water, and all the ices·, acs monograph 81, 1968.

[121] A. Werner. Ueber haupt-und nebenvalenzen und die constitution der ammoniumverbindungen. *Justus Liebigs Annalen der Chemie*, 322(3):261–296, 1902.

[122] A. Wallqvist and R. D. Mountain. Molecular models of water: Derivation and description. *Reviews in Computational Chemistry*, pages 183–247, 1999.

[123] J. F. Ouyang and R. Bettens. Modelling water: a lifetime enigma. *CHIMIA International Journal for Chemistry*, 69(3):104–111, 2015.

[124] P. Lo Nostro and B. Ninham. *Aqua Incognita: Why ice floats on water and Galileo 400 years on.* Connor Court Publishing, 2014.

[125] O. Björneholm, M. H. Hansen, A. Hodgson, L.-M. Liu, D. T. Limmer, A. Michaelides, P. Pedevilla, J. Rossmeisl, H. Shen, G. Tocci, E. Tyrode, M.-M. Walz, J. Werner, and H. Bluhm. Water at interfaces. *Chemical reviews*, 116(13):7698–7726, 2016.

[126] V. M. Gun'ko, V. V. Turov, V. M. Bogatyrev, V. I. Zarko, R. Leboda, E. V. Goncharuk, A. A. Novza, A. V. Turov, and A. A. Chuiko. Unusual properties of water at hydrophilic/hydrophobic interfaces. *Advances in Colloid and Interface Science*, 118(1-3):125–172, 2005.

[127] A. Serva, S. Pezzotti, S. Bougueroua, D. R. Galimberti, and M.-P. Gaigeot. Combining ab-initio and classical molecular dynamics simulations to unravel the structure of the 2d-hb-network at the air-water interface. *Journal of Molecular Structure*, 1165:71–78, 2018.

[128] W. A. P. Luck. The influence of ions on water structure and on aqueous systems. In *Water and Ions in Biological Systems*, pages 95–126. Springer, 1985.

[129] B. Halliwell and J. M. C. Gutteridge. The importance of free radicals and catalytic metal ions in human diseases. *Molecular aspects of medicine*, 8(2):89–193, 1985.

[130] E. J. Tokar, L. Benbrahim-Tallaa, and M. P. Waalkes. Metal ions in human cancer development. *Metal Ions in Toxicology: Effects, Interactions, Interdependencies*, 8:375, 2015.

[131] S. S. Gnanamanickam. Rice and its importance to human life. In *Biological control of rice diseases*, pages 1–11. Springer, 2009.

[132] K. Münger, W. C. Phelps, V. Bubb, P. M. Howley, and R. Schlegel. The e6 and e7 genes of the human papillomavirus type 16 together are necessary and sufficient for transformation of primary human keratinocytes. *Journal of virology*, 63(10):4417–4421, 1989.

[133] D. P. Woodruff. *The Solid-Liquid Interface.* CUP Archive, 1973.

[134] A. W. Adamson and A. P. Gast. *Physical chemistry of surfaces.* Interscience publishers New York, 1967.

[135] W. Norde. Driving forces for protein adsorption at solid surfaces. In *Macromolecular Symposia*, volume 103, pages 5–18. Wiley Online Library, 1996.

[136] M. Bellion, L. Santen, H. Mantz, H. Hähl, A. Quinn, A. Nagel, C. Gilow, C. Weitenberg, Y. Schmitt, and K. Jacobs. Protein adsorption on tailored substrates: long-range forces and conformational changes. *Journal of Physics: Condensed Matter*, 20(40):404226, 2008.

[137] J. Koo, T. Gutberlet, and C. Czeslik. Control of protein interfacial affinity by nonionic cosolvents. *The Journal of Physical Chemistry B*, 112(20):6292–6295, 2008.

[138] C. F. Wertz and M. M. Santore. Adsorption and reorientation kinetics of lysozyme on hydrophobic surfaces. *Langmuir*, 18(4):1190–1199, 2002.

[139] M. Chaplin. Water Structure and Science. 2018-08-31, http://www1.lsbu.ac.uk/water/index.html.

[140] J. C. Slater. Atomic radii in crystals. *The Journal of Chemical Physics*, 41(10):3199–3204, 1964.

[141] B. Cordero, V. Gómez, A. E. Platero-Prats, M. Revés, J. Echeverría, E. Cremades, F. Barragán, and S. Alvarez. Covalent radii revisited. *Dalton Trans.*, 0:2832, 2008.

[142] A. Bondi. van der waals volumes and radii. *The Journal of physical chemistry*, 68(3):441–451, 1964.

[143] M. Mantina, A. C. Chamberlin, R. Valero, C. J. Cramer, and D. G. Truhlar. Consistent van der waals radii for the whole main group. *The Journal of Physical Chemistry A*, 113(19):5806–5812, 2009.

[144] R. D. Shannon. Revised effective ionic radii and systematic studies of interatomic distances in halides and chalcogenides. *Acta crystallographica section A: crystal physics, diffraction, theoretical and general crystallography*, 32(5):751–767, 1976.

[145] F. Hofmeister. Zur lehre von der wirkung der salze. *Archiv für experimentelle Pathologie und Pharmakologie*, 25(1):1–30, 1888.

[146] W. Kunz, J. Henle, and B. W. Ninham. 'zur lehre von der wirkung der salze'(about the science of the effect of salts): Franz hofmeister's historical papers. *Current Opinion in Colloid & Interface Science*, 9(1-2):19–37, 2004.

[147] Andrea Salis and Barry W Ninham. Models and mechanisms of hofmeister effects in electrolyte solutions, and colloid and protein systems revisited. *Chemical Society Reviews*, 43(21):7358–7377, 2014.

[148] M. Chaplin. Hofmeister Series. 2018-08-31, http://www1.lsbu.ac.uk/water/hofmeister_series.html.

[149] G. A. Petsko and D. Ringe. *Protein structure and function.* New Science Press, 2004.

[150] C. Branden and J. Tooze. *Introduction to Protein Structure. New York: Garland Pub.* Garland Publishing, 1999.

[151] A. Lesk. *Introduction to protein science: architecture, function, and genomics.* Oxford university press, 2010.

[152] R. Diamond. Real-space refinement of the structure of hen egg-white lysozyme. *Journal of Molecular Biology*, 82(3):371–391, 1974.

[153] K. Rezwan, L. P. Meier, and L. J. Gauckler. A prediction method for the iso-electric point of binary protein mixtures of bovine serum albumin and lysozyme adsorbed on colloidal titania and alumina particles. *Langmuir*, 21:3493–3497, 2005.

[154] R. Diamond. Real-space refinement of the structure of hen egg-white lysozyme, *Journal of Molecular Biology*, 82(3):371-391, 1974 - pdb id: 2lyz. 2018-08-31, https://www.rcsb.org/structure/2lyz.

[155] R. David and A. W. Neumann. Contact angle patterns on low-energy surfaces. *Advances in colloid and interface science*, 206:46–56, 2014.

[156] T. Young. An assay on the cohesion of fluids. philos. Technical report, TR Soc., 95: 65-87, 1805.

[157] R. Förch, H. Schönherr, and A. T. A. Jenkins. *Surface design: applications in bioscience and nanotechnology.* John Wiley & Sons, 2009.

[158] N. Stevens, C. I. Priest, R. Sedev, and J. Ralston. Wettability of photoresponsive titanium dioxide surfaces. *Langmuir*, 19(8):3272–3275, 2003.

[159] Wikipedia. Octadecyltrichlorosilane. 2018-08-31, https://commons.wikimedia.org/wiki/File:Octadecyltrichlorosilane-3D-sf.png.

[160] M. Malmsten. Formation of adsorbed protein layers. *Journal of colloid and interface science*, 207(2):186–199, 1998.

[161] S. D. Chakarova and A. E. Carlsson. Model study of protein unfolding by inter-faces. *Physical Review E*, 69(2):021907, 2004.

[162] K. K. Goli, O. J. Rojas, A. E. Özçam, and J. Genzer. Generation of functio-nal coatings on hydrophobic surfaces through deposition of denatured proteins followed by grafting from polymerization. *Biomacromolecules*, 13(5):1371–1382, 2012.

[163] G. Raffaini and F. Ganazzoli. Protein adsorption on a hydrophobic surface: a molecular dynamics study of lysozyme on graphite. *Langmuir*, 26(8):5679–5689, 2009.

[164] K. Dill, R. L. Jernigan, and I. Bahar. *Protein Actions: Principles and Modeling.* Garland Science, 2017.

[165] F. Meersman, C. M. Dobson, and K. Heremans. Protein unfolding, amyloid fibril formation and configurational energy landscapes under high pressure conditions. *Chemical Society Reviews*, 35(10):908–917, 2006.

[166] M. Tolan. *X-ray scattering from soft-matter thin films: materials science and basic research.* Springer, 1999.

[167] J. Als-Nielsen and D. McMorrow. *Elements of Modern X-ray Physics.* Wiley, 2011.

[168] M. Paulus. *Röntgenstreuung an Flüssigkeits-Gas Grenzflächen.* PhD thesis, Universität Dortmund, 2006.

[169] I. Kiesel. *In situ Untersuchung von Proteinen an Grenzflächen mit oberflächensensitiven Röntgenstreumethoden.* PhD thesis, TU Dortmund, 2014.

[170] L. G. Parratt. Surface studies of solids by total reflection of x-rays. *Phys. Rev.*, 95:359–369, 1954.

[171] H. Kiessig. Interferenz von röntgenstrahlen an dünnen schichten. *Annalen der Physik*, 402(7):769–788, 1931.

[172] M. Paulus, D. Lietz, C. Sternemann, K. Shokuie, F. Evers, M. Tolan, C. Czeslik, and R. Winter. An access to buried interfaces: the X-ray reflectivity set-up of BL9 at DELTA. *Journal of Synchrotron Radiation*, 15(6):600–605, 2008.

[173] M. Paulus, R. Fendt, C. Sternemann, C. Gutt, H. Hövel, M. Volmer, M. Tolan, and K. Wille. An internet-based synchrotron experiment for students measuring the X-ray magnetic circular dichroism of a PtFe alloy. *Journal of Synchrotron Radiation*, 12(2):246–250, 2005.

[174] C. Krywka, M. Paulus, C. Sternemann, M. Volmer, A. Remhof, G. Nowak, A. Nefedov, B. Pöter, M. Spiegel, and M. Tolan. The new diffractometer for surface X-ray diffraction at beamline BL9 of DELTA. *Journal of Synchrotron Radiation*, 13(1):8–13, 2006.

[175] C. Krywka, C. Sternemann, M. Paulus, N. Javid, R. Winter, A. Al-Sawalmih, S. Yi, D. Raabe, and M. Tolan. The small-angle and wide-angle X-ray scattering set-up at beamline BL9 of DELTA. Erratum. *Journal of Synchrotron Radiation*, 14(4):391, 2007.

[176] C. Reich, M. B. Hochrein, B. Krause, and B. Nickel. A microfluidic setup for studies of solid-liquid interfaces using x-ray reflectivity and fluorescence microscopy. *Review of Scientific Instruments*, 76(9):095103, 2005.

[177] European Synchrotron Radiation Facility. Esrf homepage - id31. 2018-08-31, http://www.esrf.eu/UsersAndScience/Experiments/StructMaterials/ID31.

[178] European Synchrotron Radiation Facility. Esrf homepage - accelerators - parameters. 2018-08-31, http://www.esrf.eu/home/UsersAndScience/Accelerators/parameters.html.

[179] M.A. Farhataziz and J. Rodgers. *Radiation chemistry: principles and applications.* VCH Publishers, 1987.

[180] N. Tîmneanu, C. Caleman, J. Hajdu, and D. van der Spoel. Auger electron cascades in water and ice. *Chemical Physics*, 299(2):277–283, 2004.

[181] P. R. Willmott, D. Meister, S. J. Leake, M. Lange, A. Bergamaschi, M. Böge, M. Calvi, C. Cancellieri, N. Casati, A. Cervellino, Q. Chen, C. David, U. Flechsig, F. Gozzo, B. Henrich, S. Jäggi-Spielmann, B. Jakob, I. Kalichava, P. Karvinen, J. Krempasky, A. Lüdeke, R. Lüscher, S. Maag, C. Quitmann, M. L. Reinle-Schmitt, T. Schmidt, B. Schmitt, A. Streun, I. Vartiainen, M. Vitins, X. Wang, and R. Wullschleger. The Materials Science beamline upgrade at the Swiss Light Source. *Journal of Synchrotron Radiation*, 20(5):667–682, 2013.

[182] B.D. Patterson, R. Abela, H. Auderset, Q. Chen, F. Fauth, F. Gozzo, G. Ingold, H. Kühne, M. Lange, D. Maden, D. Meister, P. Pattison, Th. Schmidt, B. Schmitt, C. Schulze-Briese, M. Shi, M. Stampanoni, and P.R. Willmott. The materials science beamline at the swiss light source: design and realization. *Nuclear Instruments and Methods in Physics Research Section A: Accelerators, Spectrometers, Detectors and Associated Equipment*, 540(1):42 – 67, 2005.

[183] O. H. Seeck, C. Deiter, K. Pflaum, F. Bertam, A. Beerlink, H. Franz, J. Horbach, H. Schulte-Schrepping, B. M. Murphy, M. Greve, and O. Magnussen. The high-resolution diffraction beamline P08 at PETRA III. *Journal of Synchrotron Radiation*, 19(1):30–38, 2012.

[184] P. Reckers, M. Dimamay, J. Klett, S. Trost, K. Zilberberg, T. Riedl, B. Parkinson, J. Broötz, W. Jaegermann, and T. Mayer. Deep and shallow tio2 gap states on cleaved anatase single crystal (101) surfaces, nanocrystalline anatase films, and ald titania ante and post annealing. *J. Phys. Chem C*, 119:9890–9898, 2015.

[185] P. Eaton and P. West. *Atomic force microscopy.* Oxford University Press, 2010.

[186] D. Rugar and P. Hansma. Atomic force microscopy. *Physics today*, 43(10):23–30, 1990.

[187] Y. Kitamura and T. Itoh. Reaction volume of protonic ionization for buffering agents. prediction of pressure dependence of ph and poh. *Journal of Solution Chemistry*, 16(9):715–725, 1987.

[188] S. Onclin, B. J. Ravoo, and D. N. Reinhoudt. Engineering silicon oxide surfaces using self-assembled monolayers. *Angewandte Chemie International Edition*, 44(39):6282–6304, 2005.

[189] Y. Wang and M. Lieberman. Growth of ultrasmooth octadecyltrichlorosilane self-assembled monolayers on sio2. *Langmuir*, 19(4):1159–1167, 2003.

[190] P. Lo Nostro and B. W. Ninham. Hofmeister phenomena: an update on ion specificity in biology. *Chemical reviews*, 112(4):2286–2322, 2012.

[191] H. I. Okur, J. Hladílková, K. B. Rembert, Y. Cho, J. Heyda, J. Dzubiella, P. S. Cremer, and P. Jungwirth. Beyond the hofmeister series: ion-specific effects on proteins and their biological functions. *The Journal of Physical Chemistry B*, 121(9):1997–2014, 2017.

[192] F. J. Wirkert, M. Paulus, J. Nase, J. Möller, S. Kujawski, C. Sternemann, and M. Tolan. X-ray reflectivity measurements of liquid/solid interfaces under high hydrostatic pressure conditions. *Journal of Synchrotron Radiation*, 21(1):76–81, 2014.

[193] I. M. Tidswell, B. M. Ocko, P. S. Pershan, S. R. Wasserman, G. M. Whitesides, and J. D. Axe. X-ray specular reflection studies of silicon coated by organic monolayers (alkylsiloxanes). *Phys. Rev. B*, 41:1111–1128, 1990.

[194] H.-G. Steinrück, A. Schiener, T. Schindler, J. Will, A. Magerl, O. Konovalov, G. Li Destri, O. H. Seeck, M. Mezger, J. Haddad, M. Deutsch, A. Checco, and B. M. Ocko. Nanoscale structure of si/sio2/organics interfaces. *ACS Nano*, 8(12):12676–12681, 2014.

[195] O. Hollmann, R. Steitz, and C. Czeslik. Structure and dynamics of alpha-lactalbumin adsorbed at a charged brush interface. *Phys. Chem. Chem. Phys.*, 10:1448–1456, 2008.

[196] E. F. Pettersen, T. D. Goddard, C. C. Huang, G. S. Couch, D. M. Greenblatt, E. C. Meng, and T. E. Ferrin. Ucsf chimera-a visualization system for exploratory research and analysis. *Journal of computational chemistry*, 25(13):1605–1612, 2004.

[197] M. F. Sanner, A. J. Olson, and J.-C. Spehner. Reduced surface: an efficient way to compute molecular surfaces. *Biopolymers*, 38(3):305–320, 1996.

[198] J. F. Back, D. Oakenfull, and M. B. Smith. Increased thermal stability of proteins in the presence of sugars and polyols. *Biochemistry*, 18(23):5191–5196, 1979.

[199] J. Israelachvili. *Intermolecular and surface forces*. Academic Press, 2000.

[200] L. Bergström. Hamaker constants of inorganic materials. *Advancesin Colloid and Interface Science*, 70:125–169l, 1997.

[201] C. Gripon, L. Legrand, I. Rosenman, O. Vidal, M. Robert, and F. Boub. Lysozyme-lysozyme interactions in under- and super-saturated solutions: a simple relation between the second virial coefficients in h20 and d20. *Journal of Crystal Growth*, 178:575–584, 1997.

[202] F. L. Leite, C. C. Bueno, A. L. Da Róz, E. C. Ziemath, and O. N. Oliveira. Theoretical models for surface forces and adhesion and their measurement using atomic force microscopy. *Int J Mol Sci.*, 13(10):12773–12856, 2012.

[203] M. S. Yeganeh, S. M. Dougal, and H. S. Pink. Vibrational spectroscopy of water at liquid/solid interfaces: Crossing the isoelectric point of a solid surface. *Phys. Rev. Lett.*, 83:1179–1182, 1999.

[204] J. W. Bullard and M. J. Cima. Orientation dependence of the isoelectric point of tio2 (rutile) surfaces. *Langmuir*, 22(24):10264–10271, 2006.

[205] C. M. Roth and A. M. Lenhoff. Electrostatic and van der waals contributions to protein adsorption: computation of equilibrium constants. *Langmuir*, 9(4):962–972, 1993.

[206] K. H. Biswas, J. A. Jackman, J. H. Park, J. T. Groves, and N.-J. Cho. Interfacial forces dictate the pathway of phospholipid vesicle adsorption onto silicon dioxide surfaces. *Langmuir*, 34(4):1775–1782, 2018.

[207] N. V. Nucci, B. Fuglestad, E. A. Athanasoula, and A. J. Wand. Role of cavities and hydration in the pressure unfolding of t4 lysozyme. *PNAS.*, 111:13846–13651, 2014.

[208] T. V. Chalikian and R. B. Macgregor. Origins of pressure-induced protein transitions. *J Mol Biol.*, 394:834–842, 2009.

[209] D. Russo, M. G. Ortore, F. Spinozzi, P. Mariani, C. Loupiac, B. Annighofer, and A. Paciaroni. The impact of high hydrostatic pressure on structure and dynamics of β-lactoglobulin. *Biochimica et Biophysica Acta*, 1830:4974–4980, 2013.

[210] I. Danielewicz-Ferchmin, E. M. Banachowicz, and A. R. Ferchmin. Role of electromechanical and mechanoelectric effects in protein hydration under hydrostatic pressure. *PCCP*, 13:17722–17728, 2011.

[211] K. Julius, S. R. Al-Ayoubi, M. Paulus, M. Tolan, and R. Winter. The effects of osmolytes and crowding on the pressure-induced dissociation and inactivation of dimeric ladh. *Phys. Chem. Chem. Phys.*, 20:7093–7104, 2018.

[212] M. A. Schroer, Y. Zhai, D. C. F. Wieland, Ch. J. Sahle, J. Nase, M. Paulus, M. Tolan, and R. Winter. Exploring the piezophilic behavior of natural cosolvent mixtures. *Angewandte Chemie International Edition*, 50:11413, 2011.

[213] J. Koo, M. Erlkamp, S. Grobelny, R. Steitz, and C. Czeslik. Pressure-induced protein adsorption at aqueous-solid interfaces. *Langmuir*, 29:8025–8030, 2013.

[214] M. Chu. *X-ray Reflectivity Study of Ionic Liquids at Electrified Surfaces*. PhD thesis, NORTHWESTERN UNIVERSITY, 2017.

[215] R. Scheu, B. M. Rankin, Y. Chen, K. C. Jena, D. Ben-Amotz, and S. Roke. Charge asymmetry at aqueous hydrophobic interfaces and hydration shells. *Angewandte Chemie International Edition*, 53(36):9560–9563, 2014.

[216] C. Dong, W. Xiang, F. Huang, D. Fu, W. Huang, U. Bach, Y.-B. Cheng, X. Li, and L. Spiccia. Controlling interfacial recombination in aqueous dye-sensitized solar cells by octadecyltrichlorosilane surface treatment. *Angewandte Chemie International Edition*, 53(27):6933–6937, 2014.

[217] A. Kumar, K. Staněk, P. Ryparová, P. Hajek, and J. Tywoniak. Hydrophobic treatment of wood fibrous thermal insulator by octadecyltrichlorosilane and its influence on hygric properties and resistance against moulds. *Composites Part B: Engineering*, 106:285–293, 2016.

[218] A. E. Lauritzen, M. Torkkeli, O. Bikondoa, J. Linnet, L. Tavares, J. Kjelstrup-Hansen, and M. Knaapila. Structural evaluation of 5,5'-bis(naphth-2-yl)-2,2'-bithiophene in organic field-effect transistors with n-octadecyltrichlorosilane coated sio2 gate dielectric. *Langmuir*, 34(23):6727–6736, 2018.

[219] Markus M. *X-ray studies of the density depletion at hydrophobic water-solid interfaces*. PhD thesis, Max-Planck-Institut für Metallforschung, 2008.

[220] F. J. Wirkert, C. Hölzl, M. Paulus, P. Salmen, M. Tolan, D. Horinek, and J. Nase. The hydrophobic gap at high hydrostatic pressures. *Angewandte Chemie International Edition*, 56(42):12958–12961, 2017.

[221] T. R. Jensen, M. Østergaard Jensen, N. Reitzel, K. Balashev, G. H. Peters, K. Kjaer, and T. Bjørnholm. Water in contact with extended hydrophobic surfaces: Direct evidence of weak dewetting. *Phys. Rev. Lett.*, 90:086101, 2003.

[222] M. Mezger, S. Schöder, H. Reichert, H. Schröder, J. Okasinski, V. Honkimäki, J. Ralston, J. Bilgram, R. Roth, and H. Dosch. Water and ice in contact with octadecyl-trichlorosilane functionalized surfaces: A high resolution x-ray reflectivity study. *The Journal of Chemical Physics*, 128(24):244705, 2008.

[223] D. Eisenberg and W. Kauzmann. *The Structure and Properties of Water*. Oxford University Press, 1969.

[224] R. J. Speedy and C. A. Angell. Isothermal compressibility of supercooled water and evidence for a thermodynamic singularity at 45°C. *The Journal of Chemical Physics*, 65(3):851–858, 1976.

[225] P. H. Poole, F. Sciortino, U. Essmann, and H. E. Stanley. Phase behaviour of metastable water. *Nature*, 360(6402):324, 1992.

[226] C. A. Angell. Insights into Phases of Liquid Water from Study of Its Unusual Glass-Forming Properties. *Science*, 319(5863):582–587, 2008.

[227] A. K. Soper. Chapter 3 - the structure of water and aqueous systems. In Felix Fernandez-Alonso and David L. Price, editors, *Neutron Scattering - Applications in Biology, Chemistry, and Materials Science*, volume 49 of *Experimental Methods in the Physical Sciences*, pages 135 – 211. Academic Press, 2017.

[228] L. G.M. Pettersson and A. Nilsson. The structure of water; from ambient to deeply supercooled. *Journal of Non-Crystalline Solids*, 407:399–417, 2015.

[229] P. G. Debenedetti. Supercooled and glassy water. *Journal of Physics: Condensed Matter*, 15(45):R1669, 2003.

[230] F. Mallamace, C. Corsaro, and H. E. Stanley. Possible relation of water structural relaxation to water anomalies. *Proceedings of the National Academy of Sciences*, 110(13):4899–4904, 2013.

[231] T. R. M. Barends, L. Foucar, S. Botha, R. B. Doak, R. L. Shoeman, K. Nass, J. E. Koglin, G. J. Williams, S. Boutet, M. Messerschmidt, and I. Schlichting. De novo protein crystal structure determination from x-ray free-electron laser data. *Nature*, 505:244–247, 2014.

[232] T. Ekeberg, M. Svenda, C. Abergel, F. R. N. C. Maia, V. Seltzer, J.-M. Claverie, M. Hantke, O. Jönsson, C. Nettelblad, G. van der Schot, M. Liang, D. P. DePonte, A. Barty, M. M. Seibert, B. Iwan, I. Andersson, N. D. Loh, A. V. Martin, H. Chapman, C. Bostedt, J. D. Bozek, K. R. Ferguson, J. Krzywinski, S. W. Epp, D. Rolles, A. Rudenko, R. Hartmann, N. Kimmel, and J. Hajdu. Three-dimensional reconstruction of the giant mimivirus particle with an x-ray free-electron laser. *Phys. Rev. Lett.*, 114:098102, 2015.

[233] S. Cousens, B. Reville, B. Dromey, and M. Zepf. Temporal structure of attosecond pulses from laser-driven coherent synchrotron emission. *Phys. Rev. Lett.*, 116:083901, 2016.

[234] M. J. Cooper, P. E. Mijnarends, N. Shiotani, N. Sakai, and A. Bansil. *X-Ray Compton Scattering*. Oxford University Press, 2004.

[235] K. Hämäläinen and S. Manninen. Resonant and non-resonant inelastic x-ray scattering. *Journal of Physics: Condensed Matter*, 13(34):7539, 2001.

[236] L. Van Hove. Correlations in Space and Time and Born Approximation Scattering in Systems of Interacting Particles. *Phys. Rev.*, 95:249–262, 1954.

[237] Lawrence Berkeley National Laboratory. X-ray Data Booklet: Electron binding energies for the elements H to Ti in their natural forms. 2018-08-31, http://xdb.lbl.gov/Section1/Table_1-1a.htm.

[238] Lawrence Berkeley National Laboratory. X-ray Data Booklet: Electron binding energies for the elements Lu to U in their natural forms. 2018-08-31, http://xdb.lbl.gov/Section1/Table_1-1c.htm.

[239] F. Lehmkühler. *Formation of clathrate hydrates: An x-ray scattering study.* PhD thesis, TU Dortmund, 2010.

[240] J. D. Jackson. *Classical Electrodynamics.* John Wiley & Sons, New York, 2nd edition, 1975. Chap. 7.10.

[241] RIKEN/JASRI. Spring-8 homepage - bl12xu outline. 2018-08-31, http://www.spring8.or.jp/wkg/BL12XU/instrument/lang-en/INS-0000000566/instrument_summary_view.

[242] N. Hiraoka, H. Fukui, H. Tanida, H. Toyokawa, Y. Q. Cai, and K. D. Tsuei. An x-ray raman spectrometer for exafs studies on minerals: bent laue spectrometer with 20 kev x-rays. *Journal of synchrotron radiation*, 20(2):266–271, 2013.

[243] National Institute of Standards and Technology. Photon cross section database. 2018-08-31, http://physics.nist.gov/PhysRefData/Xcom/html/xcom1.html.

[244] R. Ribberfors. Relationship of the relativistic Compton cross section to the momentum distribution of bound electron states. *Phys. Rev. B*, 12:2067–2074, 1975.

[245] R. Ribberfors. Relationship of the relativistic compton cross section to the momentum distribution of bound electron states. ii. effects of anisotropy and polarization. *Physical Review B*, 12(8):3136, 1975.

[246] P. Holm and R. Ribberfors. First correction to the nonrelativistic Compton cross section in the impulse approximation. *Phys. Rev. A*, 40:6251–6259, 1989.

[247] C. Sternemann. *Final state interaction and temperature effects in Compton scattering from lithium.* PhD thesis, Universität Dortmund, 2000.

[248] J. Felsteiner, P. Pattison, and M. Cooper. Effect of multiple scattering on experimental compton profiles: a monte carlo calculation. *Philosophical Magazine*, 30(3):537–548, 1974.

[249] Ja. Chomilier, G. Loupias, and J. Felsteiner. Correction for multiple scattering in compton profile experiments: Application for synchrotron source photons. *Nuclear Instruments and Methods in Physics Research Section A: Accelerators, Spectrometers, Detectors and Associated Equipment*, 235(3):603–606, 1985.

[250] N. Sakai. Simulation of compton double scatterings of circularly polarized γ-rays by magnetic electrons. *J. Phys. Soc. Jpn.*, 56:2477, 1987.

[251] P. Fajardo, V. Honkimäki, Th. Buslaps, and P. Suortti. Experimental validation of multiple scattering calculations with high energy x-ray photons. *Nuclear Instruments and Methods in Physics Research Section B: Beam Interactions with Materials and Atoms*, 134(3-4):337–345, 1998.

[252] M. Brancewicz, M. Itou, and Y. Sakurai. A monte carlo study of high-energy photon transport in matter: application for multiple scattering investigation in compton spectroscopy. *Journal of synchrotron radiation*, 23(1):244–252, 2016.

[253] J. Chen, A. Zhao, H. Chen, Y. Liao, P. Yang, H. Sun, and N. Huang. The effect of full/partial uv-irradiation of tio2 films on altering the behavior of fibrinogen and platelets. *Colloids and Surfaces B: Biointerfaces*, 122:709–718, 2014.

[254] M. Anpo and M. Takeuchi. The design and development of highly reactive titanium oxide photocatalysts operating under visible light irradiation. *Journal of catalysis*, 216(1-2):505–516, 2003.

Appendix A

Lysozyme on Titanium Oxide
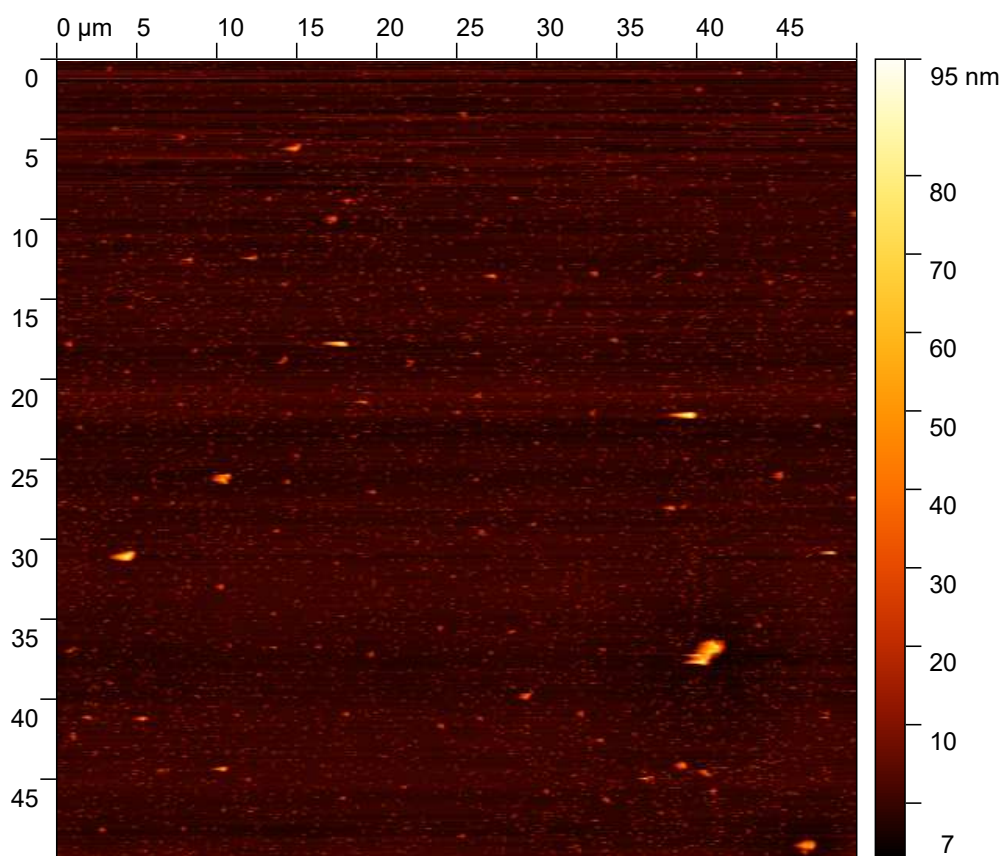
Figure A.1: Atomic Force Microscopy snapshot of a with titanium oxide covered silicon wafer. The snapshot shows a completely closed titanium oxide layer.
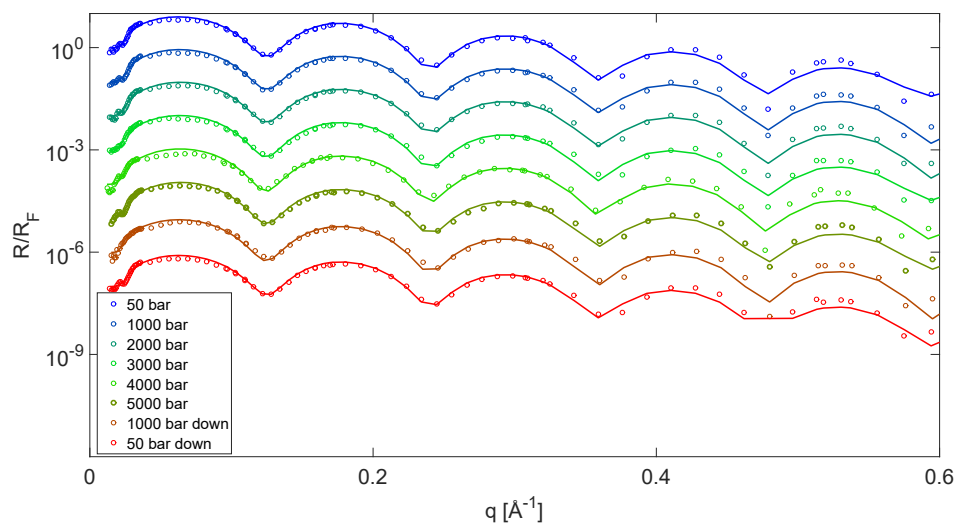
Figure A.2: Pressure dependent XRR measurements of lysozyme on the first wafer with a 50 Å thick titanium oxide layer, shifted on the y-scale for better visualization. The circles represent the measured data, while the solid lines show the fit to the data.
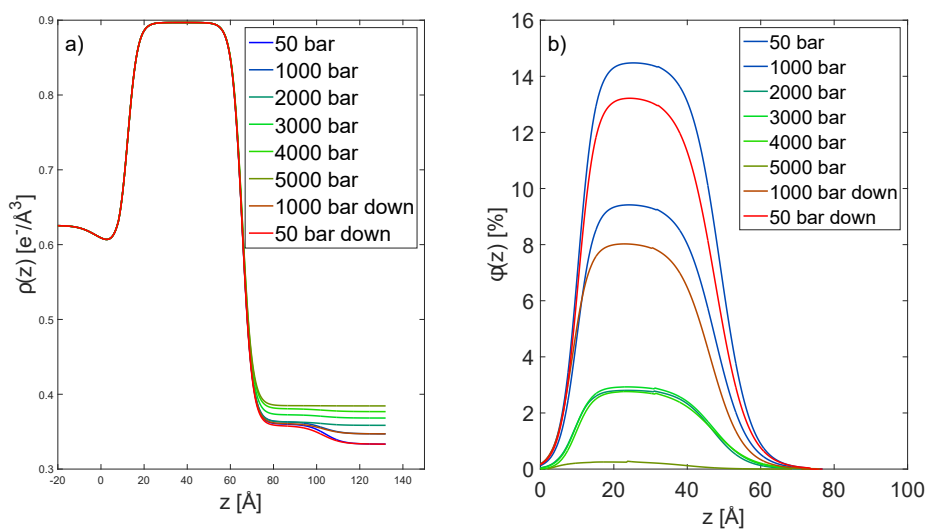
Figure A.3: a) EDPs of pressure dependent lysozyme adsorption on the first silicon wafer with a 50 Å thick titanium oxide layer at ambient temperature. b) Volume fraction profiles of the EDPs shown in a).
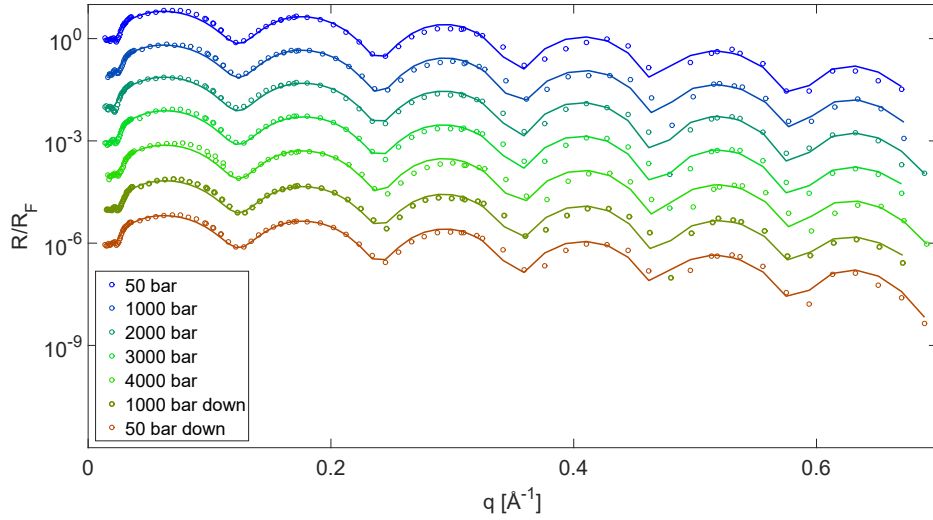
Figure A.4: Pressure dependent XRR measurements of lysozyme on the second wafer with a 50 Å thick titanium oxide layer, shifted on the y-scale for better visualization. The circles represent the measured data, while the solid lines show the fit to the data.
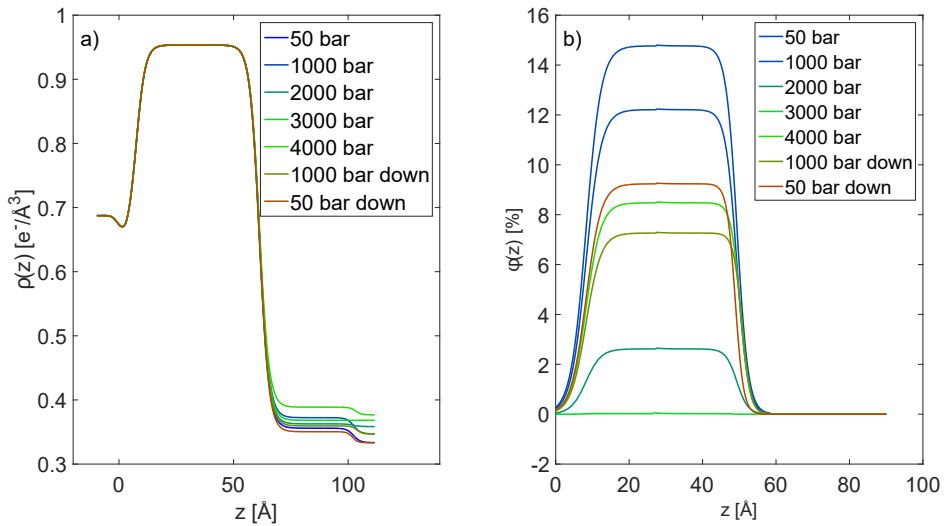
Figure A.5: a) EDPs of pressure dependent lysozyme adsorption on the second silicon wafer with a 50 Å thick titanium oxide layer at ambient temperature. b) Volume fraction profiles of the EDPs shown in a).
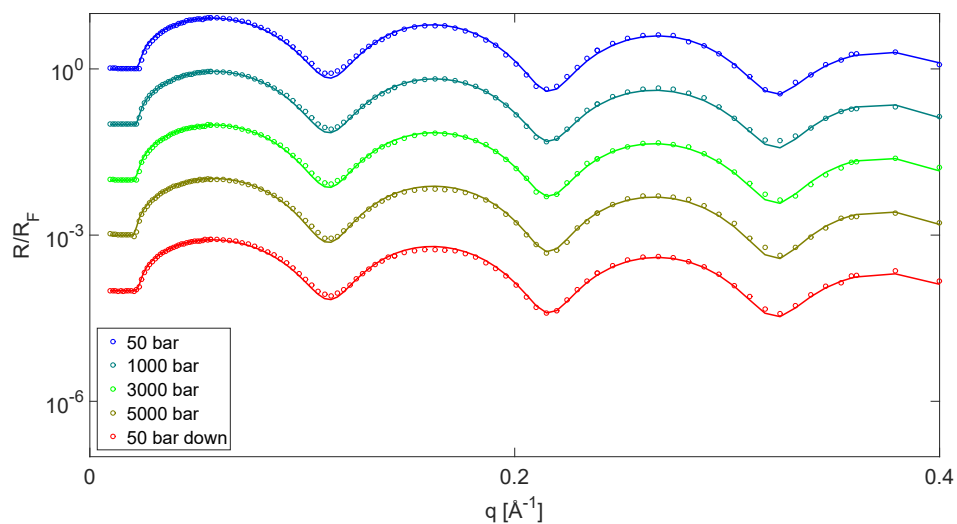
Figure A.6: Pressure dependent XRR measurements of lysozyme on a silicon wafer with a 60 Å thick titanium oxide layer, shifted on the y-scale for better visualization. The circles represent the measured data, while the solid lines show the fit to the data.
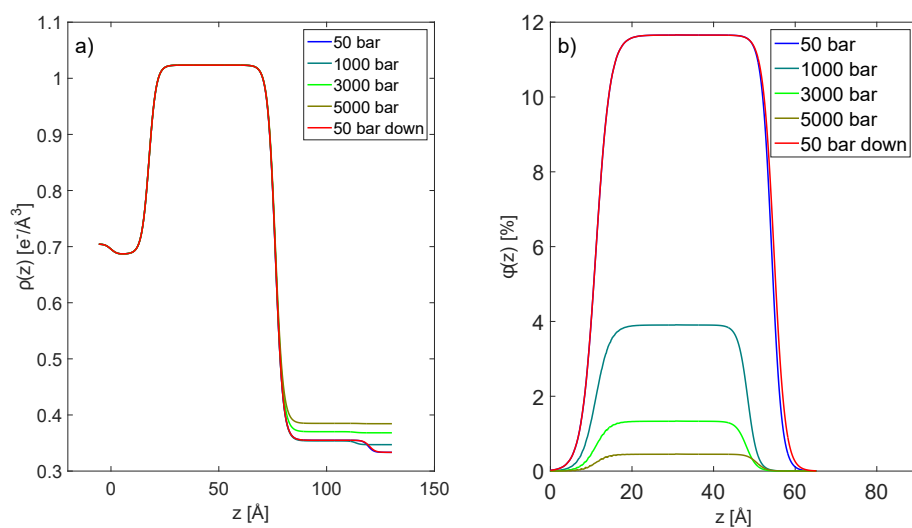
Figure A.7: a) EDPs of pressure dependent lysozyme adsorption on a silicon wafer with a 60 Å thick titanium oxide layer at ambient temperature. b) Volume fraction profiles of the EDPs shown in a).

Appendix B

Ions on OTS
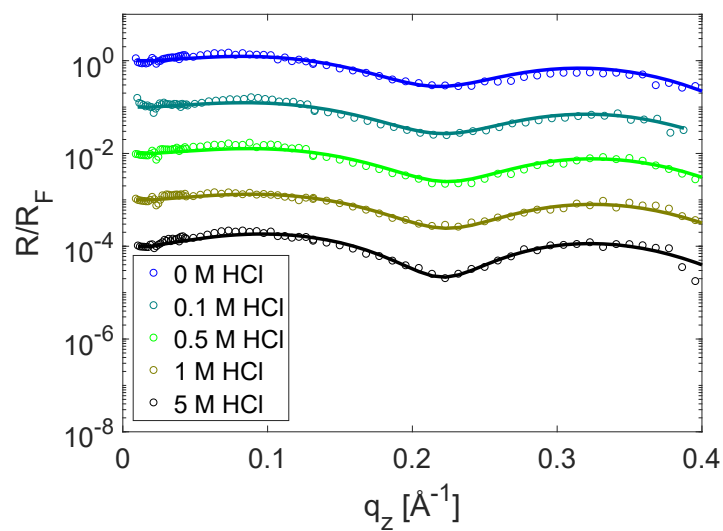
Figure B.1: XRR data of the adsorption of in water soluted hydrocloric acid on an OTS wafer as a function of ion concentration. The circles represent the measured data, while the solid lines show the fit to the data. The data as well as the fits are shifted on the y-scale for better visualization.
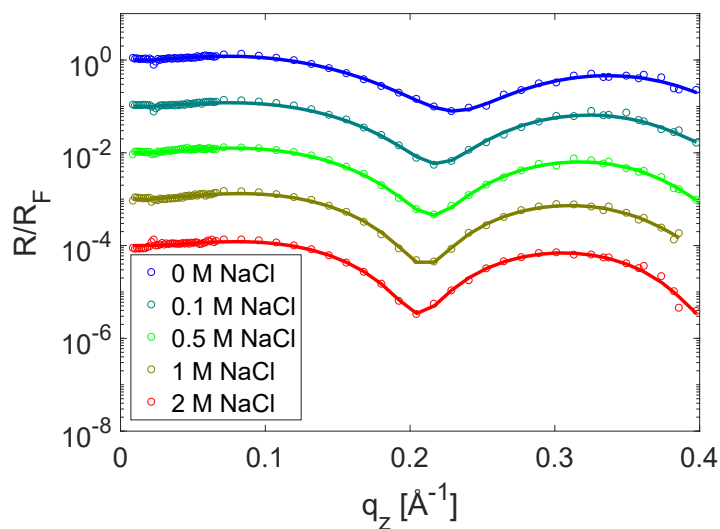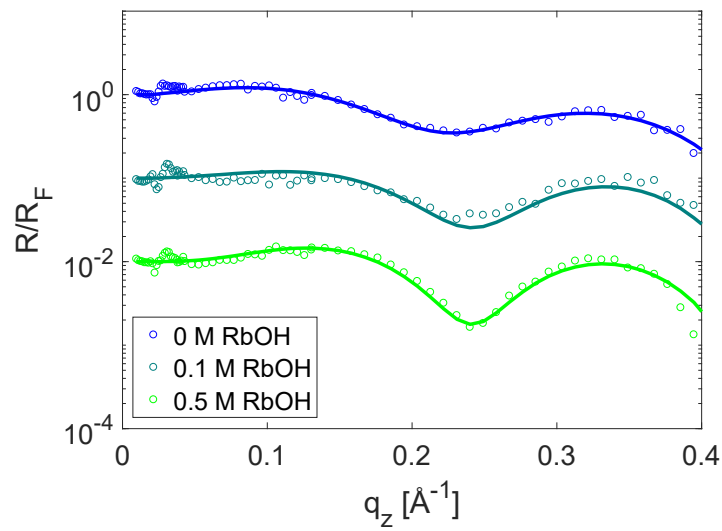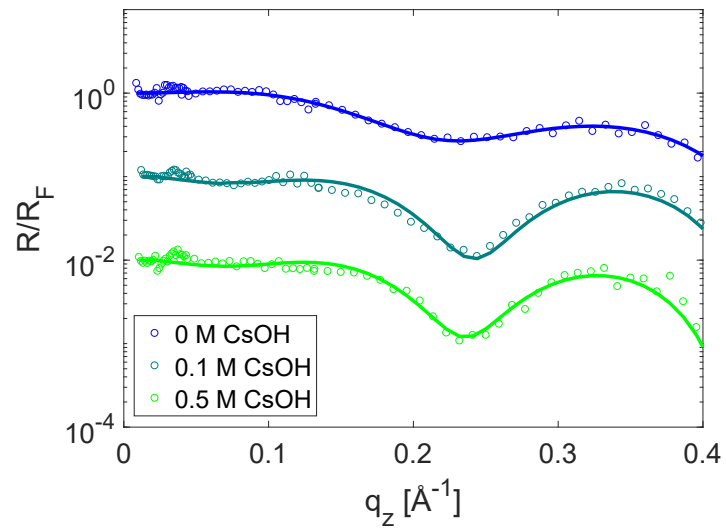
Figure B.2: XRR data of the adsorption of in water soluted sodium chloride on an OTS wafer as a function of ion concentration. The circles represent the measured data, while the solid lines show the fit to the data. The data as well as the fits are shifted on the y-scale for better visualization.
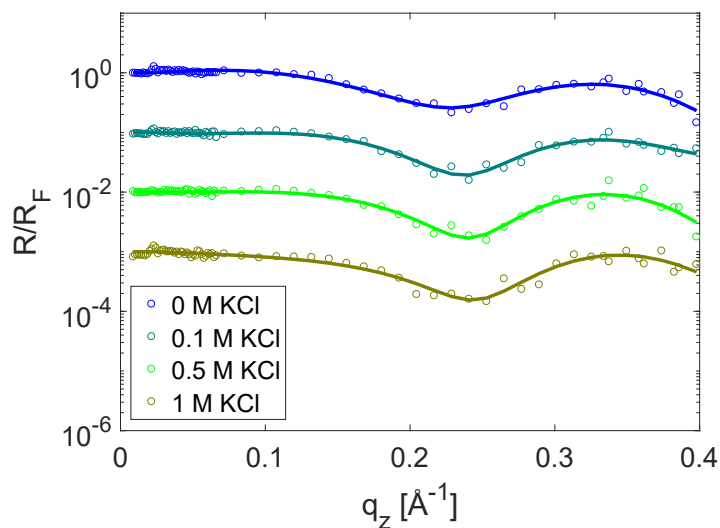
Figure B.3: XRR data of the adsorption of in water soluted potassium chloride on an OTS wafer as a function of ion concentration. The circles represent the measured data, while the solid lines show the fit to the data. The data as well as the fits are shifted on the y-scale for better visualization.
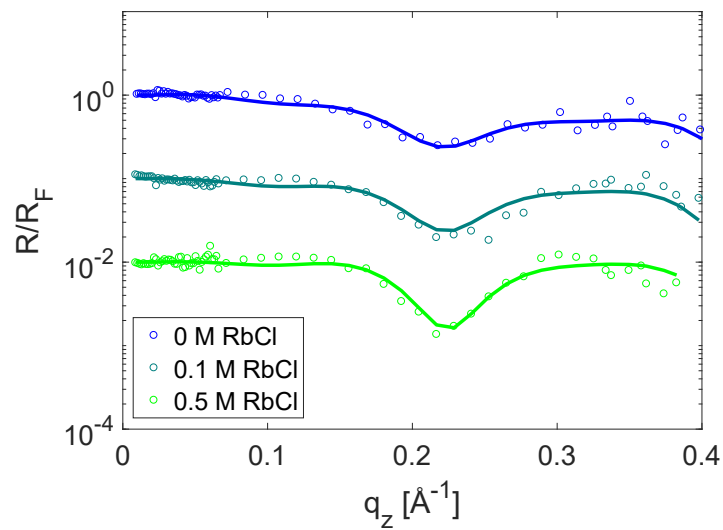
Figure B.4: XRR data of the adsorption of in water soluted rubidium chloride on an OTS wafer as a function of ion concentration. The circles represent the measured data, while the solid lines show the fit to the data. The data as well as the fits are shifted on the y-scale for better visualization.
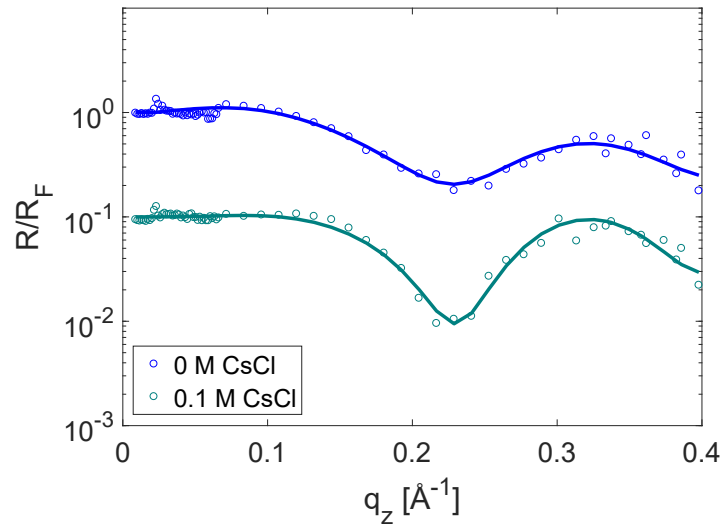
Figure B.5: XRR data of the adsorption of in water soluted caesium chloride on an OTS wafer as a function of ion concentration. The circles represent the measured data, while the solid lines show the fit to the data. The data as well as the fits are shifted on the y-scale for better visualization.
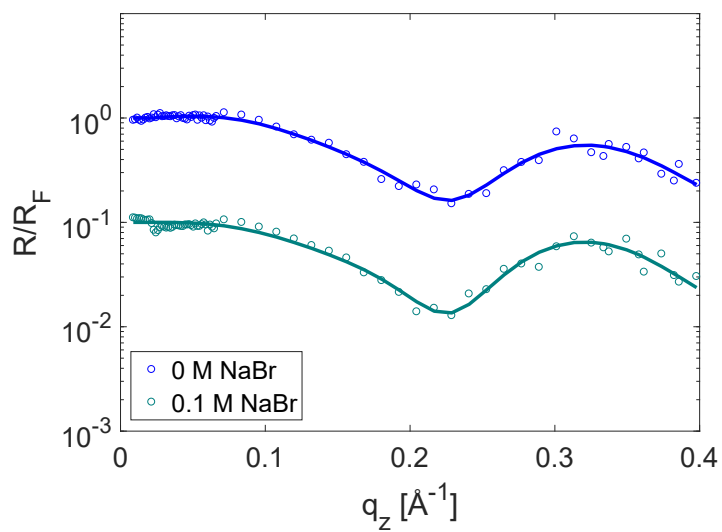
Figure B.6: XRR data of the adsorption of in water soluted sodium bromide on an OTS wafer as a function of ion concentration. The circles represent the measured data, while the solid lines show the fit to the data. The data as well as the fits are shifted on the y-scale for better visualization.
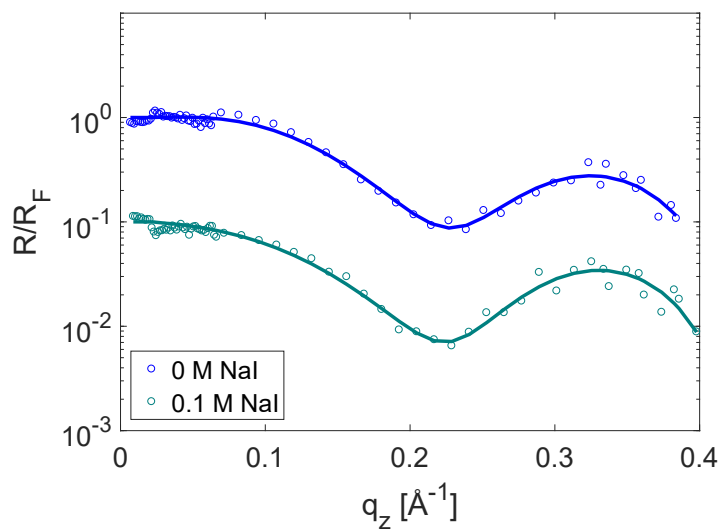
Figure B.7: XRR data of the adsorption of in water soluted sodium iodide on an OTS wafer as a function of ion concentration. The circles represent the measured data, while the solid lines show the fit to the data. The data as well as the fits are shifted on the y-scale for better visualization.
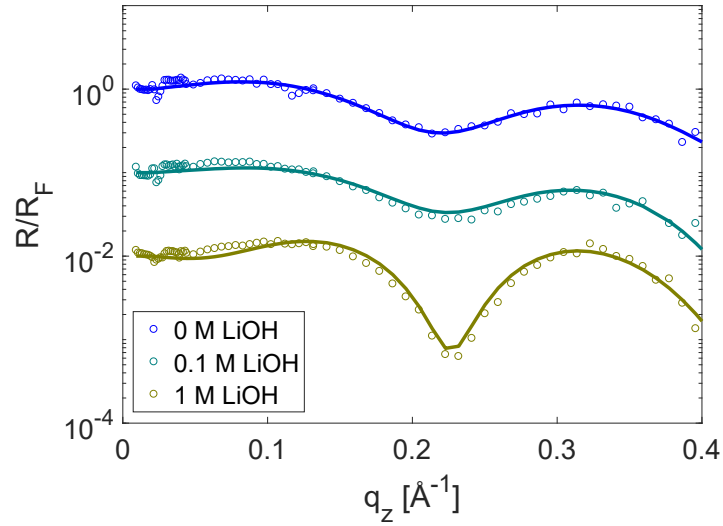
Figure B.8: XRR data of the adsorption of in water soluted lithium hydroxyde acid on an OTS wafer as a function of ion concentration. The circles represent the measured data, while the solid lines show the fit to the data. The data as well as the fits are shifted on the y-scale for better visualization.
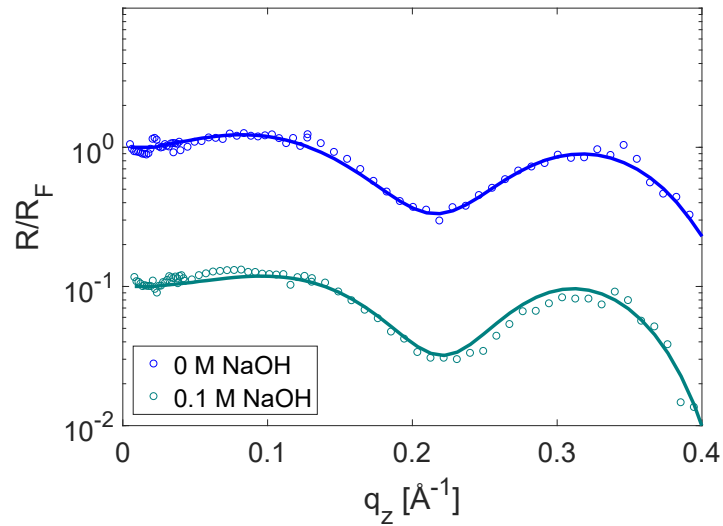
Figure B.9: XRR data of the adsorption of in water soluted sodium hydroxyde on an OTS wafer as a function of ion concentration. The circles represent the measured data, while the solid lines show the fit to the data. The data as well as the fits are shifted on the y-scale for better visualization.
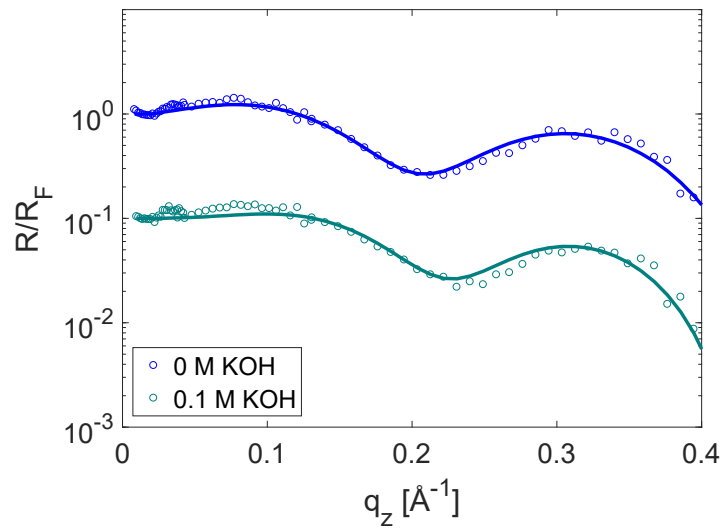
Figure B.10: XRR data of the adsorption of in water soluted potassium hydroxyde on an OTS wafer as a function of ion concentration. The circles represent the measured data, while the solid lines show the fit to the data. The data as well as the fits are shifted on the y-scale for better visualization.

Figure B.11: XRR data of the adsorption of in water soluted rubidium hydroxyde on an OTS wafer as a function of ion concentration. The circles represent the measured data, while the solid lines show the fit to the data. The data as well as the fits are shifted on the y-scale for better visualization.

Figure B.12: XRR data of the adsorption of in water soluted caesium hydroxyde on an OTS wafer as a function of ion concentration. The circles represent the measured data, while the solid lines show the fit to the data. The data as well as the fits are shifted on the y-scale for better visualization.

Publications

- **Y. Forov**, M. Paulus, S. Dogan, P. Salmen, C. Weis, T. Gahlmann, A. Behrendt, C. Albers, M. Elbers, W. Schnettger, S. Egger, E. Zwar, H. Rehage, I. Kiesel, T. Riedl und M. Tolan (2018). *Langmuir 34, 5403-5408*: "Adsorption Behavior of Lysozyme at Titanium Oxide-Water Interfaces ".

- F. Lehmkühler, **Y. Forov**, T. Büning, Ch. J. Sahle, I. Steinke, K. Julius, T. Buslaps, M. Tolan, M. Hakala, C. Sternemann (2016) *Phys. Chem. Chem. Phys. 18, 6925-6930*: "Intramolecular structure and energetics in supercooled water down to 255 K ".

- Ch. J. Sahle, C. Sternemann, C. Giacobbe, Y. Yan, C. Weis, M. Harder, **Y. Forov**, G. Spiekermann, M. Tolan, M. Krisch, und A. Remhof (2016). *Phys. Chem. Chem. Phys. 18, 19866-19872*: "Formation of CaB_6 in the thermal decomposition of the hydrogen storage material $Ca(BH_4)_2$".

- C. Weis, C. Sternemann, V. Cerantola, Ch. J. Sahle, G. Spiekermann, M. Harder, **Y. Forov**, A. Kononov, R. Sakrowski, H. Yavaş, M. Tolan und M. Wilke (2017). *Scientific Reports 7:16526*: "Pressure driven spin transition in siderite and magnesiosiderite single crystals ".

- F. Lehmkühler, **Y. Forov**, M. Elbers, I. Steinke, Ch. J. Sahle, C. Weis, N. Tsuji, M. Itou, Y. Sakurai, A. Poulain und C. Sternemann (2017). *Phys. Chem. Chem. Phys. 19, 28470-28475*: "Temperature dependence of the hydrogen bond network in trimethylamine N-oxide and guanidine hydrochloride-water solutions ".

- Ch. J. Sahle, J. Niskanen, C. Schmidt, J. Stefanski, K. Gilmore, **Y. Forov**, S. Jahn, M. Wilke, C. Sternemann (2017) *J. Phys. Chem. B 121, 11383-11389*: "Cation hydration in supercritical NaOH and HCl aqueous solutions ".

- S. Dogan, M. Paulus, **Y. Forov**, C. Weis, M. Kampmann, C. Cewe, I. Kiesel, P. Degen, P. Salmen, H. Rehage und M. Tolan (2018). *J. Phys. Chem. B 122, 3953-3960*: "Human Apolipoprotein A1 at Solid/Liquid and Liquid/Gas Interfaces ".

- C. Weis, G. Spiekermann, C. Sternemann, M. Harder, G. Vankó, V. Cerantola, Ch. J. Sahle, **Y. Forov**, R. Sakrowski, I. Kupenko, S. Petitgirard, H. Yavaş, C. Bressler, W. Gawelda, M. Tolan und M. Wilke (2018). *J. Anal. At. Spectrom.,*

Acknowledgments

Eidesstattliche Versicherung

Ich versichere hiermit an Eides statt, dass ich die vorliegende Dissertation mit dem Titel "X-ray studies on adsorption processes at solid-liquid interfaces and ultrafast dynamics in water" selbständig und ohne unzulässige fremde Hilfe erbracht habe. Ich habe keine anderen als die angegebenen Quellen und Hilfsmittel benutzt sowie wörtliche und sinngemäße Zitate kenntlich gemacht. Die Arbeit hat in gleicher oder ähnlicher Form noch keiner Prüfungsbehörde vorgelegen.

_____   _____
Ort, Datum   Unterschrift

Belehrung

Wer vorsätzlich gegen eine die Täuschung über Prüfungsleistungen betreffende Regelung einer Hochschulprüfungsordnung verstößt handelt ordnungswidrig. Die Ordnungswidrigkeit kann mit einer Geldbuße von bis zu 50.000,00 € geahndet werden. Zuständige Verwaltungsbehörde für die Verfolgung und Ahndung von Ordnungswidrigkeiten ist der Kanzler/die Kanzlerin der Technischen Universität Dortmund. Im Falle eines mehrfachen oder sonstigen schwerwiegenden Täuschungsversuches kann der Prüfling zudem exmatrikuliert werden (§ 63 Abs. 5 Hochschulgesetz - HG -).

Die Abgabe einer falschen Versicherung an Eides statt wird mit Freiheitsstrafe bis zu 3 Jahren oder mit Geldstrafe bestraft.

Die Technische Universität Dortmund wird ggf. elektronische Vergleichswerkzeuge (wie z.B. die Software "turnitin") zur Überprüfung von Ordnungswidrigkeiten in Prüfungsverfahren nutzen.

Die oben stehende Belehrung habe ich zur Kenntnis genommen.

_____   _____
Ort, Datum   Unterschrift